ENHANCING THE PERFORMANCE OF A SILICON PHOTONIC OPTICAL MODULATOR USING DEVICE-LEVEL ENGINEERING

A

Thesis submitted

in Partial Fulfilment of the Requirements

for the Degree of

Doctor of Philosophy

by

Darpan Mishra

Department of Electronics and Electrical Engineering
Indian Institute of Technology Guwahati
Guwahati - 781039, Assam, India
April 2021

In hopes that this work may contribute to future research,

this work is dedicated to all researchers.

Certificate

This is to certify that the thesis entitled “**Enhancing the performance of a silicon photonic optical modulator using device-level engineering**", submitted by **Darpan Mishra** bearing registration number 156102009, a research scholar in the *Department of Electronics and Electrical Engineering, Indian Institute of Technology Guwahati*, for the award of the degree of **Doctor of Philosophy**, is a record of an original research work carried out by him under my supervision and guidance. The thesis has fulfilled all requirements as per the regulations of the institute and in my opinion has reached the standard needed for submission. The results embodied in this thesis have not been submitted to any other University or Institute for the award of any degree or diploma.

Date:
Place: Guwahati

Dr. Ramesh Kumar Sonkar
Dept. of Electronics and Electrical Engg.,
Indian Institute of Technology Guwahati,
Guwahati - 781 039, Assam, India.

Acknowledgements

First and foremost, I would like to express my deepest and most sincere gratitude to my supervisor Dr. Ramesh Kumar Sonkar, for the continuous support of my Ph.D. study and research, for his patience, motivation, enthusiasm, and guidance. His kindness, dedication, hard work, and attention to detail helped me in all the time of research, publishing research papers, and writing of this thesis. I could not have imagined having a better advisor and mentor for my Ph.D. study.

Besides my advisor, I am also thankful to my doctoral committee members Prof. Rakhesh Singh Kshetrimayum, Dr. Tamarapalli Venkatesh, and Dr. Arun Tej Mallajosyula for their encouragement, suggestions, and feedback.

My sincere thanks also go to the Head of the Department and other faculty members for their kind help in carrying out this work, including all the members of the research and technical staff of the department.

I thank my fellow labmates, friends, and seniors, Mr. Bikash Sah, Mr. Chandan Kumar, Mr. Manoranjan Minz, Mr. Sandeep Pandey, Mr. Mohit Mishra, Mr. Atanu Purkayastha, Mr. Dhiman Kakati, Mr. Dibyajyoti Das, Dr. Jitendra Prajapati, and Mr. Mrinmoy Bharadwaj for the stimulating discussions (both research and other topics) and for all the fun we have had in the last five years. I thank all the members of the Hostel Management Committee (Dibang Hostel, 2016-17) and Research Scholar Forum (EEE, 2017-18 and 2018-19), of which I was a part. It is impossible for me to write the name of all the individuals who have helped me (both directly and indirectly) during my Ph.D., and for that, I apologize.

My deepest gratitude goes to my family for supporting me throughout this journey and bearing all the pain that may have ensued due to my prolonged distraction. My father, who himself is an electrical engineer, motivated me to select engineering as my field of study. I am very grateful to my parents for believing in me.

Last, but not least, I would like to thank the *Ministry of Electronics and Information Tech-*

nology, Government of India, for providing scholarship under the *'Visvesvaraya PhD Scheme for Electronics and IT'* to carry out the research presented in this thesis.

(Darpan Mishra)

Abstract

The research presented in this thesis deals with enhancing the performance of an optical modulator in Si photonics platform using device-level engineering techniques. The thesis starts with an introduction to the field of Si photonics, followed by a comprehensive theory of modulation techniques and metrics used to characterize the modulation efficiency. A chapter on optical waveguides is presented elaborating on determining the waveguide characteristics, viz., mode, loss, and dispersion, using a Ge-doped Si strip waveguide for multimodal application over the whole optical telecom band. A PN phase shifter, which is an integral part of an MZM, is modeled, taking into account the 2D nature of carrier distribution and mode field. The proposed model can be used to design and optimize a PN phase shifter with multiple design parameters viz., wavelength, waveguide dimension, core and cladding material, doping concentration, and junction offset. The model is validated with numerical TCAD simulation. The performance of a Si MZM with quasi-TM mode propagation is evaluated and shown to achieve >100 Gbps transmission over a single channel. Material engineering to improve the performance is studied by designing a multi-layer SiGe phase shifter. The equivalent electrical circuit of the proposed multi-layer PN phase shifter is presented. A process simulation study to create the multi-layer structure by a single Ge implantation in Si is done and, both lateral and vertical PN phase shifter performance is evaluated. The high-speed characteristics of Ge-doped Si MZM are compared with a Si MZM and shown to achieve better performance in terms of higher modulation bandwidth, receiver tolerance, and fiber transmission. The designed Ge-doped Si MZM can be used for 400G datacom applications with >100 Gbps per channel.

Contents

List of Figures

List of Tables

List of Acronyms

AO	Acousto-optic
BER	Bit-error-rate
BOX	Buried Oxide
BPM	Beam Propagation Method
°C	Celsius
cm	centimeter
CMOS	Complementary Metal Oxide Semiconductor
CPW	Coplanar Waveguide
CWDM	Coarse Wavelength Division Multiplexing
DAC	Digital-to-analog Converter
dB	Decibel
DC	Direct Current
DOS	Density of States
DWDM	Dense Wavelength Division Multiplexing
EDFA	Erbium-doped Fiber Amplifier
EIM	Effective Index Method
EO	Electro-optic
ER	Extinction ratio
eV	Electron-volt
FCA	Free-carrier Absorption
FCPD	Free-Carrier Plasma Dispersion
FDTD	Finite Difference Time Domain

FEM	Finite-element Method
FKE	Franz-Keldysh Effect
fs	femtosecond
GB	Giga-Byte
Gbps	Gigabit per second
Ge	Germanium
GHz	Gigahertz
G-S-G-S-G	Ground-Signal-Ground-Signal-Ground
GVD	Group Velocity Dispersion
HD-FEC	Hard-decision Forward Error Correction
HH	Heavy-hole
IL	Insertion loss
IQ	In-phase/Quadrature-phase
ITO	Indium-tin-oxide
K	Kelvin
keV	Kilo electron-volt
KHz	Kilohertz
km	kilometer
$LiNbO_3$	Lithium Niobate
LH	Light-hole
MHz	Megahertz
mm	millimeter
MO	Magneto-optic
MRM	Micro-ring Modulator
MRR	Micro-ring Resonator
mW	milli-Watt
MZI	Mach-Zehnder Interferometer
MZM	Mach-Zehnder Modulator

nm	nanometer
NL-EPM	Non-local Empirical Pseudopotential Method
NRZ	Non-return-to-zero
Ω	Ohm
OOK	On-off Keying
P-L	Payne-Lacey
PAM	Pulse Amplitude Modulation
PDL	Polarizarion Dependent Loss
pJ	pico-Joule
PMD	Pre-metal Dielectric
PRBS	Pseudo-random Bit Sequence
ps	picosecond
QAM	Quadrature Amplitude Modulation
QCSE	Quantum Confined Stark Effect
QSFP	Quad Small Form-factor Pluggable
QV-FDM	Quasi-vectorial Finite Difference Method
RAM	Random Access Memory
RF	Radio Frequency
RTA	Rapid Thermal Annealing
Si	Silicon
SiGe	Silicon Germanium
Si_3N_4	Silicon Nitride
SiO_2	Silicon Dioxide
SMF	Single Mode Fiber
SO	Spin-orbit
SOI	Silicon on Insulator
SPM	Self Phase Modulation
Tbps	Terabit per second

TCAD	Technology Computer Aided Design
TE	Transverse Electric
TM	Transverse Magnetic
TO	Thermo-optic
TWE	Traveling-Wave Electrode
μm	micrometer
WDM	Wavelength Division Multiplexing
ZDWL	Zero Dispersion Wavelength

List of Symbols

A_a	Phonon absorption coefficient
A_e	Phonon emission coefficient
$a_{\|\|}$	In-plane lattice constant
$a_{\perp}$	Out-of-plane lattice constant
a_0	Lattice constant
α	Absorption coefficient
α_{FCA}	Free-carrier absorption loss
α_m	Intrinsic material absorption
α_{scat}	Scattering loss
α_{TWE}	TWE attenuation
β	Mode propagation constant
β_2	Group velocity dispersion coefficient
c	Speed of light
c_{11}, c_{12}, c_{44}	Material elastic constant
C_d	Phase shifter depletion capacitance
ΔE_c	Conduction band offset
ΔE_v	Valence band offset
ΔN_e	Change in electron concentration
ΔN_h	Change in hole concentration
$\Delta\alpha$	Change in absorption coefficient
Δn	Change in real part of refractive index
$\Delta\phi$	Phase shift of light

Δ_{so}	Spin-orbit splitting energy
Δx	Cell size
D	Total dispersion
D_{GVD}	Group velocity dispersion
E	Mode electric field
$\vec{E}$	Interface electric field
E_b	Energy per bit
E_g	Band-gap energy
E_{hh}	Heavy-hole band energy
E_i	Input light electric field
E_{lh}	Light-hole band energy
E_o	Output light electric field
E_{so}	Spin-orbit band energy
E^x	Quasi-TM mode electric field
E^y	Quasi-TE mode electric field
ϵ'	Strain tensor
$\epsilon_{\parallel}$	In-plane strain
$\epsilon_{\perp}$	Out-of-plane strain
ϵ	Absolute permittivity
$\bar{\epsilon}$	Strain energy
ϵ_0	Free-space permittivity
ϵ_{Si}	Silicon relative permittivity
ϵ_T	Tetragonal strain
f_{3dB}	3 dB modulation bandwidth
f_{RC}	*RC* limited bandwidth
f_{τ}	Transit time limited bandwidth
h	layer thickness
H_{BOX}	BOX height

H_m	Metal contact height
$h\nu$	Photon energy
H_{rib}	Rib height
H_{PMD}	PMD height
H_{slab}	Slab height
I_i	Input light intensity
I_o	Output light intensity
k	Imaginary part of refractive index
k_0	Free-space wavenumber
k_B	Boltzmann constant
L	Phase shifter length
$L_{1/e}$	Propagation length where mode power drops to $1/e$ of its input power
L_c	Correlation length of sidewall roughness
L_D	Dispersion length
L_{eff}	Effective waveguide length
L_π	Length required for π phase shift
λ	Wavelength of light
M	Mode confinement
m_0	Electron rest mass
m^*_{ce}	Electron conductivity effective mass
m^*_{ch}	Hole conductivity effective mass
m^*_{de}	Electron density of states effective mass
m^*_{dh}	Hole density of states effective mass
m^*_{hh}	Heavy-hole effective mass
m^*_l	Longitudinal effective mass
m^*_{lh}	Light-hole effective mass
m^*_{so}	Spin-orbit effective mass
m^*_t	Transverse effective mass

μ_e	Electron mobility
μ_h	Hole mobility
n	Real part of refractive index
n'	Complex refractive index
n_{clad}	Cladding refractive index
n_{core}	Core refractive index
n_{eff}	Mode effective index
n_i	Intrinsic carrier concentration
n_m	Microwave index
n_{TE}	Effective index of TE mode
n_{TM}	Effective index of TM mode
N_a	Acceptor concentration
N_d	Donor concentration
ω	Angular frequency of light
P	Total power consumption
P_{TWE}	Dynamic power consumption of TWE arm
ϕ	Phase of light
q	Charge of an electron
R	Resistance
R_S	Source resistance
R_T	Termination resistance
σ	standard deviation of sidewall roughness
τ	Carrier transit time
τ_e	Electron transit time
τ_h	Hole transit time
θ_p	phonon equivalent temperature
T	Temperature
t	Time

t_w	Pulse width
V	Applied voltage
V_b	PN diode built-in voltage
V_{DC}	DC voltage
V_π	Voltage required for π phase shift
V_{pp}	peak-to-peak voltage
V_{RF}	RF voltage
V_{TWE}	Voltage across TWE
V_t	Thermal voltage
W_{cont}	Contact width
W_D	PN diode depletion width
W_m	Metal contact width
W_{rib}	Rib width
W_{slab}	Slab width
x	Germanium mole fraction
$\hat{x}$	x-axis
$\hat{y}$	y-axis
$\hat{z}$	z-axis
Z_0	Characteristic impedance of TWE
ζ	Junction position
ζ_0	Junction offset

Physical Constants

c	2.99792458×10^{8} m.s^{-1}
ϵ_0	$8.85418781 \times 10^{-12}$ F.m^{-1}
h	$6.62607015 \times 10^{-34}$ J.s
k_B	1.380649×10^{-23} J.K^{-1}
m_0	$9.1093837 \times 10^{-31}$ kg
π	3.141592653
q	$- 1.602176634 \times 10^{-19}$ C

List of Publications

Journal Publications

1. **Darpan Mishra** and Ramesh Kumar Sonkar, “Analysis of a SiGe Mach-Zehnder modulator for 400G data communication,” *Applied Optics*, vol. 60, no. 7, pp. 2083-2092, March 2021.
2. **Darpan Mishra** and Ramesh Kumar Sonkar, “Performance assessment of a silicon traveling-wave Mach-Zehnder modulator employing quasi-TM mode propagation,” *Optical Engineering*, vol. 59, no. 12, December 2020.
3. **Darpan Mishra** and Ramesh Kumar Sonkar, “2D modeling of silicon optical PN phase shifter,” *Applied Optics*, vol. 59, no. 4, pp. 998-1007, February 2020.
4. **Darpan Mishra** and Ramesh Kumar Sonkar, “Mode, dispersion, and loss analysis of a graded-index germanium-doped silicon buried strip waveguide,” *Optical Engineering*, vol. 59, no. 1, 016118, January 2020.
5. **Darpan Mishra** and Ramesh Kumar Sonkar, “Analysis of germanium-doped silicon vertical PN junction optical phase shifter,” *Journal of the Optical Society of America B*, vol. 36, no. 5, pp. 1348-1354, May 2019.
6. **Darpan Mishra** and Ramesh Kumar Sonkar, “Analysis of a process simulated graded-index strained silicon-germanium optical phase shifter,” *Optical Materials*, vol. 89, pp. 604-608, March 2019.
7. **Darpan Mishra** and Ramesh Kumar Sonkar, “Design and analysis of a graded-index strained $Si_{1-x}Ge_x$ optical PN phase shifter,” *IEEE Photonics Journal*, vol. 10, no. 6, December 2018.

Conference Publications

1. **Darpan Mishra**, Manoranjan Minz, and Ramesh Kumar Sonkar, "Effect of pre-amorphization and annealing on the performance of a silicon optical phase shifter," *2020 OSA Frontiers in Optics + Laser Science APS/DLS*, Washington DC, United States, 14-17 September 2020.

2. Manoranjan Minz, **Darpan Mishra**, and Ramesh Kumar Sonkar, "Compact polarization beam splitter using contra-directional gratings on SOI platform," *14th Pacific Rim Conference on Lasers and Electro-Optics (CLEO PR 2020)*, Sydney, Australia, 2-6 August 2020.

3. **Darpan Mishra**, Manoranjan Minz, and Ramesh Kumar Sonkar, "Performance evaluation of a quasi-TM mode silicon optical modulator," *2020 IEEE Region 10 Symposium (TENSYMP)*, Dhaka, Bangladesh, 5-7 June 2020.

4. **Darpan Mishra**, Manoranjan Minz, and Ramesh Kumar Sonkar, "A 2D optimization model for silicon optical PN phase shifter simulation," *2020 IEEE 8th International Conference on Photonics (ICP)*, Kota Bahru, Kelantan, Malaysia, 16-18 March 2020.

5. Manoranjan Minz, **Darpan Mishra**, and Ramesh Kumar Sonkar, "Design of a hybrid mode and polarization division multiplexer," *Asia Communication and Photonics Conference (ACPC)*, Chengdu, China, 2-5 November 2019.

6. **Darpan Mishra**, Manoranjan Minz, Ramesh Kumar Sonkar, and Mohd. Mansoor Khan, "Bandwidth optimization of germanium-doped silicon optical modulator for high-speed applications," *Proc. SPIE 11193, Nanophotonics and Micro/Nano Optics V, 111930T, SPIE/COS Photonics Asia*, Hangzhou, China, 20-23 October 2019.

7. Manoranjan Minz, **Darpan Mishra**, Ramesh Kumar Sonkar, and Mohd. Mansoor Khan, "Grating-assisted MDM-PDM hybrid (de)multiplexer for optical interconnect applications," *Proc. SPIE 11193, Nanophotonics and Micro/Nano Optics V, 111930C, SPIE/COS Photonics Asia*, Hangzhou, China, 20-23 October 2019.

8. Manoranjan Minz, **Darpan Mishra**, and Ramesh Kumar Sonkar, "Mode-division multiplexer with contra-directional couplers," *24th Optoelectronics and Communications Conference / Photonic in Switching and Computing Conference (OECC/PSC 2019)*, Fukuoka, Japan, 7-11 July 2019.
9. **Darpan Mishra**, Manoranjan Minz, and Ramesh Kumar Sonkar, "Effect of germanium doping on the performance of a silicon optical modulator," *41st Photonics & Electromagnetics Research Symposium 2019*, Rome, Italy, 17-20 June 2019.
10. Manoranjan Minz, **Darpan Mishra**, and Ramesh Kumar Sonkar, "Design of a 3-channel mode-division multiplexer based on grating assisted couplers," *41st Photonics & Electromagnetics Research Symposium 2019*, Rome, Italy, 17-20 June 2019.
11. Sumantra Chaudhuri, Rakhesh Singh Kshetrimayum, Ramesh Kumar Sonkar, and **Darpan Mishra**, "Dual Circularly Polarized Slot Antenna with Novel Isolator," *41st Photonics & Electromagnetics Research Symposium 2019*, Rome, Italy, 17-20 June 2019.
12. Sumantra Chaudhuri, Rakhesh Singh Kshetrimayum, Ramesh Kumar Sonkar, and **Darpan Mishra**, "High gain dual linearly polarized patch antenna array," *41st Photonics & Electromagnetics Research Symposium 2019*, Rome, Italy, 17-20 June 2019.
13. **Darpan Mishra**, Manoranjan Minz, and Ramesh Kumar Sonkar, "Mode and loss analysis of an ultra-small graded-index strip waveguide for multimode datacenter applications," *2018 IEEE 7th International Conference on Photonics (ICP)*, Langkawi, Malaysia, 9-11 April 2018.
14. Manoranjan Minz, **Darpan Mishra**, and Ramesh Kumar Sonkar, "Design of a grating assisted mode-division multiplexer," *2018 IEEE 7th International Conference on Photonics (ICP)*, Langkawi, Malaysia, 9-11 April 2018.
15. **Darpan Mishra** and Ramesh Kumar Sonkar, "Effect of junction profile on the phase and loss characteristics of a silicon optical modulator," *2017 IEEE Workshop on Recent Advances in Photonics (WRAP)*, Hyderabad, India, 18-19 December 2017.

16. **Darpan Mishra** and Ramesh Kumar Sonkar, “Mode and loss analysis of a graded $Si_{1-x}Ge_x$ strip waveguide,” *Asia Communication and Photonics Conference (ACPC)*, Guangzhou, China, 10-13 November 2017.

1

Introduction

Contents

1.1 Silicon Photonics

Silicon photonics is the study of technology that involves the transmission, manipulation, and detection of light by or through a silicon-based media. Silicon-based media incorporates everything from different forms of silicon viz. crystalline silicon [1], amorphous silicon [2], polycrystalline silicon [3], porous silicon [4], silicene [5], to different compounds and alloys with silicon constituents such as silicon dioxide [6], silicon carbide [7], silicon nitride [8], silicon-germanium [9], silicon-germanium-tin [10], etc. Silicon photonics also involves any hybrid technology involving silicon or its alloys, for example, graphene [11], lithium niobate [12], III-V semiconductors [13], barium titanate [14], etc. Silicon photonics was started by Richard Soref in the early 1990s and had since then evolved into a whole new area of study. Applications of silicon photonics range from astronomy [15], medicine [16, 17], communications [18], to high energy physics [19, 20]. The vast study and applications of silicon photonics have been brought about by the numerous advantages it provides, the foremost being abundant availability and mature low-cost manufacturing. The already established electronics industry uses silicon, thereby giving the possibility of monolithic electronic-photonic integration. From an optical viewpoint, silicon has a high index contrast with its oxide, *i.e.* silicon dioxide, thereby having a larger bending radius and allowing sub-wavelength device dimensions. It also has good thermo-optic properties and non-linear properties [1]. Silicon is an excellent material to realize passive photonic devices. However, the main disadvantage of silicon is its indirect band-gap due to which efficient light sources cannot be realized. Instead, III-V semiconductor lasers are flip-chip bonded to silicon for heterogeneous integration on a silicon substrate [21]. Over the years, numerous studies have been done to realize efficient silicon light sources, some notable technologies being zone folding technique [22, 23], porous silicon [22, 24], erbium implantation [25], tensile-strained germanium [26], silicon-germanium-tin [27, 28], Raman lasers [29], etc. However, silicon-based light sources are still at the research stage due to efficiency and stability issues and are far from commercialization. Another disadvantage of silicon is the absence of the Pockels effect, which is the linear electro-optic effect, due to its centrosymmetric structure. Studies have shown that strained silicon exhibit the Pockels effect by breaking the crystal symmetry [30, 31]. Efficient modulation in silicon, however, is achieved using the free carrier plasma dispersion effect [32].

1.2 Market Scenario

Today, silicon photonics is a huge area of study with academic as well as industry-driven research to realize low cost, energy-efficient photonic devices using silicon. The four key areas, viz. low cost, low power, low footprint, and high speed, are realizable using silicon. Key industries focussed on silicon photonic products are Infinera Corporation, Cisco Systems Inc., Intel Corporation, IBM Corporation, FLIR Systems, and Finisar Corporation in the United States; Mellanox Technologies Ltd. in Israel; Hamamatsu Photonics K.K. and AIO Core Co. Ltd. in Japan; S.T. Microelectronics NV in Switzerland; NKT Photonics in Denmark; SICOYA in Germany; and DAS Photonics in Spain. The global market value of silicon photonics is predicted to reach USD 2518.59 Million by 2024 with a 22.93% compound annual growth rate (source: [33]). In 2019, Cisco acquired Luxtera Inc., which was a leader in silicon photonics and optical transceivers. Intel provides silicon photonics 4 fiber lane optical transceiver for 100G networks in the QSFP28 module with each of the 4 lanes capable of handling up to 28G data rate. There have been multiple startups in silicon photonics, some notable being Ayar Labs in California and France based fabless Scintil Photonics. Nokia has recently, in February 2020, acquired the United States based silicon photonics startup Elenion. The major focus today is to provide high-speed connectivity using photons instead of electrons to carry data. The high-frequency lightwaves provide far greater bandwidth than traditional copper cables.

1.3 National Status

Silicon photonics research in India is academic driven with some notable research being carried out by the Photonics Research Group in the Department of Electronics and Electrical Engineering at the Indian Institute of Technology Guwahati, Assam; the Integrated Optoelectronics Research Group in the Department of Electrical Engineering at the Indian Institute of

Technology Madras, Tamil Nadu; the Centre for Nano Science and Engineering at the Indian Institute of Science, Karnataka; the Nanophotonics Research Group at the Indian Institute of Technology Delhi, Delhi; the Optoelectronic Nanodevice Research Laboratory in the Department of Electrical Engineering at the Indian Institute of Technology Indore, Madhya Pradesh; and, the Integrated Photonics Research Lab in the Department of Physics at the Indian Institute of Technology Roorkee, Uttarakhand.

1.4 International Status

The academic research groups outside India are the Silicon Photonics Group at the University of Southampton, England; the Silicon Photonics Group at the Centre for Nanoscience and Nanotechnology, Université Paris-Sud, France; the Photonics Research Group at Ghent University, Belgium; the Emerging Computing Systems and Design Automation Lab in the Department of Electrical and Computer Engineering at the Colorado State University, United States; University of California, Santa Barbara, United States; and the University of California San Diego, United States.

1.5 Thesis Organization

This thesis is organized in the following chapters:

Chapter 2 presents the theory and working of optical modulators for data communication applications. The different types of modulation and how efficient modulation is done in silicon platform are described. The different types of structures, analysis, and characterization of the modulator are given. The last section of this chapter focuses on the techniques to improve the modulator performance.

Chapter 3 gives an introduction to optical waveguides and their analysis. The mode, loss, and dispersion characteristics of a graded-index silicon-germanium strip waveguide for hybrid multiplexing applications over the coarse wavlength division multiplexing band are presented. The usable number of guided modes at different wavelengths is shown to depend on the mode confinement, propagation loss, and dispersion length.

Chapter 4 presents a 2D model of a silicon PN phase shifter, which can be used to design and optimize the phase shifter performance without any commercial tools. The model takes into account the widening of the depletion region at the core-cladding interface, and a detailed description of the model algorithm is given.

Chapter 5 investigates the performance of a silicon Mach-Zehnder modulator (MZM) employing quasi-TM mode propagation with dual-arm push-pull drive using on-off keying. The quasi-TM MZM can achieve >100 Gbps transmission over a single channel. Performance comparison with state-of-the-art is given.

Chapter 6 introduces a multi-layer graded-index silicon-germanium phase shifter, which exhibits enhanced performance compared to a silicon phase shifter. A process simulation study has been done to emulate a fabricated device using both lateral and vertical PN junction profiles. The designed phase shifters are compared with the state-of-the-art.

Chapter 7 investigates the high-speed characteristics of a process simulated germanium-doped silicon MZM for dual-arm quadrature drive. The proposed MZM is compared with recently reported results, and can achieve >100 Gbps data rate over a single channel, and can be used for 400G data communications.

Chapter 8 provides a brief summary of the work carried out during the doctoral tenure.

2

Silicon Optical Modulator: Theory and Working

Contents

2.1 Introduction

The high bandwidth requirement of current data communication due to the increasing number of end-users have paved the way for photonics to replace electronics. A viable solution to the “interconnect bottleneck” problem is to use optical interconnects instead of the metallic interconnects [34–36]. However, such a scheme suffers from high costs and a large device footprint. The cost is mainly determined by the fabrication process, while the device size is limited by the wavelength of light and material being used. Silicon photonics with low-cost CMOS compatible fabrication and sub-micron device size due to high index contrast aims at realizing efficient photonic devices [1]. Integrated optics deal with multiple active and passive optical components on a single substrate. Large bandwidth of an optical communication link is needed for high-speed data transmission, with optical modulators at the core of such a data link, used to encode electrical information in light. The optical modulator is thus an integral component of an optical communication link.

2.2 Overview of an Optical Communication System

The basic block diagram of a communication system is shown in Fig. 2.1. It consists of three blocks — the transmitter, channel, and receiver. For an optical communication system that employs light as a data carrier, the transmitter consists of the light source, modulator, and multiplexer; the channel is either fiber optic cable, free-space, or planar waveguides for on-chip integrated circuits; and the receiver consists of demultiplexer and photodetector. In addition, both the transmitter and receiver side contains electrical signal processing and conditioning circuits to handle the electrical data bits. The electrical data bits are integrated into light using the modulator. Instead of an external modulator, the light source itself can be modulated by an electrical driver circuit. However, the direct modulation of light sources is slower than exter-

Fig. 2.1: Block diagram of a communication system.

nal modulation techniques. At a higher frequency of switching, the laser heats up, leading to an increase in the threshold current and corresponding signal distortion [37]. The multiplexer is used to combine multiple channels carrying different data streams. Data can be carried by different wavelengths, both polarizations of each wavelength, and multiple modes of each polarization. Such a scheme is known as hybrid multiplexing. The demultiplexer at the receiver side does the opposite of the multiplexer and separates different channels into different paths to a photodetector, which converts the optical signal to a corresponding electrical signal. The channel either fiber, planar waveguides, or free-space has different effects on the signal. Optical fiber has low attenuation and dispersion owing to a very small index contrast between the core and cladding. The core has a circular cross-section and is larger than the wavelength of light. Optical fibers are used for long-distance communication. Planar waveguides have a rectangular cross-section, and the index contrast is relatively high. Such waveguides have large loss and dispersion and are used for short-distance communication typically for intra-chip applications. Miniaturization of electronic chips to ensure high operating frequency, according to Moore's law, leads to a decrease in the cross-section of the metallic interconnect layers and the distance between the successive layers. In electronic integrated circuits, the metallic interconnect layers form multiple floors with local interconnects at the bottom (example, connections within a logic gate) and global interconnects at the top (example, the connection between different logic gates within a chip). As the device dimensions decrease, the resistance and capacitance increase, thereby increasing the time constant and hence, the propagation delay. This can be overcome by replacing the metallic interconnect layers by optical interconnects, which are basically planar waveguides. Though the optical interconnect dimensions are larger than the corresponding metallic interconnects, multiple floors are not required since a single optical interconnect can carry different data without any crosstalk. However, the need for electrical-to-optical and optical-to-electrical conversion at each device connection (since the base devices are electronic) increases the complexity. Instead, photonic devices with data being processed by manipulating light instead of electrons are preferred and are the major reason for the drive towards realizing photonic chips. For example, logic operations can then be performed using optical logic gates [38] rather than by electronic logic gates. The processing of light is much faster, and the bandwidth of photonic devices is greater owing to their high frequency. The free-space channel uses spatial multiplexing and vector modes to increase the transmission bandwidth [39,40], and follows line-of-sight transmission.

2.3 Optical Telecom Bands

The optical telecom band represents the range of wavelengths over which fiber optic communication takes place, and are given in Table 2.1. The O-, E-, S-, C-, L-, and U-bands represent the original (O), extended (E), short (S), conventional (C), long (L), and ultra-long (U) wavelength bands, respectively.

Table 2.1: Optical telecommunication bands.

Band	Wavelength range (nm)
O	1260 – 1360
E	1360 – 1460
S	1460 – 1530
C	1530 – 1565
L	1565 – 1625
U	1625 – 1675

Currently, long-haul fiber optic communication uses the C-band centered at 1550 nm wavelength due to the advent of the erbium-doped fiber amplifier (EDFA). Data is carried using multiple wavelengths of an optical telecom band, known as wavelength division multiplexing (WDM). The two types of WDM generally used are the dense wavelength division multiplexing (DWDM) and coarse wavelength division multiplexing (CWDM). DWDM supports up to 80 channels over a single fiber and uses 0.4 nm (0.8 nm) channel spacing for a 50 GHz (100 GHz) grid. Currently, DWDM is used over only C- and L-band. CWDM, on the other hand, utilizes multiple optical bands, from O- to L-band, and allows up to 18 channels with channel spacing of 20 nm. DWDM is expensive compared to CWDM due to the requirement of sophisticated transceivers.

2.4 Types of modulation

An optical modulator modulates light according to a message signal. The message signal is encoded in light by changing its properties, such as amplitude, phase, frequency, or polarization. In a broad sense, modulation can be of two types — direct modulation and external modulation.

In direct modulation, the light source itself is modulated according to a message signal, which is in electrical form. Direct modulation of a laser source is simple and, thus, cost-effective. In direct modulation, the current input to the laser is varied. However, direct modulation suffers from carrier induced frequency drift known as chirping, and heating issue at high-frequency operation [41].

In external modulation, a device is used, which changes the property of light according to the message signal, which can be in any form. External modulators are preferred for high-speed operation and to extend the life of the light source. There are various types of external modulation, such as mechanical, acousto-optic (AO), thermo-optic (TO), magneto-optic (MO), all-optical, and electro-optic (EO). In mechanical modulation, a mechanical shutter or chopper is used, which blocks the path of light [42]. The mechanical modulators are basically discs with slits that are rotated by means of a motor. These are used for sub-kHz modulation and suffers from the diffraction of light beams around the slit edges. AO modulators change the optical properties of a light beam using acoustic waves. Light is passed through an AO crystal subjected to RF signal. There are two different types of AO modulation mechanisms — Raman-Nath regime [43] and Bragg regime [44]. AO modulators can reach speeds up to the MHz range. In TO modulators, the optical property, namely the refractive index, is varied by varying the temperature. Silicon has a TO coefficient of $1.86 \times 10^{-6}\ \mathrm{K}^{-1}$. Silicon TO modulators have been realized and can achieve modulation up to lower GHz range [45]. MO modulators use the magnetic field to vary the property of a light beam. The left and right circular polarizations travel at different speeds when subjected to a quasi-static magnetic field [46]. The polarization of light when passed through a MO material change which is known as the Faraday rotation. All-optical modulators can be used to circumvent electrical-to-optical and optical-to-electrical conversions by using a light beam to modulate another light beam [47]. This type of modulation is faster and less noisy. However, the main drawback is the requirement of a controlling light beam. In EO modulators, light is passed through a material subjected to an electric field. The electric field is varied to change the property of the light beam. Different types of EO modulation are the Pockels effect, Kerr effect, Franz-Keldysh effect (FKE), quantum confined stark effect (QCSE), and the free-carrier plasma dispersion (FCPD) effect.

The Pockels effect is the fastest EO effect, but occurs in non-centrosymmetric materials, *i.e.*, crystals which do not have a center of symmetry. The most widely studied crystal is the man-made $LiNbO_3$ [48]. The Pockels effect is known as the linear EO effect as it is directly proportional to the applied electric field. Silicon, however, does not exhibit the Pockels effect due to its centrosymmetric structure. However, strain applied to silicon breaks the crystal symmetry and has been shown to have the Pockels effect [30, 31]. The Kerr effect occurs in all materials but is weak. The Kerr effect is the second-order EO effect and is proportional to the square of the electric field [49]. In the FKE, an applied electric field is used to shift the optical absorption edge to lower energies [50]. Thus, light is absorbed even if the photon energy is less than the band-gap. QCSE describes light absorption in quantum-well structures, where the absorption differs depending upon the direction of the applied electric field relative to the quantum wells [51]. The FCPD effect uses an applied electric field to modulate light by changing the carrier concentration across a junction device [32]. Since the Pockels effect is absent in silicon, the FCPD effect is preferred for high-speed modulation. This thesis focusses on FCPD based silicon modulators, and thus a separate section is dedicated to describing the FCPD effect in detail.

2.5 The FCPD effect

The FCPD effect is the most effective EO effect used in silicon for modulation. In the FCPD effect, an electric field is applied across a junction device to change the carrier concentration, which in turn changes the refractive index as seen by the light beam. The refractive index is a complex quantity given as

$$n' = n + ik \tag{2.1}$$

where k is related to the absorption coefficient as [52]

$$k = \frac{\alpha\lambda}{4\pi} \tag{2.2}$$

The Drude model gives the relation between the change in n' and the change in carrier concentration which is [52]

$$\Delta n = -\frac{e^2\lambda^2}{8\pi^2 c^2 \epsilon_0 n}\left(\frac{\Delta N_e}{m^*_{ce}} + \frac{\Delta N_h}{m^*_{ch}}\right) \tag{2.3a}$$

$$\Delta\alpha = \frac{e^3\lambda^2}{4\pi^2 c^3 \epsilon_0 n}\left(\frac{\Delta N_e}{m^{*2}_{ce}\mu_e} + \frac{\Delta N_h}{m^{*2}_{ch}\mu_h}\right) \tag{2.3b}$$

However, an empirical fit to (2.3) was given by Soref and Bennett by experimentation for 1550 nm wavelength as [32]

$$\Delta n = -\left[8.8 \times 10^{-22}\Delta N_e + 8.5 \times 10^{-18}(\Delta N_h)^{0.8}\right] \tag{2.4a}$$

$$\Delta\alpha = 8.5 \times 10^{-18}\Delta N_e + 6.0 \times 10^{-18}\Delta N_h \tag{2.4b}$$

where the change in carrier concentrations ΔN_e, ΔN_h are in cm^{-3}. The coefficients in (2.4a) and (2.4b) have units of cm^3 and cm^2 respectively. Applying an electric field changes both n and α, as they are related by the Kramers-Kronig dispersion relation [53]. However, the use of either one primarily for modulation specifies whether the modulator is electrorefraction type or electroabsorption type. In electrorefraction modulators, change in Δn is used to change the phase of light. Thus, the integral part of an eletrorefraction modulator is the phase shifter, and such modulators are referred to as phase modulators. In contrast, electroabsorption modulators use the change in $\Delta\alpha$ to modulate light. While electroabsorption modulator structures employ a single wire waveguide across which an electric field is applied to change the absorption coefficient, in electrorefraction modulators, an interferometer and resonator structures are most commonly used.

2.6 FCPD phase modulator structures

There are mainly two types of structures used viz. the Mach-Zehnder interferometer (MZI) and the micro-ring resonator (MRR) for FCPD based phase modulators. MZI and MRR structures are passive and are made active by integrating phase shifters in the arms of the MZI and the ring cavity of MRR and are called the Mach-Zehnder modulator (MZM) and the micro-ring modulator (MRM), respectively. The bird's-eye view of an MZM and MRM are shown in Fig. 2.2.

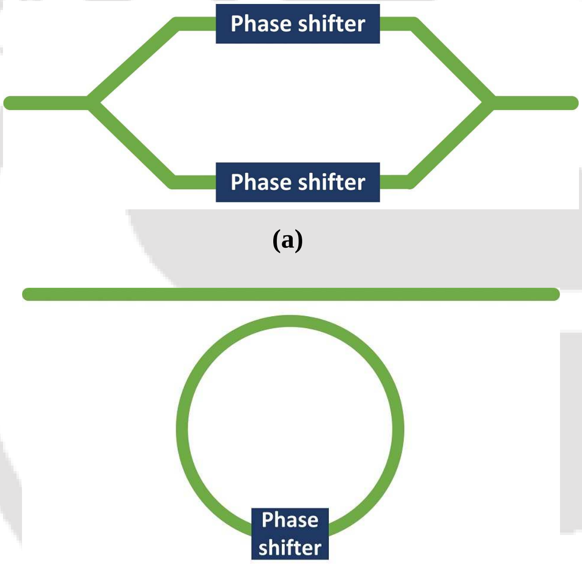

(a)

(b)

Fig. 2.2: Bird's-eye view of (a) MZM and (b) MRM.

The MZM consists of an input 1 × 2 3 dB power splitter, two bus waveguides connected to the output of the power splitter, and a 2 × 1 output combiner whose input are the bus waveguides. The phase shifter is integrated into the bus waveguides. An applied electric field is used to change the phase of light either in one or both arms. The relative phase difference between the two arms at the combiner side determines the output light intensity. The MZM is used as an intensity modulator. If the relative phase difference between the two arms is an even multiple of π, constructive interference takes place, and ideally (considering loss is zero), the output intensity is equal to the input intensity. This represents the bit '1'. If the relative phase difference is an odd multiple of π, destructive interference takes place, and the output light intensity is ideally zero. This represents the bit ‘0’. It should be kept in mind that zero intensity doesn’t mean that the light vanishes. Rather the mode leaks to the cladding.

The MRM operates on the principle of resonance. It consists of a bus waveguide and a ring cavity. The cavity is shown to be circular, but, can be shaped like a racetrack to improve light coupling. The phase shifter is integrated in the ring waveguide. The ring is so designed such that when light couples, the round-trip phase difference is an even multiple of π. In this case, the ring is said to be in resonance, and the output intensity is ideally (considering full light coupling) zero. Applying an electric field to the phase shifter changes resonant condition (round-trip phase difference), and the zero transmission point changes to a different wavelength.

Both the MZM and MRM have been extensively studied [54–59], and the advantages and disadvantages of both are given in Table 2.2.

Table 2.2: Comparison of MZM and MRM.

Metrics	MZM	MRM
Fabrication tolerance	High	Low
Temperature sensitive	Less	More
Power consumption	High	Low
Footprint	Large	Small

Most studies prefer MZMs to MRMs due to its high fabrication and temperature tolerance and use various techniques to optimize the phase shifter to have lower power consumption and small device footprint.

2.7 MZM architecture

The MZM cannot be driven as a lumped element due to the relatively long phase shifter length required to obtain a π phase shift. The phase shifter length can be reduced by using a larger drive voltage but at the cost of higher power consumption. A transmission line model is employed, and a traveling wave electrode (TWE) is used to overcome the bandwidth limitation of the MZM. This occurs due to the inductive impedance of the transmission line electrode, which cancels the phase shifter capacitive load [60]. The MZM configuration with ground–signal–ground–signal–ground (G-S-G-S-G) TWE for the dual-arm drive is shown in Fig. 2.3.

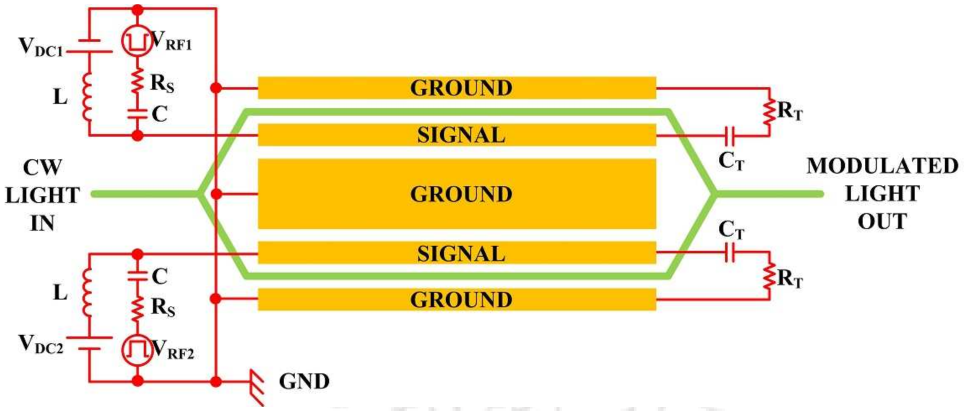

Fig. 2.3: MZM configuration with CPW TWEs in both arms.

Each of the phase shifter arms is treated as a coplanar waveguide (CPW) structure [61]. The PN phase shifters are kept reverse-biased using DC voltage sources V_{DC1} and V_{DC2}, as shown in Fig. 2.3. The inductor L and capacitor C at the source side are used to block the RF and DC voltages, respectively. The termination capacitance C_T is used to block the DC signal, which drops across the PN diode. The capacitances C and C_T offer very low (ideally zero) impedance to the RF source, which travels along the signal electrode in the same direction as the optical wave. The RF source has an associated impedance denoted in Fig. 2.3 as R_S which is typically 50 Ω. The resistance R_T is used at the termination side and is also taken to be 50 Ω. The MZM is driven by applying the high-frequency voltages V_{RF1} and V_{RF2} across the two PN phase shifters. The partial capacitance and conformal mapping techniques [62, 63] are used to obtain the electrical equivalent circuit of the phase shifter. The modulation bandwidth depends on three major factors, viz. the impedance mismatch between the source, TWE, and termination resistance; velocity mismatch between the optical mode and the traveling RF signal; and the RF loss. The TWE should be designed such that the optical mode group index is equal to the RF microwave refractive index to reduce the adverse effect of velocity mismatch. A TO phase shifter is used in one or both arms of the MZM (not shown in Fig. 2.3) to set the operating point.

2.8 MZM transfer characteristics

The MZM bias and driving voltage are determined from the modulator transfer characteristics, which gives the relation between the output light intensity and the input light intensity. In terms of the electric field, the input light intensity can be written as

$$I_i = |E_i e^{-j\omega t}|^2 \tag{10}$$

The 3-dB splitter at the input side splits the input light into equal halves, each with intensity $I_i/2$. Table 2.3 shows the notations used in terms of the electric field for the corresponding intensity.

Table 2.3: Intensity and corresponding electric field notation.

Intensity	I_i	$I_i/2$	α
Electric field	E_i	$E_i/\sqrt{2}$	$\alpha/2$

The output electric field of the two arms are given by

$$E_{o1} = \frac{E_i}{\sqrt{2}} e^{-\frac{\alpha_1 L_1}{2}} e^{-j(\omega t + \beta_1 L_1 + \phi_1(V) L_1)} \tag{11a}$$

$$E_{o2} = \frac{E_i}{\sqrt{2}} e^{-\frac{\alpha_2 L_2}{2}} e^{-j(\omega t + \beta_2 L_2 + \phi_2(V) L_2)} \tag{11b}$$

For a symmetric MZM, $\beta_1 = \beta_2$ and $L_1 = L_2$. The output electric field and corresponding output light intensity is

$$E_o = \frac{1}{\sqrt{2}} (E_{o1} + E_{o2}) \tag{12a}$$

$$I_o = |E_o|^2 \tag{12b}$$

For a single-arm drive with the other arm grounded, the output intensity is

$$I_o = \frac{I_i}{4} \Big[e^{-j\left(\phi_1(V_1) - j\frac{\alpha_1(V_1)}{2}\right)L} + e^{-j\left(\phi_1(0) - j\frac{\alpha_1(0)}{2}\right)L} \Big]^2 \tag{2.7}$$

For the dual-arm drive in quadrature, the output intensity is

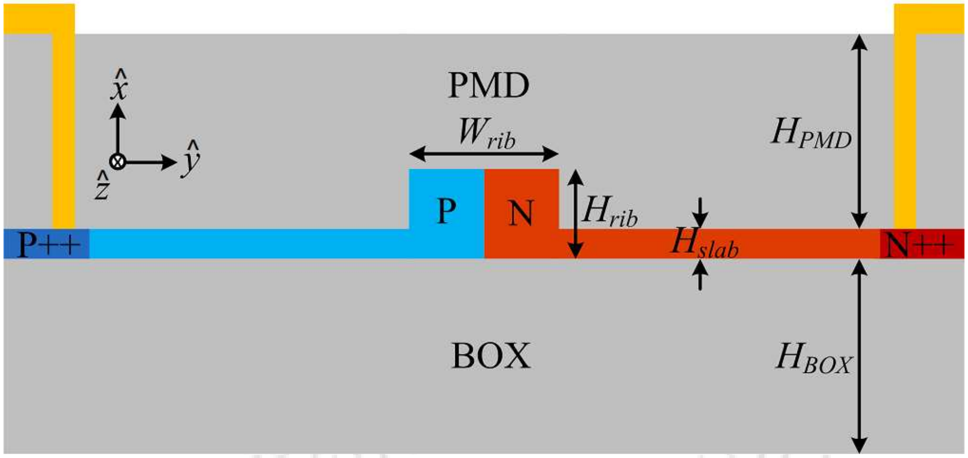

Fig. 2.4: PN phase shifter cross-section.

$$I_o = \frac{I_i}{4}\left[e^{-j\left(\phi_1(V_1) - j\frac{\alpha_1(V_1)}{2}\right)L} e^{-j\frac{\pi}{2}} + e^{-j\left(\phi_1(V_2) - j\frac{\alpha_1(V_2)}{2}\right)L}\right]^2 \tag{2.8}$$

The factor $e^{-j\frac{\pi}{2}}$ in the first term on the right-hand side of (2.8) is used to set the MZM in quadrature operation using a TO phase shifter.

2.9 Characterizing the MZM

The phase shifter performance affects the high-speed modulator characteristics. Both the phase shifter and modulator performance metrics are listed below.

2.9.1 Phase shifter performance metrics

The phase shifter is basically a junction device, with the most common being the PN junction [64], the PIN junction [65], and the MOS capacitor [66]. The PN junction is the fastest as it works in reverse bias by depletion of majority charge carriers. However, the length of the PN phase shifter is longer. In contrast, the PIN is used in forward bias by injection of minority carriers. The advantage is that the length of the PIN phase shifters is less. The MOS-capacitor based phase shifters work in accumulation mode.

The cross-section of a PN phase shifter is shown in Fig. 2.4. The PN phase shifter is created on a silicon-on-insulator (SOI) wafer. The underlying silicon substrate (not shown in the figure) is comparatively thick and provides mechanical strength. The rib is created by etching the top silicon layer and is suitable for realizing active devices since the contact electrodes can be formed far away from the modal region. The buried oxide (BOX) layer is sufficiently thick to prevent mode leakage to the underlying silicon substrate. The top cladding is the pre-metal dielectric (PMD) layer. Silicon dioxide (SiO_2) has been used as both the BOX and PMD material. The contact electrodes are formed by creating vias in the PMD layer and depositing metal. The electrodes are formed over heavily doped P++ and N++ regions to ensure they are ohmic in nature. The waveguide height (width) is along $\hat{x}$ ($\hat{y}$) direction. The mode propagates along $\hat{z}$ direction.

The phase shifter is characterized by the

(i) Phase shift:

The phase shift is calculated as [67]

$$\Delta\phi = \frac{2\pi L}{\lambda}\int_{\hat{x}}\int_{\hat{y}} \Delta n(\hat{x},\hat{y})\,|E^y(\hat{x},\hat{y})|^2\, d\hat{x}\, d\hat{y} \tag{2.9}$$

(ii) Absorption loss:

The absorption loss is determined as [67]

$$\alpha = \alpha_{scat} + \int_{\hat{x}}\int_{\hat{y}}\left[\Big(\alpha_{FCA}(\hat{x},\hat{y}) - \Delta\alpha(\hat{x},\hat{y})\Big)\times|E^y(\hat{x},\hat{y})|^2\right] d\hat{x}\, d\hat{y} \tag{2.10}$$

The calculation of α_{scat} and α_{FCA} can be found in Appendix A along with different types of loss components.

(iii) Modulation efficiency:

The modulation efficiency is the product of voltage (V_π) and length (L_π) required to achieve π phase shift and is calculated as

$$V_\pi L_\pi = |V| \times \frac{\pi}{\Delta\phi(V)} \tag{2.11}$$

(iv) $\alpha V_\pi L_\pi$:

This is a FOM defined as the total absorption at any voltage for π phase shift.

(v) Insertion loss:

The insertion loss of a device is defined as the loss in signal power when the device is inserted into a communication link and can be calculated as [67]

$$IL = 4.34 \times \alpha(0V)\, L_\pi \tag{2.12}$$

A higher $\Delta\phi$, lower α, lower value of $V_\pi L_\pi$, lower IL, and lower $\alpha V_\pi L_\pi$ corresponds to a better phase shifter.

2.9.2 MZM performance metrics

The MZMs are characterized by

(i) 3 dB modulation bandwidth:

The 3 dB modulation bandwidth is described as the frequency range in which the modulation sensitivity is within 3 dB of the peak value. The RC-limited bandwidth of the phase shifter is given as

$$f_{RC} = \frac{1}{2\pi RC_d} \tag{2.13}$$

where R is the series resistance of the PN phase shifter and C_d is PN junction depletion capacitance.

(ii) Extinction ratio (ER):

The ER is the ratio of the output intensity for *‘on’* and *‘off’* state of the modulator, or in other words, the ratio of light intensity to represent bit ‘1’ and bit ‘0’. ER is determined from the modulator transfer characteristics.

(iii) Bit-error-rate (BER):

The BER represents the ratio of error bits to the total bits received. BER ranges from 0 to 1.

(iv) Speed:

The speed of the modulator represents how fast the modulator can modulate light with the electrical data bits.

(v) Energy per bit (E_b):

The E_b represents the energy efficiency of the modulator and is given as

$$E_b = \frac{P}{Bit\,Rate} \tag{2.14}$$

The total power consumption (P) is determined by summing the power consumption of all the TWE arms that are driven. The dynamic power consumption of each TWE arm is given as [68]

$$P_{TWE} = \frac{(V_{TWE}/2)^2}{Z_0} \tag{2.15}$$

A high modulation efficiency, ER, speed, and lower BER and E_b corresponds to a better modulator.

2.10 Improving MZM performance

The increasing demand for high bandwidth devices to decrease latency has given rise to numerous techniques to realize high-speed devices. The performance can be improved by broadly two techniques – system-level engineering and device-level engineering.

2.10.1 System-level engineering

Low-bandwidth modulators can be used to achieve high-speed operation using system-level engineering, which focusses on modulator driving configurations and modulation formats. The bandwidth can be enhanced by using a series push-pull operation, which lowers the diode capacitance [69]. Higher modulation speed can be achieved by using advanced modulation formats such as pulse amplitude modulation (PAM) and quadrature amplitude modulation (QAM). Four silicon MZMs with an average modulation bandwidth of 30 GHz at -3 V have been shown to achieve 106 Gbps per lane using PAM-4 [70]. Two MZMs with 3 dB bandwidth of 36 GHz at -4 V have been used in in-phase quadrature (IQ) modulator configuration with series push-pull operation and shown to achieve up to 232 Gbps operation using 16-QAM [71]. While the simple on-off keying (OOK) was the choice of modulation for 100G networks, the IEEE 802.3bs specifies PAM-4 modulation for 400G networks [72]. The 100G network uses 4-lane 25G modulators, while 400G network uses either 4-lane 100G modulators or 8-lane 50G modulators. Though advanced modulation formats can lead to higher data speeds, the overall chip power increases due to the increased complexity in realizing the electrical driver circuitry. A DAC-less PAM-4 modulator is reported in [73], which lowers the power consumption by using two OOK electrical drivers to generate PAM-4 signal in the optical domain.

2.10.2 Device-level engineering

Device-level engineering focusses on increasing the modulation bandwidth using material engineering and junction optimizations instead of using advanced modulation formats. The modulation bandwidth can be increased by designing the phase shifter either to have lower capacitance per unit length or to have a higher phase shift per unit length resulting in lower length. The modulation efficiency is an important metric to measure the modulator efficiency. Small V_π will result in lower drive voltage required for light extinction and result in low E_b. The phase shifter design and optimization is the main focus of device-level engineering. The phase shifter metrics depend on the modal overlap with the depletion region. The waveguide, material, and junction parameters play an important role in the design of a phase shifter to improve the overall device performance. The waveguide parameters include the waveguide dimensions, which determines the mode confinement and scattering loss. The material parameters include the carrier effective mass, mobility, lifetime, and material absorption. The junction parameters include the type of junction, junction profile, dopant species, doping concentration, and the junction offset. It is crucial to select appropriate parameter values for optimum performance as there are numerous trade-offs involved that affects the device performance and can be found in [74–78].

Numerous optimizations based on waveguide dimensions [67,79,80], materials like strained silicon-germanium [81, 82], hydrogenated amorphous silicon [83, 84], silicon slot waveguide with ITO [85], junction parameters like use of PN [64, 75, 86, 87], PIN [65], PIPIN [88], interleaved/interdigitated PN [77, 89], and doping optimizations like restricted depth doping [90], U-shaped junction [91], S-shaped junction [92], L-shaped junction [93], including optimization of ion-implantation conditions [94], etc., have been reported over the years to enhance the phase shifter performance.

2.11 Summary

A basic overview of an optical communication system is provided with the optical telecom bands used for communication. The different types of modulation techniques are defined with special attention to the FCPD effect, which is used for efficient modulation in silicon. The phase modulator structures are shown with emphasis on the MZM, which is used throughout this thesis. The phase shifter is defined as an integral part of a phase modulator, and the performance metrics of the phase shifter and MZM are defined. Lastly, techniques to improve the modulator performance are briefly discussed.

3

Optical Waveguides: Basic Building Block of Photonic Devices

Contents

3.1 Introduction

An optical waveguide is a structure that guides light along a particular direction, which is known as the propagation direction. A waveguide consists of a core that has a high index of refraction surrounded by a cladding with a low index of refraction. The most common type of optical waveguide is the optical fiber, which has a cylindrical cross-section. The optical fiber transmits light by the mechanism of total internal reflection. Optical fibers can be either single-mode or multimode. Multimode optical fibers use a graded-index structure to reduce modal dispersion. Integrated photonic chips have rectangular waveguide structures due to the feasibility of planar fabrication. Planar photonic chips employ nanowire waveguides to realize active and passive photonic devices. Optical waveguides are used as a channel for data transmission. To increase the information rate, different wavelengths, both polarization of each wavelength, and multiple modes of each polarization are used as channels. Based on specific applications, waveguide design is crucial, and their analysis is necessary for optimum device performance. For a given material system and waveguide dimension, the channel length depends on the dispersion-loss characteristics of each light mode and is related to its effective index. The mode, loss, and dispersion characteristics depend on waveguide core-cladding material and waveguide dimensions. Planar rectangular cross-sectional waveguide uses high index contrast core-cladding materials as opposed to optical fibers in order to reach sub-wavelength dimensions. However, such planar waveguides suffer from high modal dispersion due to their high index contrast and are suitable for short-distance communication typically in the range of few micrometers to few millimeters. Silicon-on-insulator (SOI) wafers are commonly used for planar photonic devices due to their low-cost CMOS processing with an index contrast of ~2 over the whole coarse wavelength division multiplexing (CWDM) band. Optical waveguides can be formed by etching the top silicon layer to create rib (partially etched) or strip (fully etched) waveguides, putting two waveguide cores close to each other to create slot waveguides, or by drilling holes in the top silicon layer to create a photonic crystal waveguide. The most commonly used optical waveguide for passive applications is the channel/strip waveguide.

Waveguide analysis involves the parametric study of the effect of core-cladding materials and waveguide dimensions on the number of supported modes, mode group velocity, birefringence effects, modal dispersion, mode confinement, propagation losses, etc. Multiple literature studies exist that focus on the analysis of different types of waveguides. Single-mode condition in SOI rib waveguides was given by Soref *et. al.* [95] and later corrected by Pogossian *et. al.* [96]. The same was analyzed by Huang *et. al.* [97] for SOI rib waveguides at 1550 nm using FEM simulations. Hocker and Burns analyzed mode dispersion of isotropically diffused channel waveguides using EIM [98]. Dulkeith *et. al.* [99] studied the group index and GVD of single-mode SOI strip waveguides. Tan *et. al.* [100] studied the group velocity dispersion (GVD) and self-phase modulation (SPM) in Si_3N_4 waveguides. Lee *et. al.* [101] investigated the effect of waveguide size and surface roughness on the transmission losses of a silicon strip waveguide and used the Payne-Lacey (P-L) model [102] for the scattering loss. Vlasov and McNab [103] measured the propagation and bending losses of submicron single-mode silicon strip waveguides. Daniel and Agrawal [104] studied the effect of waveguide dimensions on the dispersion and birefringence properties. Mas *et. al.* [105] investigated the chromatic dispersion of silicon slot waveguides and showed that the dispersion properties could be tailored by the waveguide geometrical parameters. Hammani *et. al.* [106] performed experimental studies on the linear and non-linear optical properties of silicon-germanium waveguides with varying cross-sectional areas. Apart from these, multiple studies on waveguide dispersion can also be found in literature [107–112].

3.2 Waveguide structure

The graded-index SiGe strip waveguide is process simulated using Synopsys® SPROCESS 2D [113]. The starting material is an SOI wafer with 250 nm top silicon thickness and 2 μm BOX. The graded-index structure is formed by germanium (Ge) doping with a dose of 1.35×10^{17} cm^{-2} at 165 keV energy followed by rapid thermal annealing (RTA) at 1100°C for 5 seconds. Then, a 250 nm anisotropic etch is done to form a strip waveguide of a cross-sectional area 500 nm × 250 nm. The final step is 2 μm top oxide deposition to form a buried strip waveg-

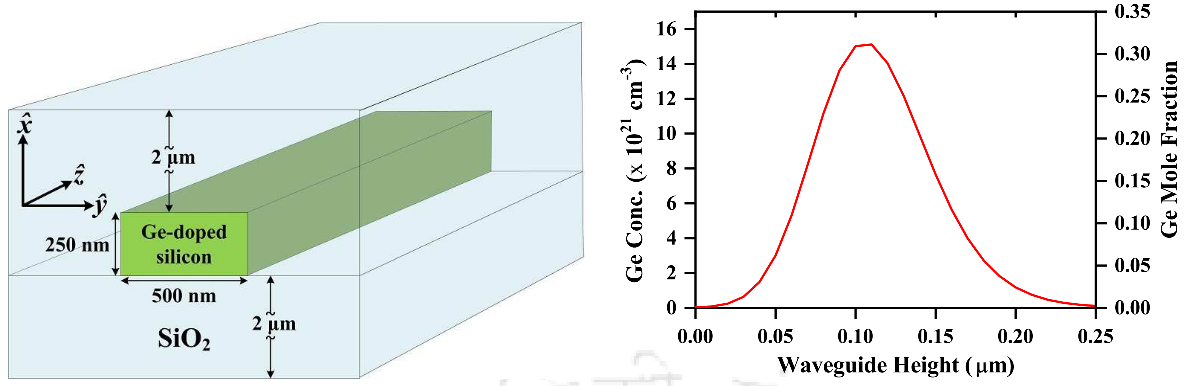

(a) (b)

Fig. 3.1: (a) 3D view of the buried strip waveguide (the silicon substrate is not shown) and (b) Germanium concentration and mole fraction across waveguide height.

uide. The waveguide structure is shown in Fig. 3.1 along with the germanium concentration and mole fraction distribution across the waveguide height.

3.3 Waveguide Analysis

The quasi-vectorial finite difference method (QV-FDM) [114] has been used for mode analysis of the proposed waveguide at different wavelengths. A mesh size of 120 × 100 cells with a uniform cell size of 12.5 nm in each direction has been used with the Neumann boundary condition. The refractive index of silicon and oxide at different wavelengths are calculated from [115] and [116] respectively. The refractive index of $Si_{1-x}Ge_x$ is calculated as [117]

$$n_{SiGe}(x, \lambda) = n_{Si}(\lambda) + (1.16 - 0.26\lambda)\, x^2 \tag{3.1}$$

The maximum Ge mole fraction (x) obtained from the given germanium dose is ~0.31. Ge doping results in material absorption loss if the band-gap energy of the graded $Si_{1-x}Ge_x$ is lower than the corresponding photon energy. The band-gap energy of the proposed structure along waveguide height is calculated as [118]

$$E_g(x) = 1.0905 - 0.962x + 0.4306x^2 - 0.1672x^3 \tag{3.2}$$

The band-gap energy across waveguide height along with the photon energy at different wavelengths is shown in Fig. 3.2. The minimum band-gap energy is ~0.83 eV denoted by the

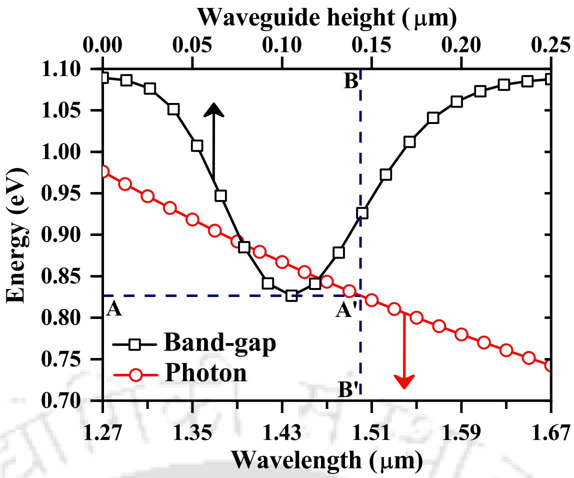

Fig. 3.2: Band-gap and photon energy across waveguide height and photon wavelength respectively.

A-A' line of Fig. 3.2. This corresponds to a photon wavelength of ~1500 nm denoted by the line **B-B'**. Beyond 1500 nm, the waveguide becomes transparent, and thus material absorption does not occur. The material absorption depends on both photon wavelength as well as the Ge mole fraction and is calculated as [118]

$$\alpha_m = \begin{cases} 0 & \text{if } h\nu \le E_g - k_B\theta_p \\ A_a \frac{(h\nu - E_g + k_B\theta_p)^2}{e^{\theta_p/T}-1} & \text{if } E_g - k_B\theta_p \le h\nu \le E_g + k_B\theta_p \\ A_a \frac{(h\nu - E_g + k_B\theta_p)^2}{e^{\theta_p/T}-1} + A_e \frac{(h\nu - E_g + k_B\theta_p)^2}{1-e^{-\theta_p/T}} & \text{if } h\nu \ge E_g + k_B\theta_p \end{cases} \tag{3.3}$$

The real and imaginary part of the refractive index across the waveguide height at different wavelengths are given in Fig. 3.3(a) and 3.3(b) respectively. The refractive index and the

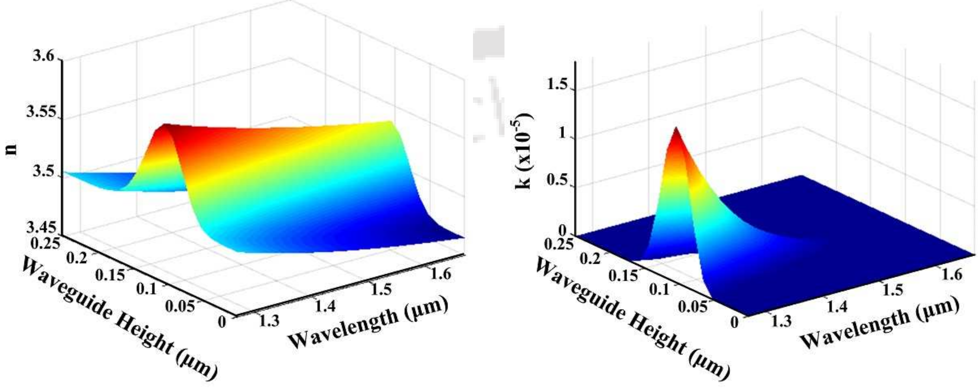

(a) **(b)**

Fig. 3.3: (a) Refractive index and (b) extinction coefficient across the waveguide height at different wavelengths.

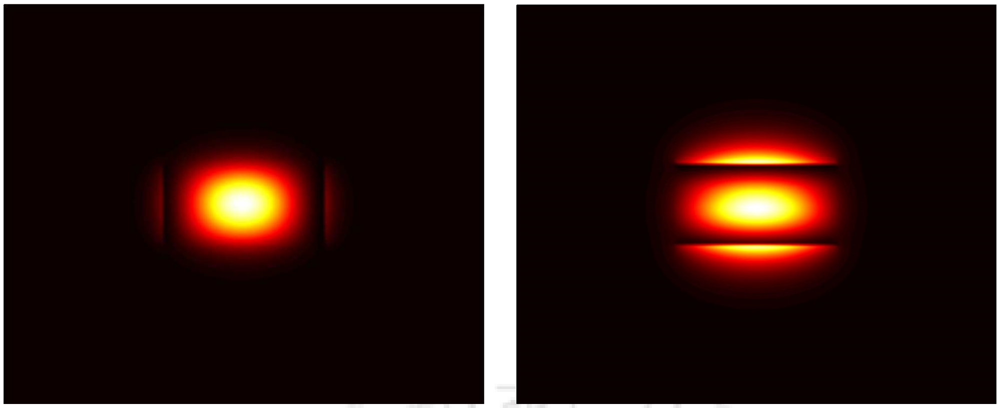

(a) E^y_{00} mode **(b)** E^x_{00} mode

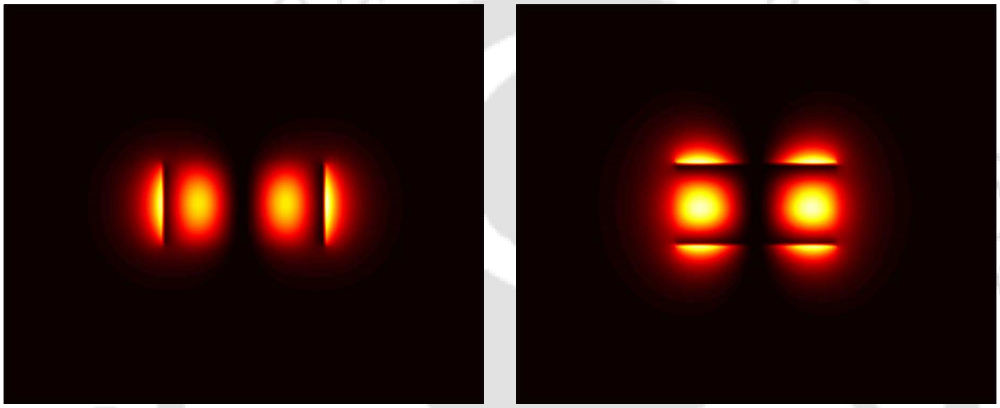

(c) E^y_{10} mode **(d)** E^x_{10} mode

Fig. 3.4: Supported mode profiles of the proposed graded-index strip waveguide at 1310 nm.

extinction coefficient profile across the waveguide height have the same Gaussian-like shape similar to the Ge implantation profile with the refractive index having a square dependency on the mole fraction, as evident from (3.1). The extinction coefficient is negligible after 1500 nm.

The number of modes supported by the waveguide, mode profile, mode effective index, and 2D mode confinement is determined by QV-FDM using the refractive index and extinction coefficient profile across the waveguide height at different wavelengths. For short-range optical communication, the O-band is preferred, which is centered at 1310 nm [119]. The mode profile of the supported modes at 1310 nm is shown in Fig. 3.4. The quasi-TE (quasi-TM) mode is characterized by discontinuity along the waveguide width (height) and is denoted by E^y_{mn} (E^x_{mn}) or HE_{mn} (EH_{mn}), where m and n represents the mode zero-crossing along waveguide width and height respectively.

Different modes of each polarization of each wavelength travel along the waveguide with different velocities. The mode velocity increases with the mode order while the mode confinement deceases. Due to this, different modes will take different time to reach a particular distance, which leads to dispersion. The material is itself dispersive as the refractive index is a function of the wavelength. The proposed graded-index waveguide can be approximated as a multi-layer waveguide with each layer having different dielectric properties. Since the mesh size used in QV-FDM is 12.5 nm, the graded-index waveguide is approximated as a 20-layered waveguide with each layer thickness equal to 12.5 nm. Also, it should be noted that the quasi-TE (quasi-TM) modes are directed parallel (perpendicular) to the layer interfaces along the $\hat{y}$ ($\hat{x}$) axis respectively. The effective material refractive index for the quasi-TE and quasi-TM modes are given as [120]

$$n_{mat}^2 = \begin{cases} \dfrac{\sum\limits_{j=1}^{j=N} \epsilon_j h_j}{\sum\limits_{j=1}^{j=N} h_j} & : E_{mn}^y \text{ mode} \\ \\ \dfrac{\sum\limits_{j=1}^{j=N} h_j}{\sum\limits_{j=1}^{j=N} \dfrac{h_j}{\epsilon_j}} & : E_{mn}^x \text{ mode} \end{cases} \tag{3.4}$$

The group velocity dispersion also known as waveguide dispersion is the second-order dispersion and its coefficient given as [110]

$$\beta_2 = \frac{\partial^2 \beta}{\partial \omega^2} \tag{3.5}$$

The GVD is then calculated from

$$D_{GVD} = -\frac{2\pi c}{\lambda^2}\beta_2 \tag{3.6}$$

The mode GVD compensates the material dispersion, and the total dispersion is calculated by adding both. The material dispersion is calculated using (3.5) and (3.6) by replacing the effective refractive indices of the mode by the effective material refractive index determined from (3.4) [110]. Since the waveguide acts as a data channel, it is important to carefully assign a particular channel to a particular mode. This is because the propagating pulse broadens due to dispersion. The dispersion length is a measure of the distance the pulse travels before it broadens by a factor of $\sqrt{2}$ and is calculated as [99]

$$L_D = \frac{2\pi c}{\lambda^2}\frac{t_w^2}{D} \tag{3.7}$$

For high data rate signals, the pulse width (t_w) is small, and such signals should be assigned to a mode with low dispersion to reduce the pulse broadening.

3.4 Results and Discussions

The effective index and 2D mode confinement of the proposed waveguide as a function of wavelength are shown in Fig. 3.5(a) and (b) respectively. The effective index and mode confinement of all the supported modes decrease with wavelength. The mode confinement of the E^y mode is greater than the E^x mode, which is due to the fact that the waveguide width is greater than the waveguide height.

The total material absorption loss of each propagating mode as a function of wavelength was determined from the imaginary part of the effective index and is shown in Fig. 3.6. The material absorption decreases exponentially with wavelength and is negligible after 1500 nm. A larger

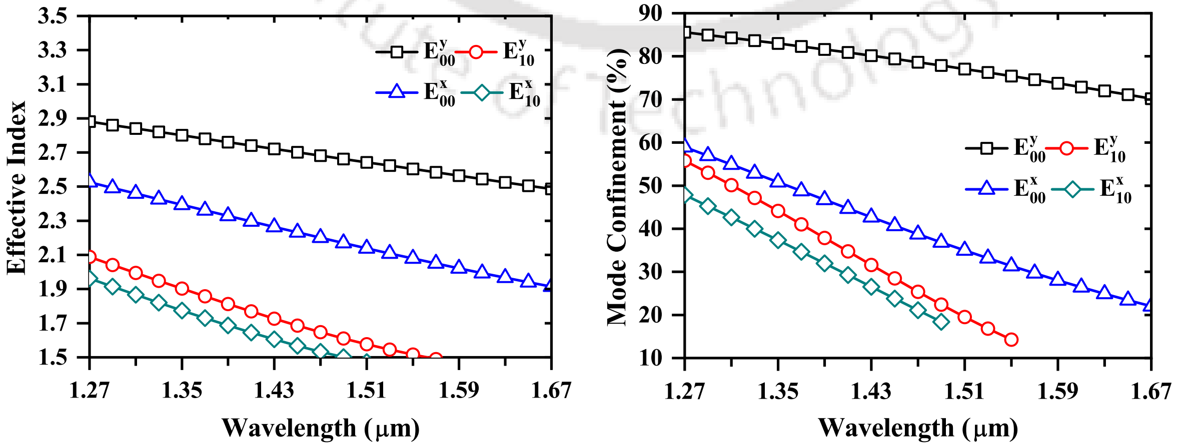

(a) (b)

Fig. 3.5: (a) Mode effective indices and (b) Mode confinement.

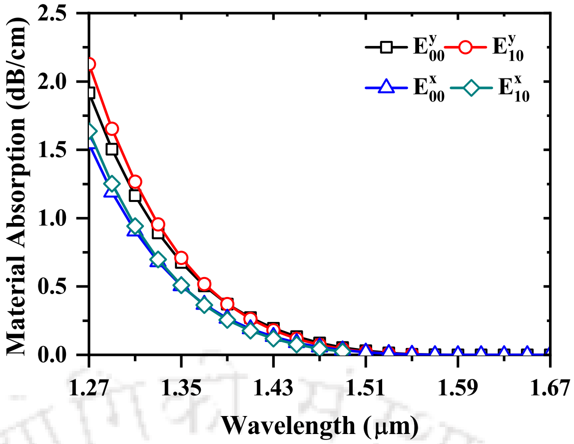

Fig. 3.6: Intrinsic material absorption.

Ge implantation dose would result in the right shift of the material absorption curve. From Fig. 3.6, it can be seen that E^y mode has a higher loss than E^x mode. Also, the first order modes of each polarization have a higher loss compared to the fundamental mode. The reason for the first is that both the fundamental and first-order E^y mode has larger confinement compared to the corresponding E^x modes, respectively. Since the first-order mode has two lobes compared to one lobe of the fundamental mode, larger material absorption occurs for first-order modes.

The scattering loss of the fundamental and first-order modes of both polarization as a function of wavelength is shown in Fig. 3.7(a) and 3.7(b) respectively. The scattering loss is calculated using standard deviation (σ) = 2 nm and correlation length (L_c) = 50 nm [121]. The scattering loss of E^y_{00} mode is more or less constant with wavelength, whereas those of other

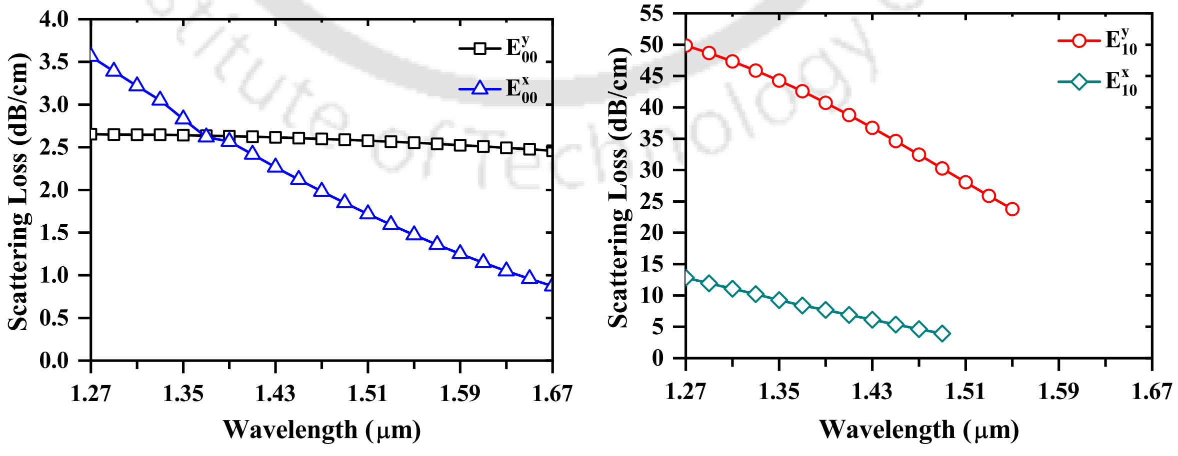

(a) **(b)**

Fig. 3.7: Scattering loss of (a) fundamental modes and (b) first order modes.

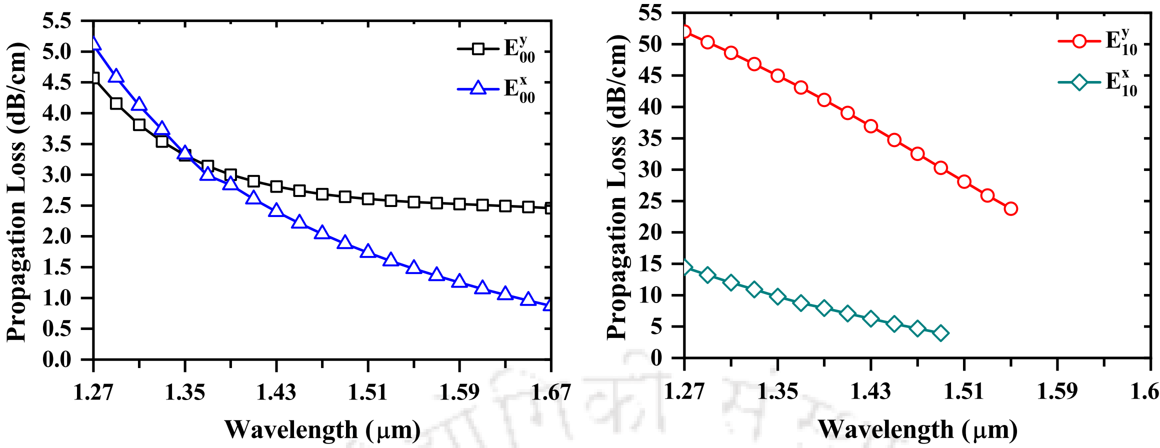

(a) (b)

Fig. 3.8: Propagation loss of (a) fundamental modes and (b) first order modes.

modes decrease. This is due to the fact that the E^{y}_{00} mode has very good confinement, and the mode intensity at the rough sidewalls does not vary much with wavelength. The confinement of other modes decreases with a greater slope, as evident from Fig. 3.5(b).

The mode propagation losses are determined from the scattering and absorption losses of each mode as a function of wavelength. For the fundamental modes of both polarization, the quasi-TM propagation loss is higher than the quasi-TE propagation loss below 1350 nm, as shown in Fig. 3.8(a). For the first-order modes, as seen in Fig. 3.8(b), the contribution of material absorption to the total loss is negligible compared to the scattering loss. The high propagation loss of the higher-order modes results in a lower waveguide length for multimodal applications.

The dispersion coefficient of the modes and material is shown in Fig. 3.9(a). The GVD of the different supported modes takes into account the material dispersion. The GVD coefficient of the modes for O-band is shown in Fig. 3.9(b) and shows the zero-dispersion wavelength (ZDWL) of the different modes. For the designed graded-index strip waveguide, ZDWL occurs in the O-band, which is suitable for multimodal operation. The E^{y}_{00} mode does not have any ZDWL, and the calculated dispersion in the O-band is in the range of -2450 ps/nm.km to -850 ps/nm.km. The ZDWL for the E^{x}_{00}, E^{y}_{10}, and E^{x}_{10} modes are 1353.3 nm, 1313.2 nm, and 1270.0 nm respectively. The O-band has three mode-dispersion crossovers, which are labeled in Fig. 3.9(b). The comparable GVD coefficients of different modes will result in a lower intermodal

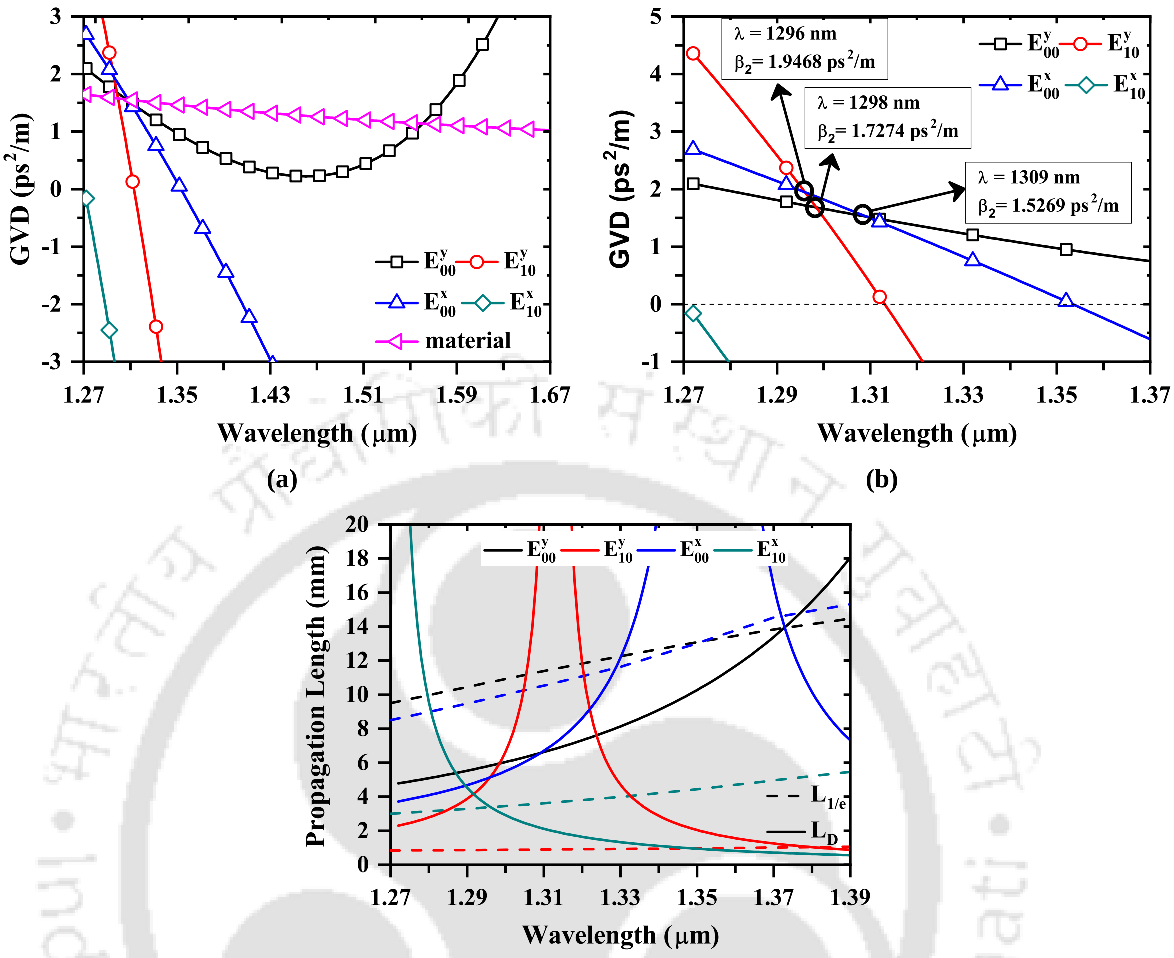

(a)

(b)

(c)

Fig. 3.9: (a) Mode and material GVD coefficient over CWDM band, (b) mode GVD showing ZDWL and mode-dispersion crossovers, and (c) L_D and $L_{1/e}$ for different supported modes.

delay for mode-division multiplexing applications. Fig. 3.9(c) shows the propagation length of different modes as a function of wavelength in 1270 nm to 1390 nm range. Two propagation lengths are shown in the figure. L_D (*solid line*) is the dispersion length and $L_{1/e}$ (*dashed line*) is the mode propagation length at which the mode power drops to $1/e$ of its input power. L_D is a measure of the dispersion, whereas $L_{1/e}$ is a measure of the propagation loss. The effective waveguide length is limited by both the mode propagation loss and the mode dispersion and is determined as $L_{eff} = min(L_D, L_{1/e})$. The pulse width used to calculate L_D in Fig. 3.9(c) is 100 fs. For data rates of a few hundred gigabits per second (Gbps), L_D is in metres, and the length is limited by the propagation loss. Since planar waveguides are used for intra-chip communication, the length ranges from few micrometres to few millimetres. This allows for sub-picosecond pulse usage resulting in terabit per second (Tbps) communication.

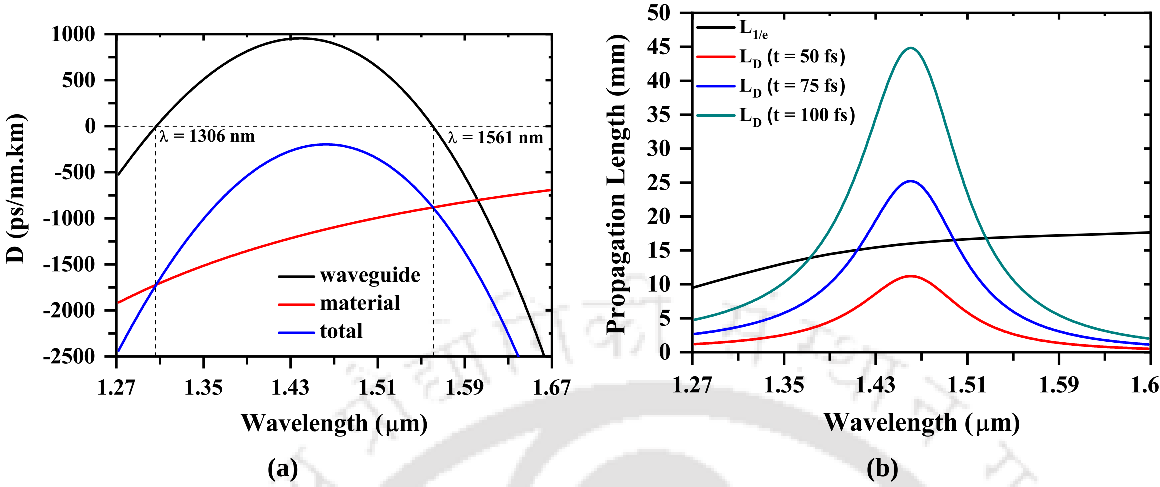

Fig. 3.10: (a) Waveguide, material, and total dispersion of E^y_{00} mode over the CWDM band and (b) The corresponding propagation length of E^y_{00} showing $L_{1/e}$ and L_D for input pulses with differnt pulse width.

The dispersion characteristic of the fundamental quasi-TE mode is shown in Fig. 3.10(a), which shows the waveguide, material, and the total dispersion as a function of wavelength. At 1306 nm and 1561 nm, the waveguide dispersion is zero. Between these two wavelengths, the waveguide dispersion compensates the material dispersion. However, for the designed graded-index waveguide parameters, the E^y_{00} mode does not have a ZDWL over the entire CWDM wavelength range. The E^y_{00} dispersion is normal and remains in the negative dispersion region. The lowest dispersion of -197 ps/nm.km occurs at a wavelength of 1460 nm. The propagation length of the same is shown in Fig. 3.10(b) for three different pulse widths, t_w = 50 fs, 75 fs, and 100 fs. For t_w = 50 fs, the waveguide length for E^y_{00} excitation across the CWDM band is limited by dispersion. For t_w = 75 fs and 100 fs, the waveguide length is limited by the propagation loss in the wavelength range of 1400-1500 nm and 1370-1530 nm, respectively. The E^y_{00} mode dispersion is negative for the chosen waveguide parameters and results in pulse compression [122].

The total number of modes that can be used depends on the specific application. Not only do propagation loss and dispersion limit the usable number of modes, but the mode confinement should also be taken into account. For example, at 1270 nm, if all four modes are used as channels, L_{eff} is ~ 0.83 mm with lowest mode confinement of ~ 47.8%. At 1490 nm, L_{eff} is ~

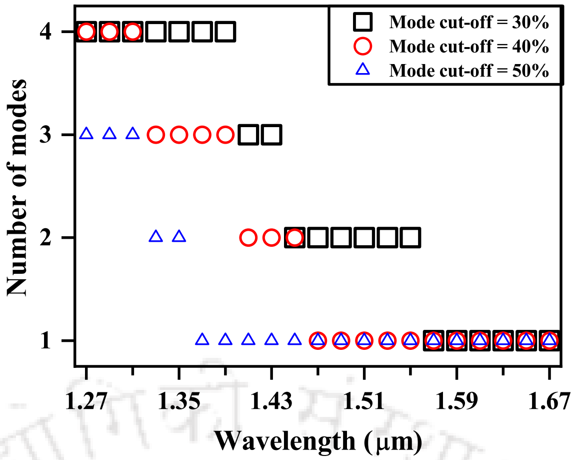

Fig. 3.11: Number of usable modes of the designed graded-index strip waveguide for different mode cut-off values.

1.43 mm but the lowest mode confinement is only ~ 18.4%. To determine the usable number of modes, a mode cut-off can be set depending on the application and then, the waveguide length can be determined from the mode with the highest propagation loss or dispersion. Fig. 3.11 shows the usable number of modes when the mode-cutoff is set at 30%, 40%, and 50%.

Long-range optical communication takes place in the C-band centered at 1550 nm while the O-band centered at 1310 nm is preferred for short-haul datacenter applications. At 1550 nm, the higher-order modes are cut-off. The mode confinement of the quasi-TE mode is ~ 75% compared to the quasi-TM mode confinement of ~ 31%. The waveguide is essentially single-mode at 1550 nm. The material absorption is absent and the E_{00}^{y} mode dispersion is ~ -737 ps/nm.km. At 1310 nm, the waveguide supports four modes with $|D| <$ 5200 ps/nm.km and mode confinement $>$ 42%. However, the lowest dispersion and highest mode confinement occurs at 1290 nm with $|D| <$ 3000 ps/nm.km and mode confinement $>$ 45%.

For the graded-index structure shown here or for any multi-layer waveguides in general, the effective material refractive index depends on the individual refractive indices and on the layer thicknesses. Also, since the grading is along one direction only, the effective index seen by the quasi-TE and quasi-TM modes are different, and the material becomes birefringent. The quasi-TE refractive index is higher compared to the quasi-TM mode refractive index as calculated from (3.4). The birefringence ($n_{TE} - n_{TM}$) varies linearly from $\sim 4.20 \times 10^{-4}$ at 1270 nm to $\sim 3.25 \times 10^{-4}$ at 1670 nm. However, the similar slope of the quasi-TE and quasi-

TM mode refractive index results in equal quasi-TE and quasi-TM material dispersion. The modal group velocity dispersion can be tailored to obtain any desired ZDWL by varying the waveguide dimensions [110] or by using multi-layer cladding [123]. The mode, dispersion, and loss characteristics can also be tailored by varying the germanium dose and energy, keeping the waveguide dimensions the same.

3.5 Summary

A graded-index buried strip waveguide on the SOI platform has been designed, and the mode, dispersion, and loss characteristics have been determined for CWDM wavelengths. Mode parameters such as the number of propagating modes and mode confinement of each mode at different wavelengths for the proposed waveguide have been calculated. The material and scattering loss components of different modes over the CWDM band have been determined. The material and mode dispersion characteristics for short-wavelength multimode transmission and CWDM single-mode transmission have been discussed. The designed waveguide has higher-order zero-dispersion wavelengths in the O-band, and the fundamental quasi-TE mode has the lowest dispersion of -197 ps/nm.km at 1460 nm. For any waveguide dimension, the number of modes that can be used is limited by the mode confinement. The waveguide is suitable for sub-picosecond pulse propagation, and the waveguide length is shown to be limited by both the propagation loss and the mode dispersion.

4

Silicon Optical Modulator: A 2D Model

Contents

4.1 Introduction

The design of the phase shifter is crucial for optimum modulator performance. The phase shifter performance depends on multiple parameters like waveguide dimensions, core and cladding refractive index, the wavelength of light, and doping concentration. It is important to do a parametric study and optimize the performance before fabrication, as multiple trade-offs are involved. The phase shifter is usually designed using commercial tools [124–127] which use numerical methods that are iterative in nature, e.g., finite-difference time-domain (FDTD) [128–130], beam propagation method (BPM) [131–133], finite element method (FEM) [134–136], Newton (fully-coupled) [137–139] and/or Gummel (de-coupled) [140–142] iterations etc., for solving the mode parameters and/or device transport equations. Multiple optimizations are involved in minimizing the simulation runtime by reducing the number of iterations, which depend on the structure complexity and mesh size. However, such commercial tools are expensive, and the alternative is to code the numerical algorithms, which require an in-depth knowledge of the iterative methods. An easy way is to use analytical formulas that give fast and reliable results under a certain set of conditions as these are derived, taking into account multiple approximations.

A rigorous model till now is not present to the best of the authors' knowledge, which takes into account the 2D carrier distribution and 2D electric field effects. Rasigade *et. al.* [79] used a 1D diode model, and the index change is analytically calculated by approximating the optical intensity as a gaussian law. In [67], Rasigade *et. al.*, approximated the optical intensity by a Pearson VII distribution to achieve a better fit of the evanescent waves for strong light confinement. Pérez-Galacho *et. al.* [76] presented a simplified model using 1D electrical simulation and calculated the overlap with the optical mode, which was calculated using finite-element or finite-difference methods with smaller mesh size, requiring large simulation runtime. However, such 1D models assume that the depletion width along the waveguide height is uniform, which is not the case in practice. The dielectric change at the core-cladding interface leads to a fringing electric field, which causes the depletion width to widen at the interface [143]. This effect

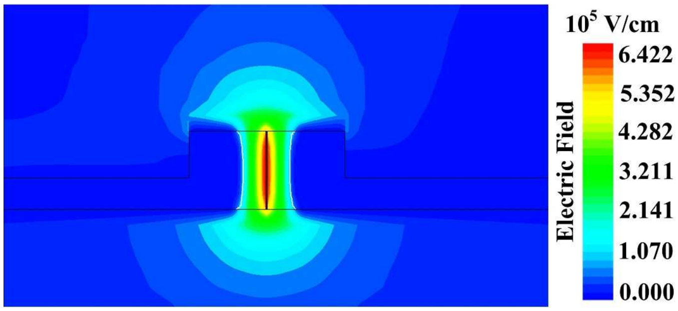

Fig. 4.1: 2D electric field distribution across the rib waveguide showing widening of the depletion region at the top and bottom interfaces (TCAD simulation). The waveguide dimensions are, W_{rib} = 500 nm, H_{rib} = 250 nm, H_{slab} = 100 nm, with PN doping of 5×10^{17} cm^{-3} each, and at a reverse bias of 5 V.

is more pronounced at higher reverse bias voltages and smaller waveguide cross-section. To show the importance of 2D modeling of a rib phase shifter, the TCAD simulation of a PN phase shifter is shown in Fig. 4.1, which shows the widening of the depletion width at the interface and the fringing electric field. The simulation parameters of TCAD simulation are given in the figure caption. The fringing electric field gives rise to fringe capacitances, and the total PN depletion capacitance increases [143].

4.2 Model flowchart

The block diagram of the 2D modeling approach used is shown in Fig. 4.2. The 2D mode field is constructed using the effective index method (EIM). EIM is also used to calculate the

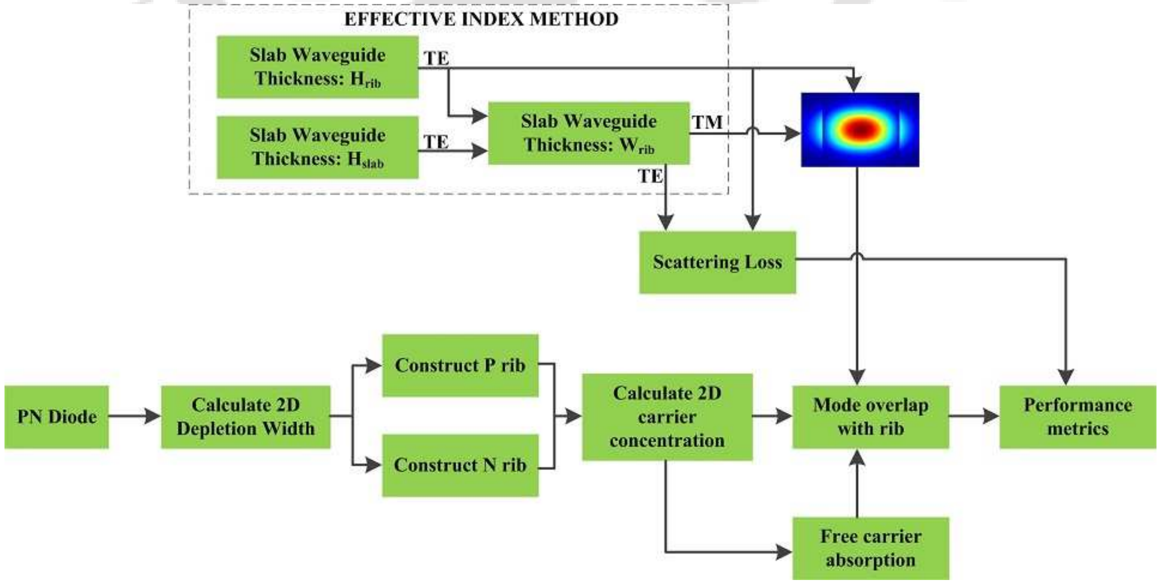

Fig. 4.2: Block diagram of the 2D PN phase shifter model.

scattering loss by the Payne-Lacey (P-L) model given in Appendix A. The 2D PN depletion width is determined from analytical equation using an algorithm to discretize the same. A 2D mesh is created to emulate the waveguide structure. The phase shifter performance metrics are then determined from the modal overlap with the waveguide rib.

4.3 Calculating the mode field

The first requirement is to design a single-mode rib waveguide. EIM is used to calculate the number of modes, mode effective indices, and to construct the 2D mode electric field across the waveguide. To make the waveguide single-mode, smaller H_{rib} is used such that quasi-TM mode is cut-off. To ensure that the waveguide supports only fundamental quasi-TE mode (E^y_{00}) propagation, W_{rib} and H_{slab} is adjusted accordingly. A larger W_{rib} requires larger H_{slab} so that higher-order modes leak to the slab. Single-mode propagation is possible with large cross-section waveguide by adjusting the waveguide dimensions [95]. EIM divides the 2D cross-sectional rib waveguide into three slab waveguides with thickness H_{rib}, H_{slab}, and W_{rib}. To solve the E^y (E^x) modes of the rib waveguide, TE (TM) analysis is performed for the slab waveguides with thickness H_{rib} and H_{slab} followed by the TM (TE) analysis of the slab waveguide with thickness W_{rib} using the effective index of the first two TE (TM) slab waveguides as the core and cladding refractive index. The detailed analysis of slab waveguide and EIM is given in [144]. The refractive index of silicon and oxide is a function of wavelength and is calculated from [115] and [116] respectively, which can be used for the optical telecom band. The 2D quasi-TE (quasi-TM) mode of the rib waveguide is calculated from the TE (TM) and TM (TE) fields of the slab waveguide with thickness H_{rib} and W_{rib} as [115]

$$E^y_{2D} = E^y_{1D}.E^x_{1D} \tag{4.1a}$$

$$E^x_{2D} = E^x_{1D}.E^y_{1D} \tag{4.1b}$$

The 2D mode confinement (M) is calculated as

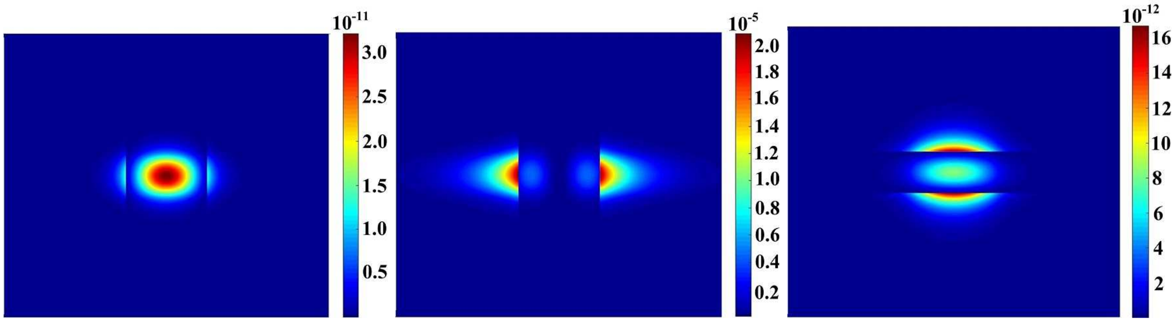

(a) E^y_{00} mode **(b)** E^y_{10} mode **(c)** E^x_{00} mode

Fig. 4.3: Mode profile showing the normalized mode power (color bar). The simulation area is 2.00 μm (width) × 1.75 μm (height).

$$M(\%) = \frac{\int_0^{H_{rib}} \int_0^{W_{rib}} E^2\,dx\,dy}{\int_{-\infty}^{\infty} \int_{-\infty}^{\infty} E^2\,dx\,dy} \times 100 \qquad (4.2)$$

The supported modes of a 500 nm × 250 nm rib waveguide with 50 nm slab at 1550 nm wavelength calculated using EIM is shown in Fig. 4.3 which shows the normalized mode power across the waveguide. The waveguide supports two quasi-TE modes and one quasi-TM mode. The E^y_{00} propagates along the waveguide with mode confinement of 71.66%. The E^y_{10} and E^x_{00} modes are cut-off with a mode confinement of 13.42% and 30.71% respectively. Thus, the waveguide is essentially single-mode. Though the EIM assumes the fields to be separable, the error with respect to numerical techniques is very less [115]. To show the effectiveness of EIM to accurately describe the mode field of a waveguide, EIM is compared with numerical quasi-vectorial finite difference method (QV-FDM) [114], and is shown in Section 4.6.

4.4 Modeling the phase shifter

In modeling the 2D depletion region, the rib is divided into four sections, as shown in Fig. 4.4. The vertical line ($A - A'$) represents the PN junction and divides the waveguide into P-rib and N-rib. The horizontal line ($B - B'$) divides the P-rib and N-rib into top and bottom equal halves. The P-rib top, N-rib top interface, is the PMD-silicon interface, and the P-rib bottom, N-rib bottom is the silicon-BOX interface. The intersection of the $A - A'$ and $B - B'$ line is taken as the axis origin, as shown in Fig. 4.4. The PN diode phase shifter is modeled using 1D

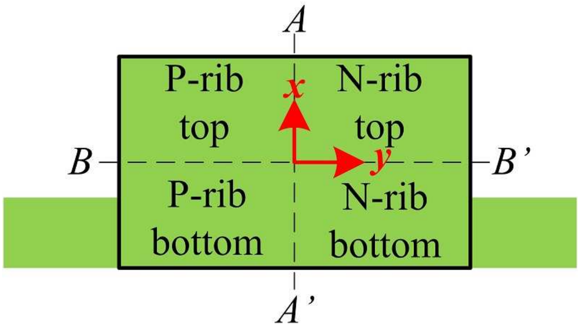

Fig. 4.4: Rib waveguide partition.

diode equations and then extended to 2D by incorporating the 2D depletion width. The built-in voltage is

$$V_b = V_t \ln\left(\frac{N_a N_d}{n_i^2}\right) \tag{4.3}$$

The 1D depletion width is given as [143]

$$W_D^{1D} = \sqrt{\frac{2\epsilon_0 \epsilon_{Si}(N_a + N_d)}{q N_a N_d}(V_b - V - 2V_t)} \tag{4.4}$$

The 1D depletion width of the P-rib and N-rib is

$$W_{Dp}^{1D} = \frac{N_d}{N_a + N_d} W_D^{1D} \tag{4.5a}$$

$$W_{Dn}^{1D} = \frac{N_a}{N_a + N_d} W_D^{1D} \tag{4.5b}$$

The 2D depletion width as given in [143] is calculated for the four rib sections as follows

P-rib top:

$$W_{Dpt}^{2D} = \frac{4W_{Dp_t}^{1D}}{\pi} \sin^2\left(\frac{\theta}{2}\right) - \frac{2W_{Dp_t}^{1D}}{\pi} - W_{Dp}^{1D} \tag{4.6a}$$

$$x_{pt} = \frac{H_{rib}}{2} + \frac{2W_{Dp_t}^{1D}}{\pi}\left\{\ln\left[\tan\left(\frac{\pi}{4} + \frac{\theta}{2}\right)\right] - \sin\theta\right\} \tag{4.6b}$$

P-rib bottom:

$$W_{Dpb}^{2D} = \frac{4W_{Dp_b}^{1D}}{\pi} \sin^2\left(\frac{\theta}{2}\right) - \frac{2W_{Dp_b}^{1D}}{\pi} - W_{Dp}^{1D} \tag{4.7a}$$

$$x_{pb} = \frac{2W^{1D}_{Dp_b}}{\pi}\left\{\sin\theta - \ln\left[\tan\left(\frac{\pi}{4}+\frac{\theta}{2}\right)\right]\right\} - \frac{H_{rib}}{2} \tag{4.7b}$$

N-rib top:

$$W^{2D}_{Dnt} = \frac{2W^{1D}_{Dn_t}}{\pi} + W^{1D}_{Dn} - \frac{4W^{1D}_{Dn_t}}{\pi}\sin^2\left(\frac{\theta}{2}\right) \tag{4.8a}$$

$$x_{nt} = \frac{H_{rib}}{2} + \frac{2W^{1D}_{Dn_t}}{\pi}\left\{\ln\left[\tan\left(\frac{\pi}{4}+\frac{\theta}{2}\right)\right] - \sin\theta\right\} \tag{4.8b}$$

N-rib bottom:

$$W^{2D}_{Dnb} = \frac{2W^{1D}_{Dn_b}}{\pi} + W^{1D}_{Dn} - \frac{4W^{1D}_{Dn_b}}{\pi}\sin^2\left(\frac{\theta}{2}\right) \tag{4.9a}$$

$$x_{nb} = \frac{2W^{1D}_{Dn_b}}{\pi}\left\{\sin\theta - \ln\left[\tan\left(\frac{\pi}{4}+\frac{\theta}{2}\right)\right]\right\} - \frac{H_{rib}}{2} \tag{4.9b}$$

where the subscripts t, b, p, n refers to top PMD-silicon interface, bottom silicon-BOX interface, P-rib, N-rib respectively. W^{2D}_{D} is the 2D depletion width and x is the distance along the rib height. $W^{1D}_{Dp(n)_t}$ and $W^{1D}_{Dp(n)_b}$ are the P (N) depletion widths calculated using (4.4)-(4.5) by replacing the silicon permittivity with PMD and BOX permittivity respectively. (4.6)-(4.9) traces the 2D depletion width along the rib height and depends on θ which varies from $-\pi/2$ to 0. W^{2D}_{D} and x lie along the y and x axis of Fig. 4.4. The parameter θ correlates the 2D depletion width (W^{2D}_{D}) to the 1D depletion width (W^{1D}_{D}) and defines the widening of the depletion width near the top and bottom interfaces. $\theta = 0$ corresponds to the value of W^{2D}_{D} and x at the core-cladding interface while $\theta = -\pi/2$ corresponds to the value towards the middle of the rib away from the interface. The factor $H_{rib}/2$ in (4.6b)-(4.9b) ensures that the axis origin lies in the middle of the rib as shown in Fig. 4.4. The 2D depletion width along the rib height of the four sections are shown in Fig. 4.5 for $N_a = N_d = 5 \times 10^{17}$ cm^{-3} and $H_{rib} = 250$ nm at 0 V. The PN junction is at the middle of the rib width at 0 nm. The rib height and width are shown along the $\hat{x}$-axis and $\hat{y}$-axis directions of the plots. Negative $\hat{y}$-axis indicates P region and positive $\hat{y}$-axis indicates N region. The widening of the depletion width near the interfaces can be seen from Figs. 4.5(a)-(d).

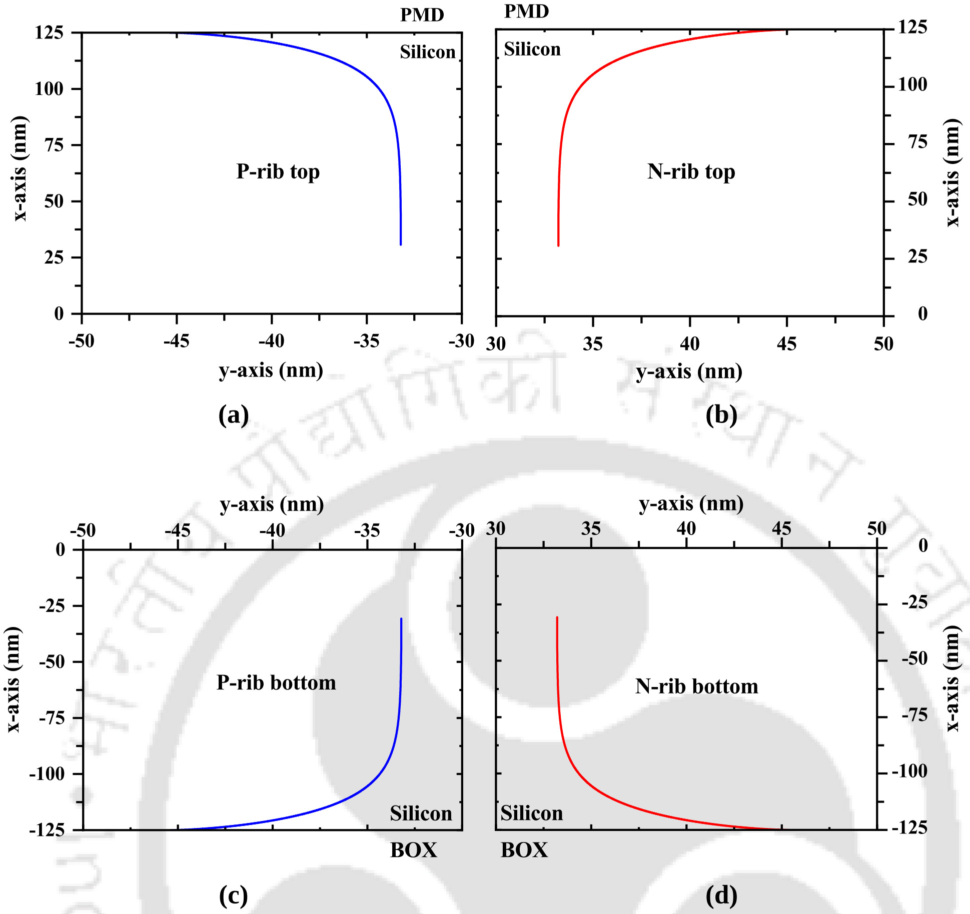

Fig. 4.5: 2D depletion width of (a) P-rib top, (b) N-rib top, (c) P-rib bottom, and (d) N-rib bottom. The '*blue*' and '*red*' lines trace the P and N depletion edges respectively.

Both the depletion width and the distance along rib height have non-linear relation with θ and the distance traced by (4.6)-(4.9) depends on the number of θ points (N_θ) taken. The 2D depletion region for the P-rib top is shown in Fig. 4.6 for different values of N_θ. It can be seen that larger values of N_θ results in larger rib height traced. For the same N_θ, greater rib height distance is traced for higher reverse bias voltages, as shown in Fig. 4.7(a) for P-rib top at N_θ = 5000. Fig. 4.7(b) shows the P-rib top 2D depletion width with oxide and air as the PMD material. The fringing field effect is more prominent for oxide PMD and leads to greater carrier depletion at the interface compared to air.

The rib is modeled by creating 2D cells with uniform cell size Δx. The $W_{rib} \times H_{rib}$ will be represented by $\frac{W_{rib}}{\Delta x} \times \frac{H_{rib}}{\Delta x}$ cells. It should be noted that Δx should also be the increment used in EIM so that modal overlap with the rib can be calculated. To form the 2D depletion region,

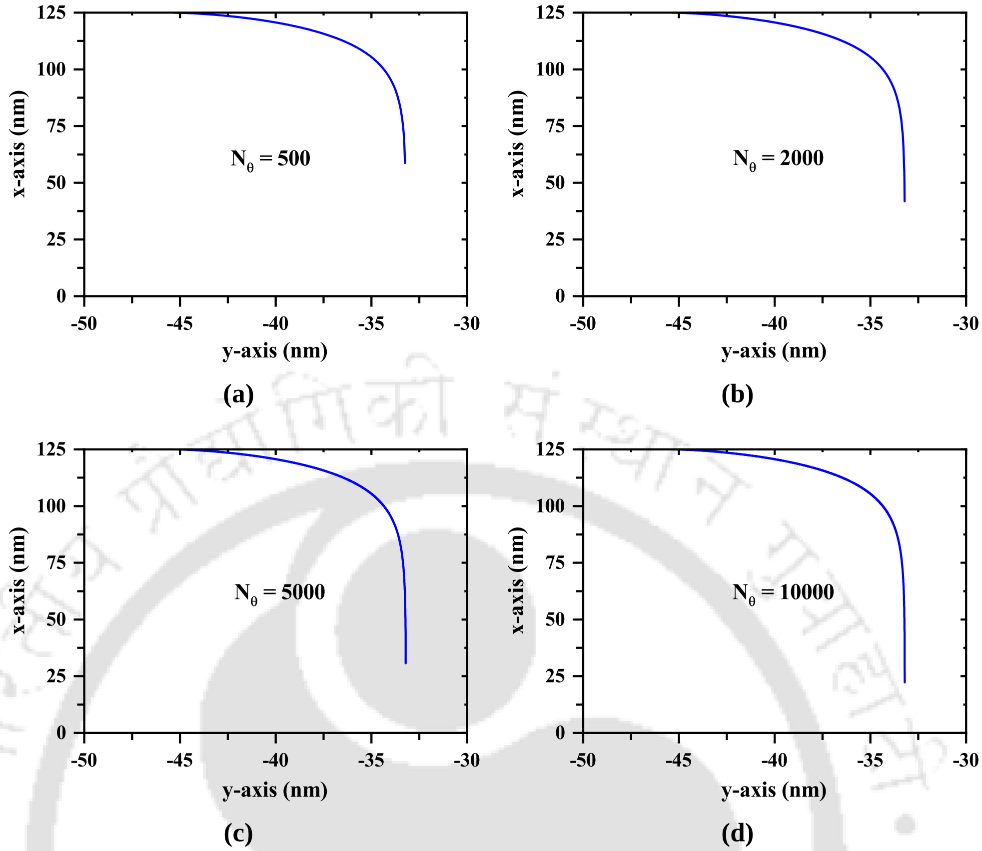

Fig. 4.6: 2D depletion width (‘*blue*’ line) of P-rib top for different values of N_θ.

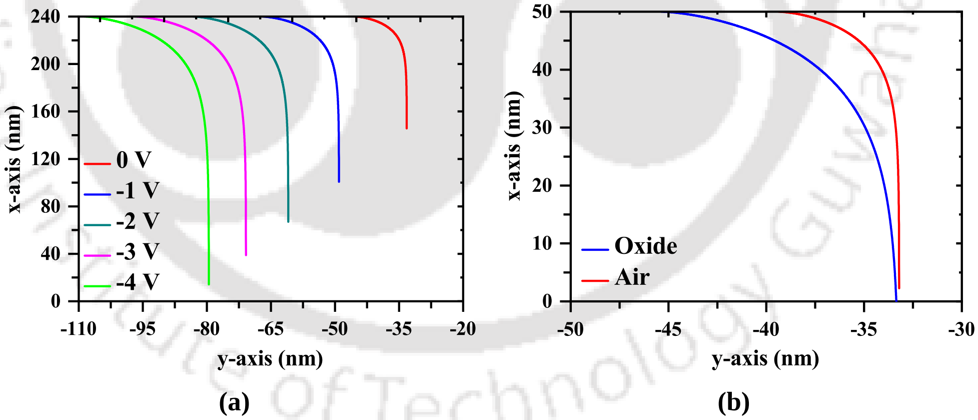

Fig. 4.7: 2D depletion width (*colored lines*) of P-rib top (a) for different reverse bias voltages (H_{rib} = 480 nm) and (b) for different PMD material (H_{rib} = 100 nm).

cells along the rib width across the junction for the P-rib and N-rib should be initialized to zero. The number of depletion cells will be the depletion width divided by the cell size Δx. Since the depletion width varies along the rib height, the number of depletion cells along the rib width for each cell along the rib height needs to be calculated. The method to do this is presented below for the P-rib top and can be easily extended to other sections.

Since the rib height distance varies with N_θ and with voltage for the same N_θ, the number of rib height cells is not known *a priori*. The increment in the rib height distance corresponding to the increment in θ is

$$\Delta x_{pt} = \frac{x_{pt}\left(\theta = \frac{-\pi}{2}\right) - x_{pt}\left(\theta = 0\right)}{N_\theta} \tag{4.10}$$

Since $x = -\infty$ at $\theta = \frac{-\pi}{2}$, $N_\theta - 1$ values are used and (4.10) is written as

$$\Delta x_{pt} = \frac{x_{pt}\left(\theta = \frac{\pi(1-N_\theta)}{2N_\theta}\right) - x_{pt}\left(\theta = 0\right)}{N_\theta - 1} \tag{4.11}$$

The Δx_{pt} values are smaller than the cell size Δx, since the value of N_θ is much greater than the number of rib height cells. Therefore, multiple points will lie inside a single cell. Since a single cell can only be represented by a single value, the mean values of all x_{pt} and W_{Dpt}^{2D} points that lie inside the single cell will be calculated to obtain a single value for the 2D depletion region and rib height. The number of x_{pt} points that occupies a single cell is

$$N_{\Delta x_{pt}} = \frac{\Delta x}{\Delta x_{pt}} \tag{4.12}$$

The total number of cells along the rib height from the interface for which the depletion cells along the rib width will be calculated is

$$N_{x_{pt}} = \frac{N_\theta - 1}{N_{\Delta x_{pt}}} \tag{4.13}$$

The algorithm for calculating the mean values of x_{pt} and W_{Dpt}^{2D} is shown in Fig. 4.8. The number of depletion cells and the corresponding rib height cells are

$$W_{Dpt}^{2D}\Big|_{cells} = \frac{W_{Dpt}^{2D}\Big|_{av.}}{\Delta x} \tag{4.14a}$$

$$x_{pt}\Big|_{cells} = \frac{x_{pt}\Big|_{av.}}{\Delta x} \tag{4.14b}$$

Once the 2D depletion cells and the corresponding rib height cells are obtained, the next

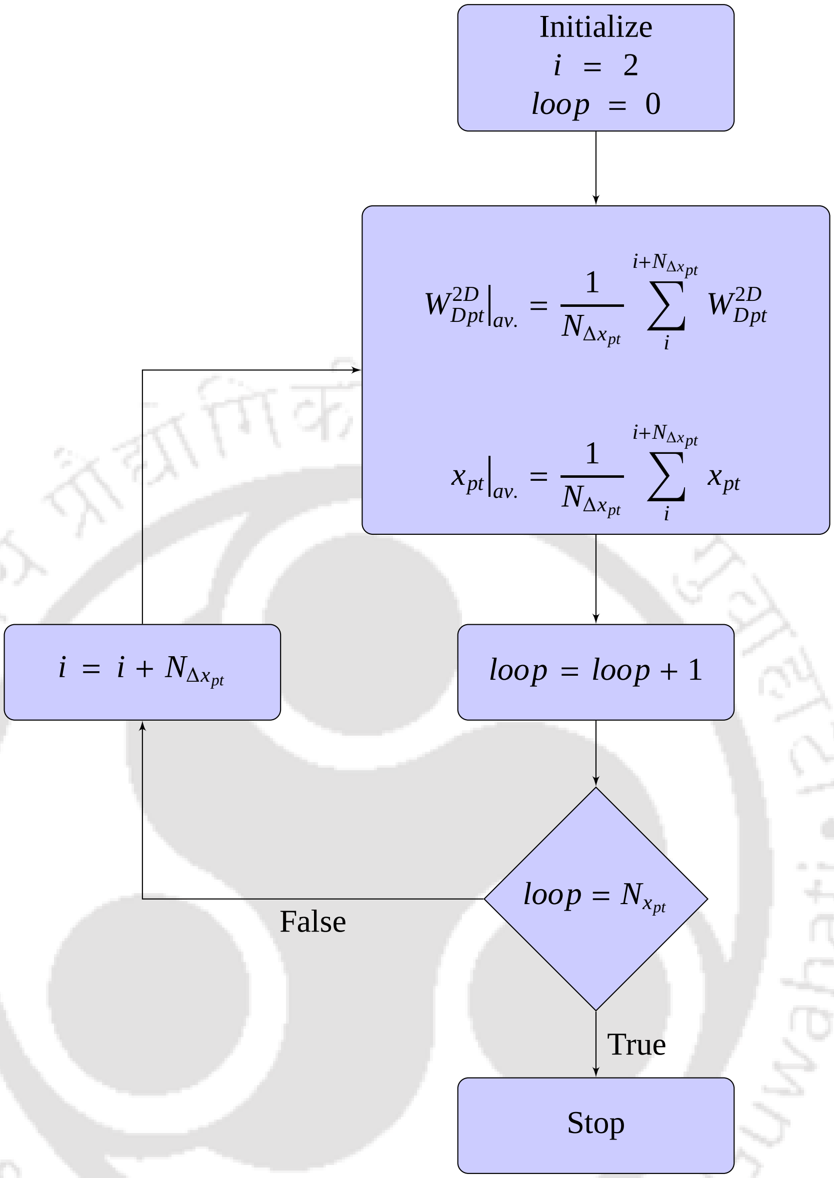

Fig. 4.8: Algorithm for 2D depletion width

step is to construct the P-rib and N-rib depletion region. The $W^{2D}_{Dpt}\big|_{cells}$ and $x_{pt}\big|_{cells}$ has $N_{x_{pt}}$ integer values. The absolute values of (4.14) are flipped so that the cell indexing starts from the PMD-silicon interface. The value of $x_{pt}\big|_{cells}$ at the interface is ‘0’ and needs to be changed to ‘1’ since it represents the cell number at the interface. The corresponding cells are put in an array of size $\frac{H_{rib}}{2\Delta x}$ starting from the interface. The empty cells are initialized with the previous cell value. The same procedure is followed for the other three rib sections. The P-rib (N-rib) depletion is formed by joining the P-rib (N-rib) top and P-rib (N-rib) bottom cells. Finally, since at lower reverse voltages and small values of N_{θ}, there are non-empty cells in the middle of the

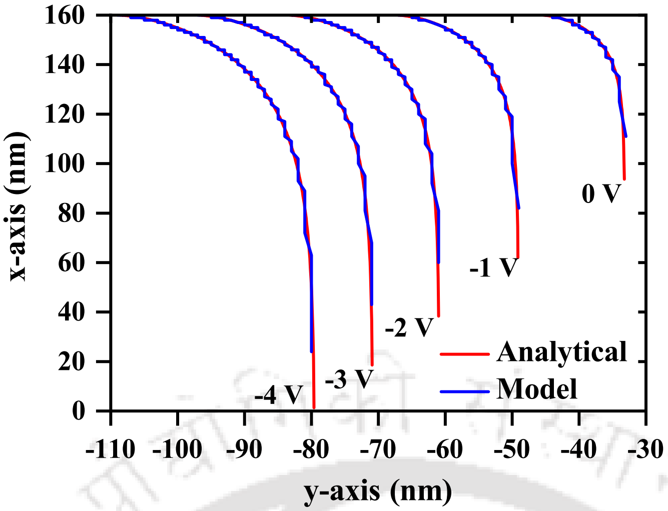

Fig. 4.9: 2D depletion width of P-rib top at different reverse bias voltages calculated using the model and analytic formula given by (4.6); H_{rib} = 320 nm.

rib, which are initialized with the 1D depletion width calculated from (4.5). The 2D depletion width calculated using the model for P-rib top is compared with the analytical form given by (4.6) and is shown in Fig. 4.9 for different reverse bias voltages. A good fit of the 2D depletion width calculated using the model with the analytical formula given in [143] can be observed.

The PN junction position is calculated as

$$\zeta = \frac{W_{rib} + \zeta_0}{2\Delta x} \tag{4.15}$$

where ζ_0 is positive for wider P-rib and negative for wider N-rib. $\zeta_0 = 0$ implies that the junction is in the middle. The cells to the left of the junction are made P-type by initializing the cell values with N_a. Similarly, the cells to the junction right are made N-type by initializing the values with N_d. The P (N) 2D depletion cells are subtracted (added) from (to) the junction and initialized to zero to create the rib area.

4.5 Performance Metrics

The refractive index change at any reverse bias voltage and wavelength is calculated as [115]

$$\Delta n = -\left(8.8 \times 10^{-22} \Delta N_e + 8.5 \times 10^{-18} (\Delta N_h)^{0.8}\right)\left(\frac{n_{Si}^{1550}}{n_{Si}^{\lambda}}\right)\left(\frac{\lambda}{1550}\right)^2 \tag{4.16}$$

The phase shift is calculated as

$$\Delta\phi = \frac{2\pi L}{\lambda} \sum_{area}\sum \Delta n \, |E^y|^2 \tag{4.17}$$

where $|E^y|^2$ is extracted from (4.1).

The change in free carrier absorption (FCA) at different bias voltages is given as

$$\Delta\alpha_{FCA} = \left[8.5\times10^{-18}\Delta N_e + 6.0\times10^{-18}\Delta N_h\right]\left(\frac{n_{Si}^{1550}}{n_{Si}^{\lambda}}\right)\left(\frac{\lambda}{1550}\right)^2 \tag{4.18}$$

The total absorption is calculated as

$$\alpha = \alpha_{scat} + \sum_{area}\sum \alpha_{FCA} \, |E^y|^2 \tag{4.19}$$

Other phase shifter metrics are determined as given in section 2.9.1

4.6 Model validation and device optimization

The 2D model is validated with TCAD simulation. A test structure is taken with waveguide dimension $W_{rib} \times H_{rib} \times H_{slab} = 500 \times 250 \times 50$ (in nm × nm × nm), $\lambda = 1550$ nm, oxide PMD, and $J_o = 0$ nm. The model algorithm is written in MATLAB, and the simulation runtime of the test structure with $N_\theta = 5000$ and $\Delta x = 1$ nm is ~66 seconds in 2nd Generation Intel® Xeon® server with 32 GB RAM. The EIM took ~56 seconds out of the total runtime to compute the mode fields, and the scattering loss since multiple slab waveguides with varying thickness need to be solved. For a particular waveguide dimension and wavelength, the mode parameters and scattering loss can be saved and separately loaded to run the model for PN diode parameter variation, which reduces the runtime to below 15 seconds. The EIM can itself be optimized by taking a lesser number of points to solve the transcendental equation of TE and TM slab waveguides [144].

Numerical simulation has been done using Synopsys® TCAD [125] with the same parameter values as the test structure, and the comparison is shown in Fig. 4.10. The P and N doping concentration are varied, and the phase shift and absorption loss per unit length are plotted as a function of wavelength. In order to validate EIM for accurately describing the waveguide mode field, both EIM and QV-FDM has been used to calculate the modal overlap with the depletion region in TCAD simulation and is shown in Fig. 4.10. The test structure with PN doping concentration 5×10^{17} cm^{-3} is then compared with another phase shifter with dimension $400 \times 200 \times 50$, $\lambda = 1310$ nm, and PN doping 1×10^{18} cm^{-3}. All other parameters are the same as the test structure. The phase and absorption curves are shown in Fig. 4.11. It can be seen from both Fig. 4.10 and Fig. 4.11, that EIM gives as good a result as that of the numerical QV-FDM. The model shows good agreement with TCAD simulation for the phase-voltage curve. In the case of the absorption-voltage curve, the model overestimates the value of absorption loss at higher doping concentrations compared to TCAD simulation, even though the same method has been used to determine the loss. This is because the extracted carrier concentration from the TCAD

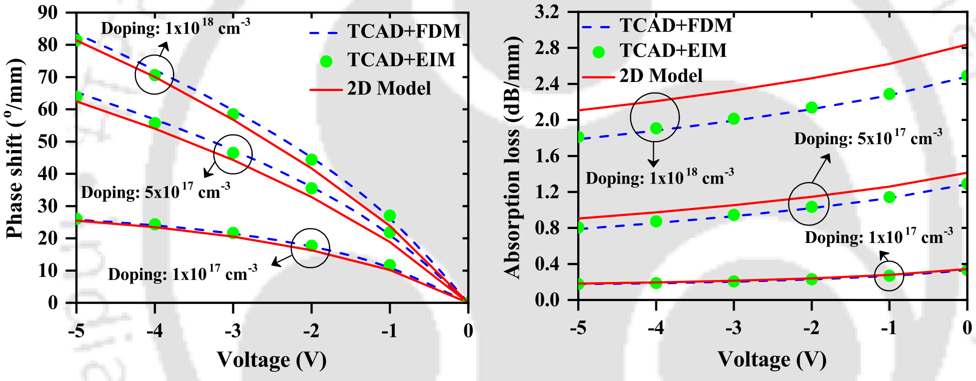

(a) (b)

Fig. 4.10: Comparison of 2D model and 2D TCAD simulation for different doping concentrations (a) Phase shift per unit length and (b) Absorption loss per unit length (the P and N doping concentrations are equal).

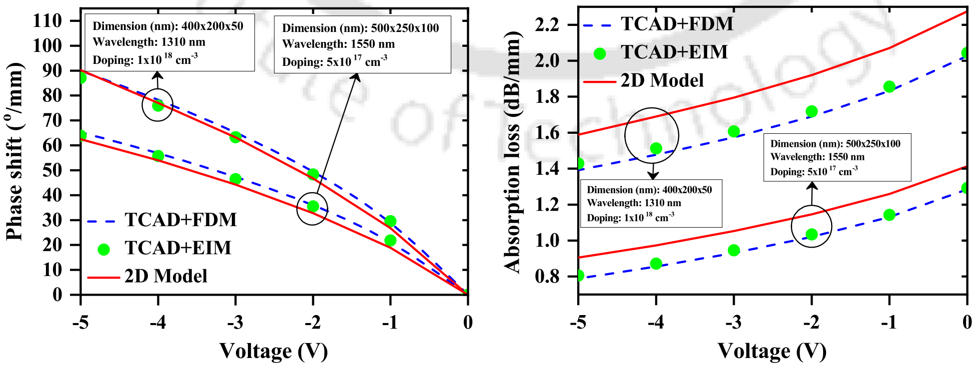

(a) (b)

Fig. 4.11: Comparison of 2D model and 2D TCAD simulation for different structures with different dimension, wavelength, and doping parameters (a) Phase shift per unit length and (b) Absorption loss per unit length (the P and N doping concentrations are equal).

simulation is lower than the doping concentration as an incomplete ionization model has been taken. Overall, good agreement between the 2D model and TCAD has been observed.

The model is used to optimize the phase shifter. The first step is to design a single-mode waveguide. The PMD layer is oxide, and the wavelength is 1550 nm. The top silicon thickness of the SOI substrate (H_{rib}) is taken as 250 nm. The minimum required slab height for different rib widths to attain single-mode operation is shown in Fig. 4.12(a) along with the corresponding scattering loss. At larger W_{rib}, larger H_{slab} is required so that the higher-order modes leak to the slab. The mode confinement is ~75% for all W_{rib} and corresponding H_{slab}. The scattering loss increases with lower W_{rib} and H_{slab}. This is because as W_{rib} decreases, the mode becomes less confined, and larger modal overlap with the sidewalls occur [145]. Also, as H_{slab} decreases, the rib sidewall height ($H_{rib} - H_{slab}$) increases, and scattering takes place over larger etch depth,

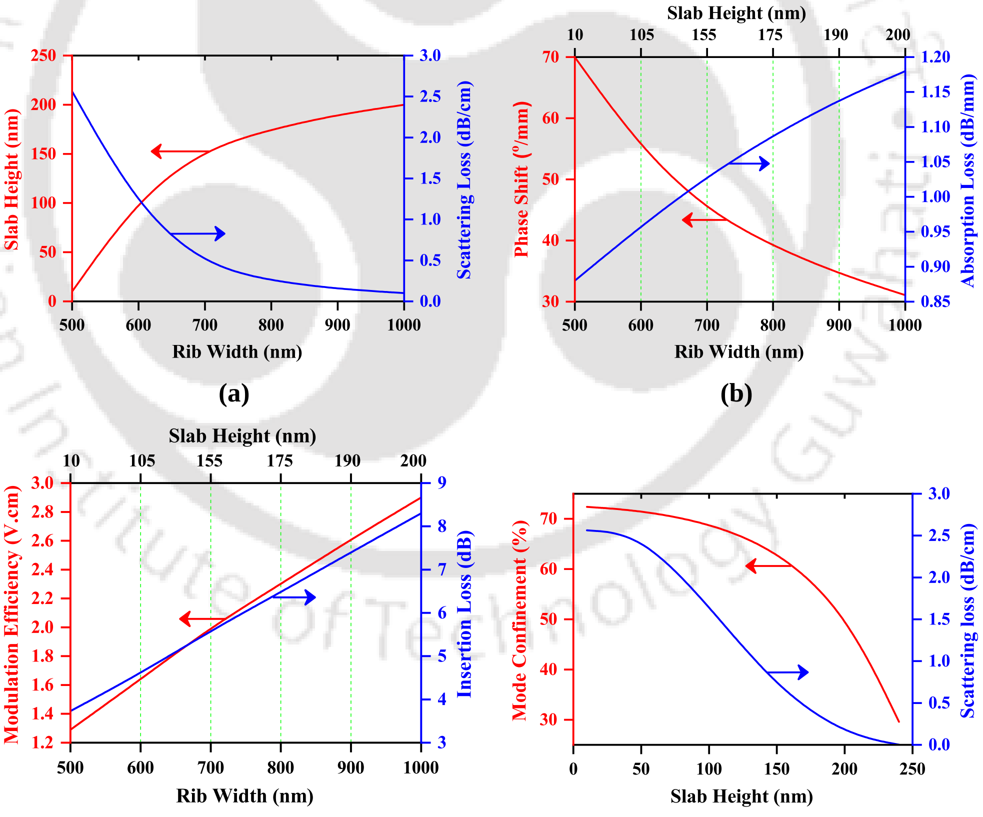

(a) (b)

(c) (d)

Fig. 4.12: (a) Minimum slab height for varying rib width to achieve single mode propagation (left) and corresponding scattering loss (right), (b) Phase shift per unit length (left) and absorption loss per unit length (right) at -5 V, (c) Modulation efficiency (left) and insertion loss (right) at -5 V, and (d) Mode confinement (left) and scattering loss (right) for varying slab height at W_{rib} = 500 nm.

which leads to an increase in the scattering loss. From Fig. 4.12(a), it seems that a larger W_{rib} and H_{slab} is better since the scattering loss is much lower. However, since the mode confinement is nearly the same, the peak mode intensity is greater for smaller W_{rib} due to a smaller cross-sectional area. This can be seen in Fig. 4.12(b) and (c) which plots the phase shifter performance metrics at -5 V with varying W_{rib} and corresponding H_{slab}. The PN doping is 5×10^{17} cm^{-3} with the junction in the middle. It can be seen that the phase shift per unit length increases with decreasing rib width due to an increase in the peak mode intensity of the fundamental quasi-TE mode. The absorption loss decreases with decreasing W_{rib} due to less number of total carriers over the rib area. The modulation efficiency and insertion loss both decrease, which is due to smaller required phase shifter length for π phase shift. Thus, a smaller rib width gives better phase shifter performance. The rib width is selected as 500 nm, and to select H_{slab}, the mode confinement and scattering loss are calculated with increasing slab height, as shown in Fig. 4.12(d). The slab height is varied from 10 nm to 240 nm, and it can be observed that the mode confinement and scattering loss both decrease due to mode leakage to the slab, and smaller etch depth, respectively. A trade-off between the mode confinement and scattering loss can be seen, and H_{slab} = 100 nm is selected with mode confinement of ~70% and scattering loss of ~1.66 dB/cm.

The waveguide is doped with 5×10^{17} cm^{-3} boron and phosphorus, each with the junction at the middle and the phase shifter metrics are calculated as shown in Fig. 4.13(a) and (b) for varying reverse bias voltages. The phase shift per unit length increases and absorption loss per unit length decreases with increasing reverse bias voltage due to an increase in the depletion width. The modulation efficiency increases and the insertion loss decreases with an increase in the reverse bias voltage. Next, to optimize the structure, the junction offset is varied from -100 nm (wider N-rib) to 100 nm (wider P-rib), and the phase shifter metrics are determined as shown in Fig. 4.13(c) and (d). At ζ_0 = 0 nm, the mode center coincides with the junction. Moving the junction left (right) leads to peak modal overlap with the N (P) depletion region. Since holes cause larger refractive index variation compared to electrons as evident from (4.16), the phase shift increases as the junction is moved from left to right. Moving the junction left

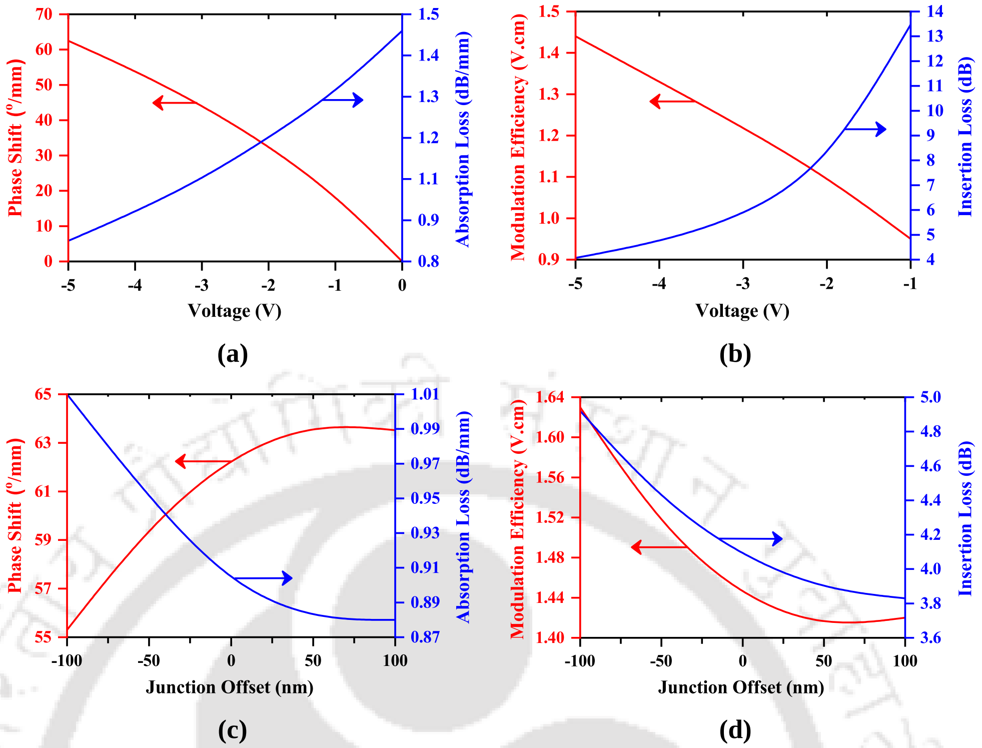

Fig. 4.13: Phase shift per unit length (left), absorption loss per unit length (right) [(a),(c)] and modulation efficiency (left), insertion loss (right) [(b),(d)]; for varying V at ζ_0 = 0 nm [(a),(b)] and varying J_o at V = -5 V.

to right decreases the absorption loss. The insertion loss and modulation efficiency decrease as the P-rib is made wider. As P-rib width continues to increase, the performance diminishes since the mode overlap with the depletion region begins to decrease. Optimum performance is achieved for J_o = 50 nm with ~64°/mm phase shift, ~0.88 dB/cm absorption loss, ~1.41 V.cm modulation efficiency, and ~3.83 dB insertion loss at -5 V. Further optimization can be made by varying the PN doping concentrations or by unequal doping in the P and N regions to enhance the phase shifter performance.

4.7 Summary

A 2D model is presented, which can be used for design, analysis, and optimization of a silicon optical PN phase shifter with a lateral junction. The model is fast, efficient, and shows good agreement with numerical TCAD simulation. The effect of design parameters on the phase shifter performance can be studied, which includes operating wavelength, waveguide dimensions, cladding material, doping concentrations, junction offset, and applied voltage. The phase shifter performance metrics, viz., phase shift per unit length, absorption loss, modulation efficiency, insertion loss, are calculated from the 2D modal overlap with the waveguide area. The modal parameters are determined using the effective index method. The model takes into account the widened depletion region at the core-cladding interface, and the algorithm to model the 2D nature of the depletion region is presented in detail. This can be extended to include vertical junction phase shifters, different core-cladding materials, and modulator parameters like bandwidth, extinction ratio, etc.

5

Silicon Optical Modulator: Quasi-TM Mode Modulation

Contents

5.1 Introduction

Most of the studies present in literature utilize the quasi-TE mode for modulation with the rib width kept larger than the rib height. Such waveguides are designed to have the quasi-TM mode cut-off with only the fundamental quasi-TE mode propagating. For a quasi-TM mode propagation with quasi-TE mode cut-off, the rib height should be larger than the rib width. A quasi-TM mode modulator using hybrid silicon – vanadium dioxide slot waveguide is reported in [146]. The rib width is 200 nm, with seven layers stacked on top of a silicon dioxide substrate with a total height of 490 nm. Some studies have investigated both quasi-TE and quasi-TM modulation, where the rib height is comparable to the rib width so that both modes are supported [147, 148].

5.2 Phase shifter structure

The rib height is made greater than the rib width to ensure the fundamental quasi-TM confinement is large, and the quasi-TE mode is cut-off. The cross-sectional view of the quasi-TM mode PN phase shifter is shown in Fig. 5.1. The waveguide parameters are given in Table 5.1.

H_{slab} plays an important role. Higher H_{slab} leads to mode leakage in the slab, thereby decreasing the mode confinement. Also, α_{scat} decreases due to lower etch depth. On the other

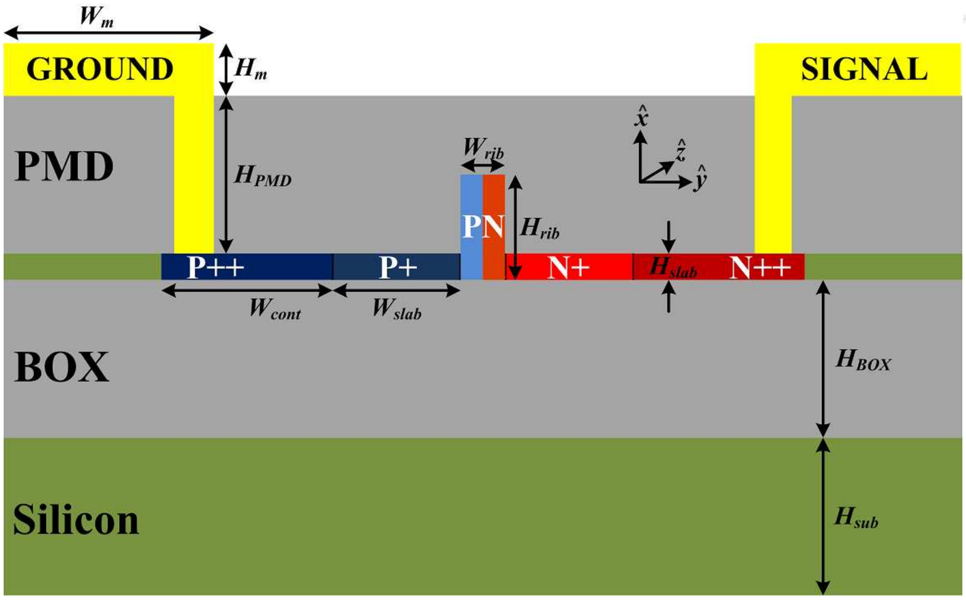

Fig. 5.1: PN phase shifter cross-section (the figure is not to scale).

Table 5.1: Waveguide parameters

Description	Symbol	Value
Metal contact width	W_m	5 μm
Metal layer thickness	H_m	1 μm
PMD layer thickness	H_{PMD}	2 μm
P++/N++ contact width	W_{cont}	1 μm
P+/N+ slab width	W_{slab}	0.5 μm
Rib width	W_{rib}	0.25 μm
Rib height	H_{rib}	0.5 μm
BOX layer thickness	H_{BOX}	2 μm
Silicon substrate thickness	H_{sub}	500 μm
P++ doping	N_A^{++}	1×10^{20} cm^{-3}
N++ doping	N_D^{++}	1×10^{20} cm^{-3}
P+ doping	N_A^{+}	5×10^{18} cm^{-3}
N+ doping	N_D^{+}	5×10^{18} cm^{-3}
P doping	N_A	5×10^{17} cm^{-3}
N doping	N_D	5×10^{17} cm^{-3}

hand, a larger H_{slab} decreases the series resistance leading to a higher RC bandwidth. The proper selection of H_{slab} is important and should take care of the trade-off between mode confinement and α_{scat}. α_{scat} in the designed waveguide cannot be neglected as the rib height is larger, leading to a considerable α_{scat}, which may be higher than α_{fca}.

H_{slab} is varied between zero (strip waveguide) and H_{rib} (slab waveguide). The parameter r is defined as the ratio of the slab height to the rib height ($r = H_{slab}/H_{rib}$) and ranges from 0 (strip waveguide) to 1 (slab waveguide). In quasi-TE phase shifters, the effect of H_{slab} on the phase shifter performance metrics is more prominent since the value of H_{rib} is small, typically between 220 nm to 300 nm [75, 76]. In the proposed quasi-TM phase shifter, the confinement

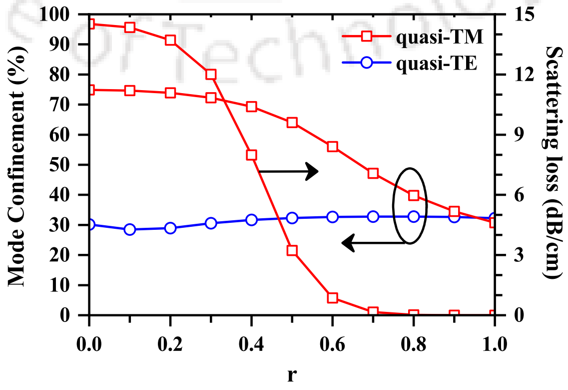

Fig. 5.2: Mode confinement and scattering loss of the proposed phase shifter as a function of the parameter r.

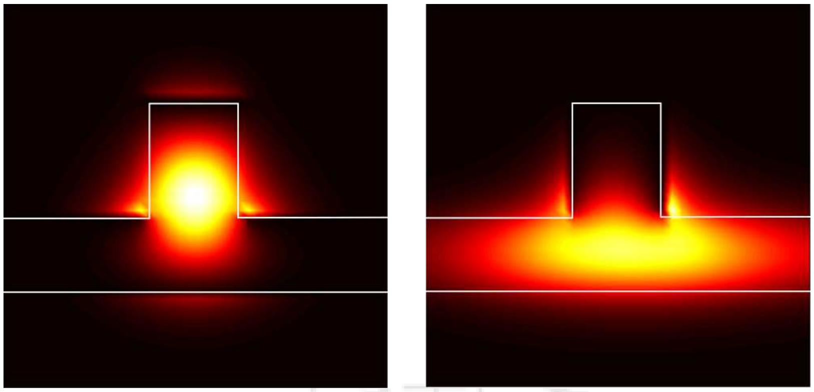
(a) **(b)**

Fig. 5.3: Mode profile of fundamental (a) quasi-TM mode and (b) quasi-TE mode.

remains roughly constant at smaller H_{slab}. This can be observed in Fig. 5.2, which shows the quasi-TM mode confinement, quasi-TE mode confinement, and quasi-TM scattering loss as a function of r. α_{scat} decreases with an increase in r (or H_{slab}) due to reduced etch depth, as seen from Fig. 5.2. The quasi-TM mode is well confined at lower r and leaks to the slab as r increases. The quasi-TE mode confinement is very less owing to lower W_{rib} compared to H_{rib} and is essentially cut-off. An optimum value of $r = 0.4$ is chosen corresponding to 200 nm slab height with ∼70% mode confinement and 7.99 dB/cm scattering loss. The mode profile of the fundamental quasi-TM and quasi-TE mode for $r = 0.4$ at a wavelength of 1550 nm is shown in Fig. 5.3. It can be observed that the quasi-TM mode is well confined, whereas, the quasi-TE mode propagates as the slab mode with mode confinement of ∼31%.

5.3 Phase shifter metrics

The phase shift per unit length and absorption loss per unit length of the designed quasi-TM phase shifter is shown in Fig. 5.4. The quasi-TM phase shifter is compared with a quasi-TE phase shifter of cross-section 500 nm (width) × 250 nm (height). The slab height of the quasi-TE phase shifter is 100 nm, thereby keeping the value of r the same as the quasi-TM phase shifter. All other parameters shown in Table 5.1 are kept the same for the quasi-TE phase shifter. The comparison is made by altering the rib height and width of the quasi-TM and quasi-TE phase shifters to obtain optimum performance for respective phase shifters. The quasi-TE phase shifter has quasi-TE mode confinement of ∼70% and quasi-TM mode confinement of

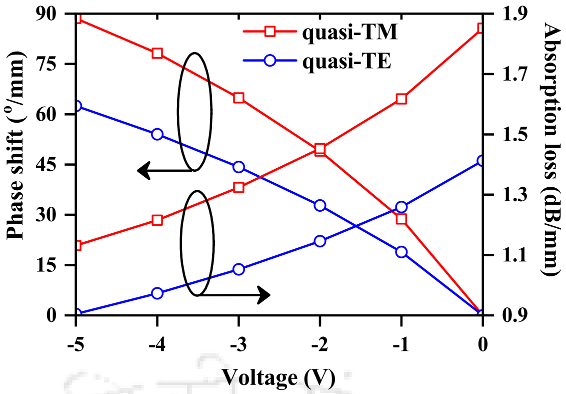

Fig. 5.4: Phase shift per unit length and absorption loss per unit length.

~30%. Both the quasi-TM and quasi-TE phase shifter have the same mode confinement of the corresponding guided mode.

The scattering loss of the quasi-TE phase shifter is 1.66 dB/cm, which is lower than the corresponding scattering loss of the quasi-TM phase shifter. This is because the etch depth is lower due to lower H_{rib} of the quasi-TE phase shifter. The FCA of the corresponding quasi-TM and quasi-TE phase shifters at 0 V are 10.52 dB/cm and 12.47 dB/cm, respectively. Though the FCA loss of the quasi-TM phase shifter is lower than the quasi-TE phase shifter, the total loss is larger, due to higher α_{scat} of the quasi-TM phase shifter. This can be seen from Fig. 5.4. The phase shift per unit length of the quasi-TM phase shifter is higher than the quasi-TE phase shifter. This is due to the waveguide structure employed for the quasi-TM phase shifter. Both the phase shifters have the same corresponding mode confinement and the same PN junction doping concentration. The quasi-TM phase shifter has a modal overlap with the depletion region over a larger area due to larger H_{rib}. The phase shift increases non-linearly with reverse bias voltage. At larger reverse bias, the depletion width widens, resulting in a larger phase shift. The non-linear behavior is due to the square root dependency of the depletion width on the bias voltage. The absorption loss decreases at larger reverse bias voltage since carrier depletes over larger width. The L_π for the quasi-TM and quasi-TE phase shifters at -5 V are 2.03 mm and 2.88 mm, respectively. The corresponding $V_\pi L_\pi$ of the quasi-TM phase shifter at -5 V is 1.02 V.cm compared to 1.44 V.cm of the quasi-TE phase shifter. Though the absorption per unit length of the quasi-TM phase shifter is higher, the total absorption is lower due to smaller L_π. The absorption loss at -5 V of the quasi-TM and quasi-TE phase shifters are 2.29 dB and 2.61 dB, respectively. The insertion loss for π phase shift at -5 V is 3.76 dB and 4.07 dB, respectively, for the quasi-TM and quasi-TE phase shifters.

The phase shifter performance metrics of the quasi-TM phase shifter is better compared to the quasi-TE phase shifter. The advantage is due to the structure employed for the quasi-TM phase shifter with the rib height larger than the quasi-TE making the interaction area of the mode with the lateral PN depletion region larger. The same can be achieved with the quasi-TE phase shifter by creating a vertical PN junction instead of a lateral PN junction [149], however, at the cost of complicated process flow. The quasi-TM phase shifter structure offers another advantage compared to the quasi-TE phase shifter in terms of the bandwidth. The larger H_{slab} results in smaller series resistance. The depletion capacitance (C_d) per unit length is higher for the quasi-TM phase shifter compared to the quasi-TE phase shifter due to the larger H_{rib}. This can be seen from Fig. 5.5. The capacitance of the quasi-TM phase shifter reduces from 8.60 pF/cm at 0 V to 3.62 pF/cm at -5 V.

5.4 MZM transfer characteristics

The Mach-Zehnder modulator (MZM) is driven in dual-arm push-pull configuration. The intensity contour plot calculated using (2.8) as a function of the MZM arm voltages is shown in Fig. 5.6(a) for 1 mm phase shifter length. Two points along the diagonal of Fig. 5.6(a) namely

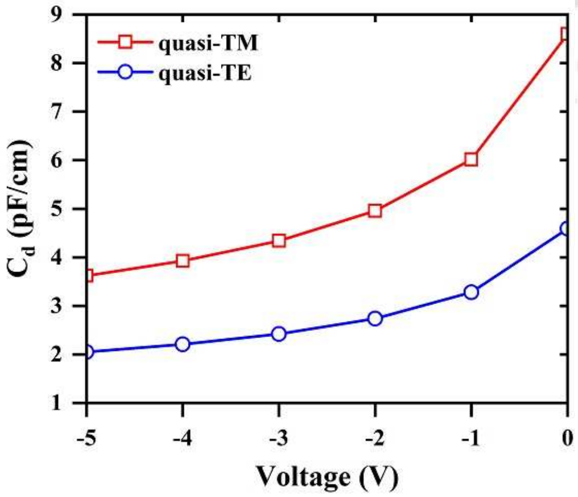

Fig. 5.5: Depletion capacitance.

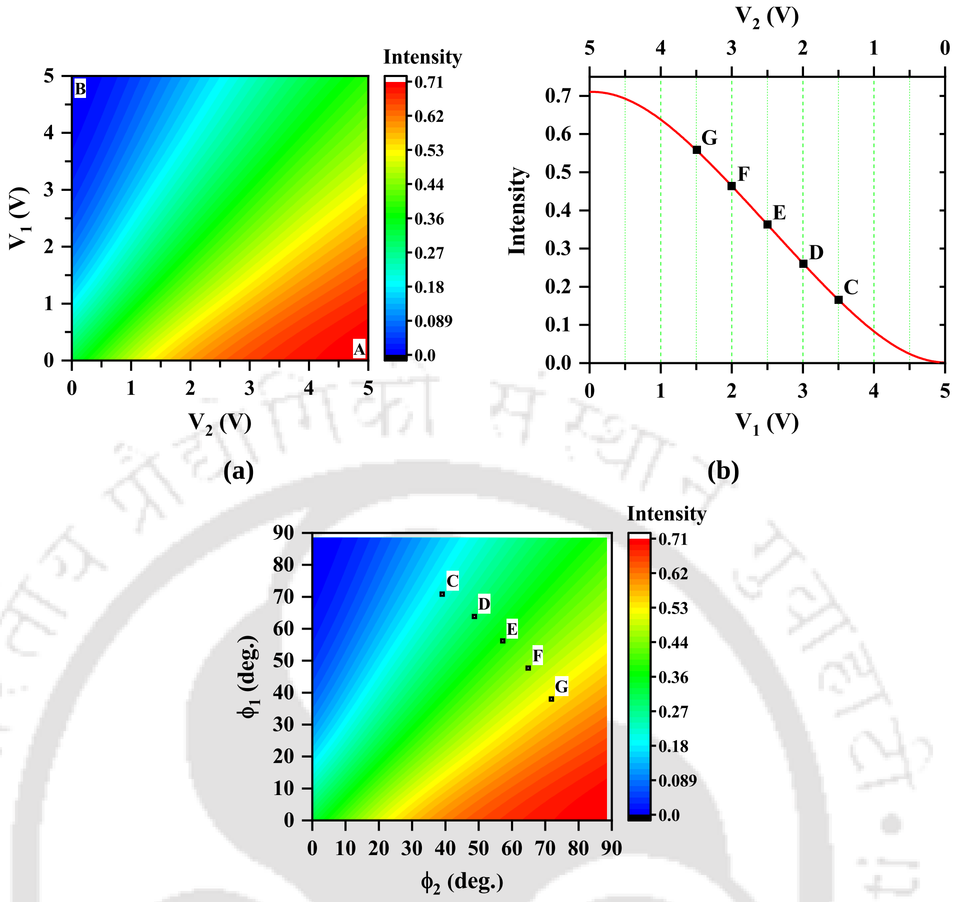

(a)

(b)

(c)

Fig. 5.6: Normalized output intensity (a) contour plot as a function of voltage change in both arms, (b) line plot along the diagonal **A** – **B**, and (c) contour plot as a function of phase change in both arms.

A and **B** is used to plot the transfer characteristic line plot as shown in Fig. 5.6(b). The intensity is the normalized output intensity. For single-arm drive, a 2 mm phase shifter is required to obtain full light extinction. However, since the drive is dual push-pull with the arms undergoing $+\pi/2$ and $-\pi/2$ phase shift, a 1 mm phase shifter can be used, thereby enhancing the modulator bandwidth. The modulator DC bias point and driving RF voltages are determined from the linear region of Fig. 5.6(b). Point **E** is selected as the bias point with $V_{DC1} = V_{DC2} = 2.5$ V. The driving RF voltages are selected as 1 V_{pp} (**D** – **F**) and 2 V_{pp} (**C** – **G**). It should be noted that the voltages shown in Fig. 5.6(a) and (b) are the voltages applied to the cathode of the PN phase shifter and are, therefore, positive values. For push-pull operation, $V_{RF1} = -V_{RF2}$. The corresponding phase shifts in the two arms for the points **C** to **G** of Fig. 5.6(b) is shown in Fig. 5.6(c). It can be observed that the phase change is not linear with a linear change in voltage points. The DC ER for 1 V_{pp} and 2 V_{pp} drive are 2.48 dB and 5.27 dB, respectively.

5.5 TWE analysis

The traveling wave electrode (TWE) is designed for the quasi-TM MZM in quadrature operation using the parameters given in Table 5.1. The detailed procedure is given in [61]. Different TWE parameters at 2.5 V reverse bias are shown in Fig. 5.7(a)-(d). The MZM frequency response (electro-optic EO S_{21}) is shown in Fig. 5.7(a). The 3 dB bandwidth can be determined from the EO S_{21} curve and represents the frequency where the phase shift is half of its DC value [150]. The 3 dB bandwidth is 74 GHz at 2.5 V reverse bias denoted by the dotted line. The electro-electro EE S-parameters (S_{11} and S_{21}) are shown in Fig. 5.7(b). EE S_{11} indicates the back reflection and is less than -7 dB over the simulated range. The EE S_{21} indicates the signal transmission loss [151]. If the velocity mismatch between the optical mode and RF signal is nil,

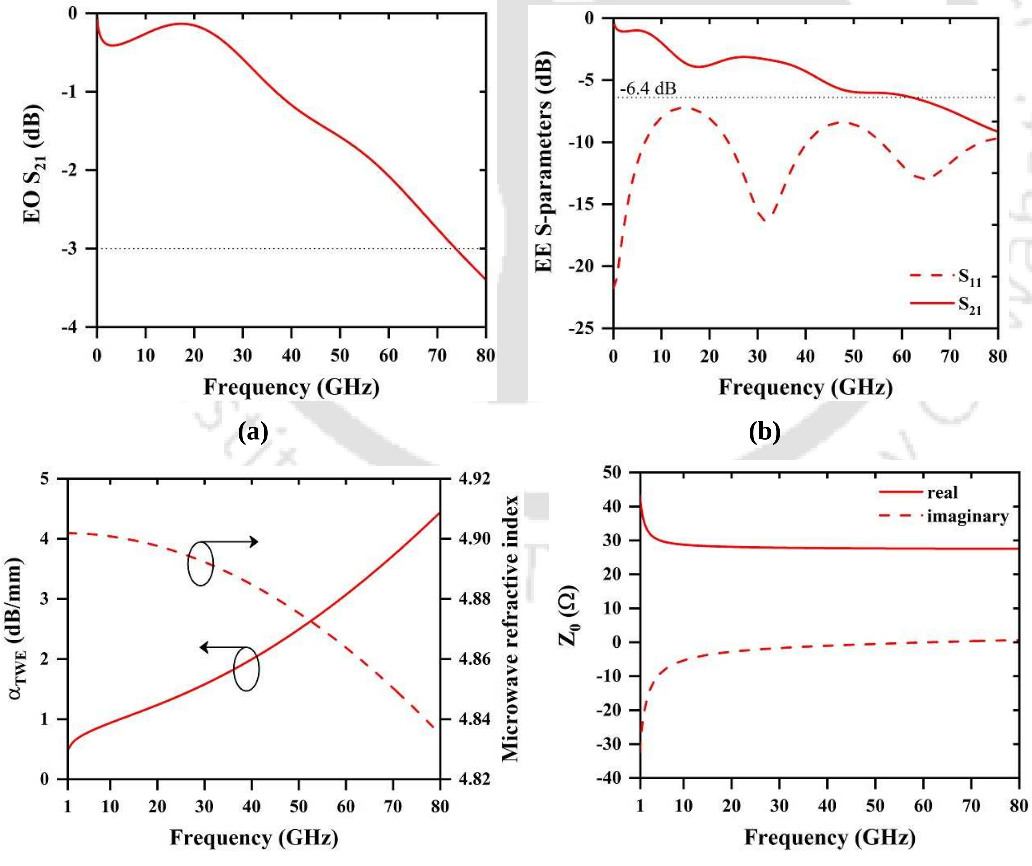

(c) (d)

Fig. 5.7: TWE parameters: (a) EO S_{21}, (b) EE S_{11}, (c) α_{TWE} and microwave refractive index, and (d) characteristic impedance (Z_0).

the -6.4 dB EE S_{21} point gives the -3 dB EO S_{21} bandwidth [152]. The -6.4 dB EE S_{21} bandwidth is 62 GHz denoted by the dotted line in Fig. 5.7(b). Fig. 5.7(c) shows the TWE attenuation (α_{TWE}) and microwave refractive index at different frequencies. The attenuation and microwave index at 74 GHz is 3.68 dB/mm and 4.84, respectively. The optical group index of the quasi-TM mode is 4.01. The characteristic impedance (Z_0) of the TWE is shown in Fig. 5.7(d). Z_0 at 74 GHz is $27.54 + 0.44i$ Ω. From the TWE graphs, it can be seen that the impedance matching of the TWE with R_S and R_T is poor. This results in high back reflection. The design can be made better by varying the TWE dimensions. However, the large rib height of the quasi-TM phase shifter reduces the flexibility of obtaining better performance. The bandwidth can be improved by using R_T = 25 Ω. The EO S_{21} -3 dB point increases to 141 GHz. The EE S_{11} falls below -10 dB and the -6.4 dB EE S_{21} bandwidth increases to 86 GHz. The α_{TWE} increases to 9.25 dB/mm at 141 GHz.

5.6 High-speed characteristics

The high-speed characteristics have been simulated in OptiSystem® v16.1.0. A dual-arm dual push-pull drive is employed using the non-return-to-zero on-off keying (NRZ-OOK) modulation scheme. Both PN junctions are reverse biased at 2.5 V and V_{RF} = 1 V_{pp} and 2 V_{pp} is used. A 1550 nm laser with 10 dBm power is used without any amplification at any stage. A pseudo random bit sequence (PRBS) with length 2^{15}-1 is used to generate the bit pattern. The bit error rate BER is determined for different data rates over a 1550 nm zero-dispersion single-mode fiber (SMF) of varying length and at different received power. The SMF attenuation is

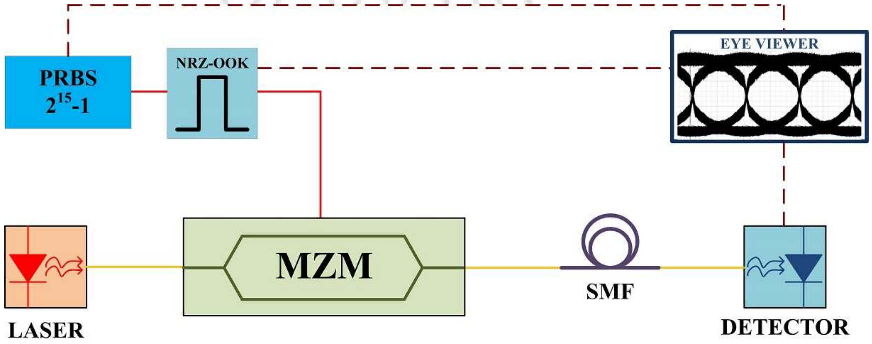

Fig. 5.8: Block diagram representation of the simulation setup.

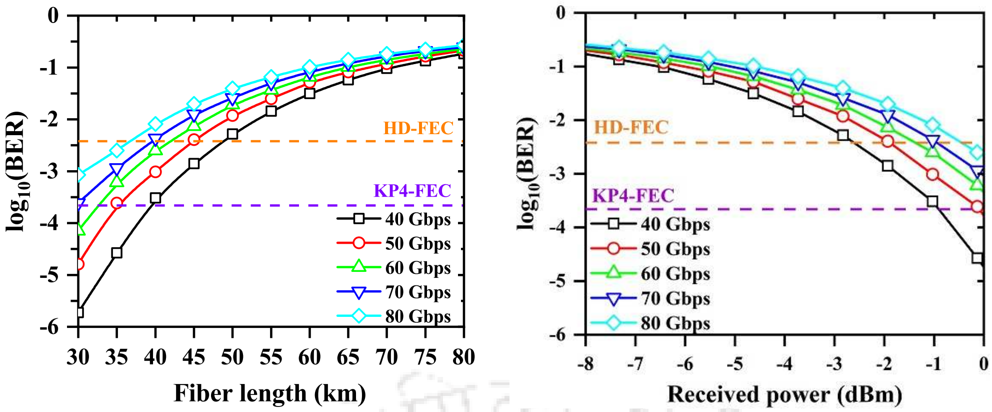

(a) **(b)**

Fig. 5.9: BER as a function of (a) SMF length and (b) received power, for V_{RF} = 1 V_{pp}.

taken to be 0.18 dB/km. The simulation setup is shown in Fig. 5.8.

The change in BER with a change in fiber length and received power are shown in Fig. 5.9(a) and (b) at 1 V_{pp} drive for data rates varying from 40 Gbps to 80 Gbps. The SMF length and the received power are varied from 30 km to 80 km and -8 dBm to 0 dBm, respectively. As the data rate increases, the BER increases with fiber length and decreases with received power. Two standard BER thresholds, the hard-decision forward error correction (HD-FEC) (BER = 3.8×10^{-3}) and the KP4-FEC (BER = 2.2×10^{-4}) are shown in Fig. 5.9. For 1 V_{pp} drive with BER below HD-FEC threshold, 40 Gbps transmission over SMF length < 48 km is possible and 80 Gbps transmission over SMF length < 35 km. The open eye diagrams at 1 V_{pp} drive over 30 km SMF transmission is shown in Fig. 5.10 for different data rates. The received power for BER below the HD-FEC should be greater than -2.8 dBm (-0.5 dBm) for 40 Gbps (80 Gbps) operation.

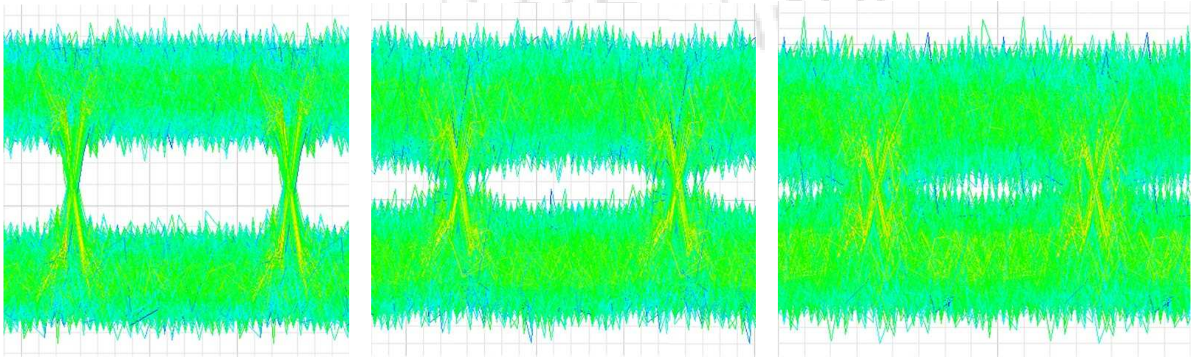

(a) **(b)** **(c)**

Fig. 5.10: Eye diagram for V_{RF} = 1 V_{pp} over 30 km fiber at (a) 20 Gbps, (b) 40 Gbps, and (c) 60 Gbps.

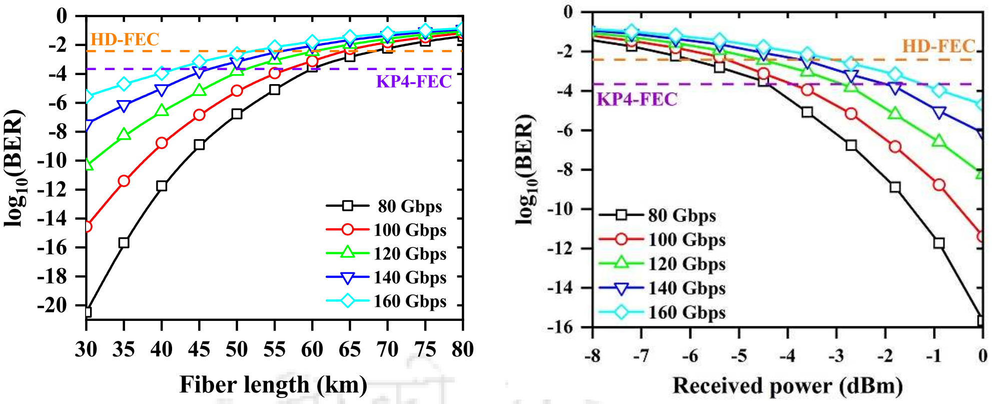

(a) **(b)**

Fig. 5.11: BER as a function of (a) SMF length and (b) received power, for V_{RF} = 2 V$_{pp}$.

The change in BER with SMF length and received power for 2 V$_{pp}$ drive are shown in Fig. 5.11(a) and (b) respectively. The data rate is varied from 80 Gbps to 160 Gbps. The SMF length and received power sweep are the same as before. The BER improves with higher drive voltage as expected, and thus higher data rates can be achieved. With BER below the HD-FEC threshold, 80 Gbps transmission over SMF length < 65 km is possible and 160 Gbps transmission over SMF length < 40 km. The open eye diagrams at 2 V$_{pp}$ drive over 50 km SMF transmission is shown in Fig. 5.12 for different data rates. The received power for BER below the HD-FEC should be greater than -4.5 dBm (-1.35 dBm) for 80 Gbps (160 Gbps) operation. The received power tolerance increases with an increase in the drive voltage, as can be expected.

The effect of fiber dispersion is studied by varying the dispersion from 0 ps.nm^{-1} to -100 ps.nm^{-1} for different SMF length at 2 V$_{pp}$ drive and 100 Gbps operation. The BER versus

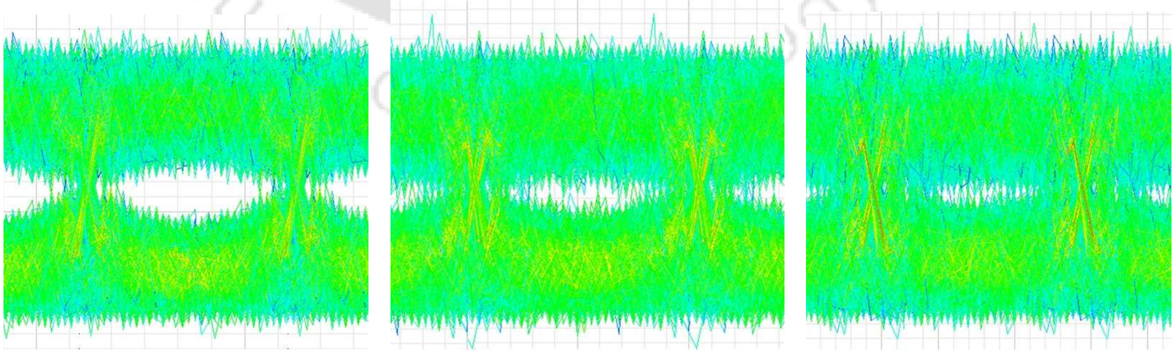

(a) **(b)** **(c)**

Fig. 5.12: Eye diagram for V_{RF} = 2 V$_{pp}$ over 50 km fiber at (a) 80 Gbps, (b) 100 Gbps, and (c) 120 Gbps.

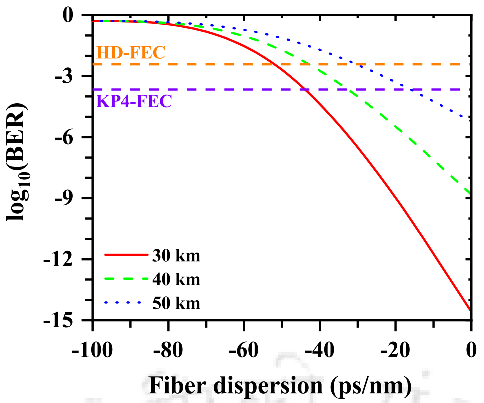

Fig. 5.13: Bit-error rate for varying fiber dispersion at 2 V_{pp} and 100 Gbps operation.

fiber dispersion is shown in Fig. 5.13. For BER less than the HD-FEC threshold at 100 Gbps transmission, the dispersion tolerance is ~ -1.73 ps.nm^{-1}.km^{-1}, ~ -1.08 ps.nm^{-1}.km^{-1}, and ~ -0.60 ps.nm^{-1}.km^{-1} for SMF lengths of 30 km, 40 km, and 50 km, respectively.

The power consumption for 1 V_{pp} drive and 2 V_{pp} drive is 18.15 mW and 72.62 mW, respectively. For 160 Gbps operation at 2 V_{pp} drive over 30 km SMF, the energy per bit (E_b) is 0.45 pJ/bit. It should, however, be noted that the above figure does not include the power consumption of the TO phase shifter.

The performance comparison of the designed MZM with recent literature is given in Table 5.2. The high performance of the designed modulator is due to the use of quasi-TM mode for propagation, instead of the quasi-TE mode. The large phase shift per unit length, along with the high bandwidth of the quasi-TM phase shifter, results in higher performance compared to a quasi-TE phase shifter. The series resistance of the quasi-TM phase shifter is lower due to larger H_{slab}, larger H_{rib}, and a smaller W_{rib} than a corresponding quasi-TE phase shifter with same cross-section and proportion. Also, the larger phase shift per unit length of the quasi-TM phase shifter results in a lower length.

Table 5.2: Mach-Zehnder modulator performance comparison

Ref.	Mode	$V_\pi L_\pi$ (V.cm)	*IL* (dB)	Bandwidth (GHz)	Mod.	V_{pp} (V_{bias}) (V)	L (mm)	Speed (Gbps)	ER (dB)	E_b (pJ/bit)
[148]*	TE	11 (-6 V)	7.7	27 (6 dB)	OOK	6 (-3)	1.35	40	6.5	4.5
	TM	14 (-6 V)	5.4							
[153]*	TE	2.7 (-9 V)	3.6	30	OOK	1.6 (0)	3	40	3.1	0.64
[91]*	TE	0.94 (-2 V)	2.7	13	OOK	2.88 (-2.4)	2	24	2.2	-
[154]*	TE	1.4 (-4 V)	4.4	58	OOK	5 (-6)	2	90	3.3	-
					PAM-4	0.5, 0.25 (-6)	2	112	2.7	-
This work**	TM	1.02 (-5 V)	3.76	74	OOK	2 (-2.5)	1	160	2.3	0.45

* Experimental result; ** Simulation result.

5.7 Summary

A silicon traveling-wave Mach-Zehnder modulator with quasi-TM mode propagation is studied for high-speed data communication. The quasi-TM PN phase shifter is shown to have better performance compared to a quasi-TE PN phase shifter of the same cross-section and parameters. The designed modulator is operated in quadrature using a dual-arm push-pull configuration. The modulation bandwidth is enhanced by using a traveling-wave electrode. The quasi-TM modulator has a bandwidth of 74 GHz at −2.5 V. The BER at different data rates are determined over single-mode fiber transmission and received power levels. The designed modulator achieves 160 Gbps OOK operation at 2 V_{pp} drive over 30 km fiber with an extinction ratio of 2.3 dB and BER of 2.77×10^{-06}. A dispersion tolerance up to -1.73 ps.nm^{-1}.km^{-1} for 100 Gbps operation over 30 km fiber transmission has been observed.

6

Silicon Optical Modulator: Enhancing Performance Using SiGe

Contents

6.1 Introduction

As stated in chapter 2, the free-carrier plasma dispersion (FCPD) effect results in the change in the refractive index, which leads to a change of phase and absorption coefficient. Decreasing the carrier concentration across a PN junction lowers the refractive index. In addition to carrier concentration change, the change in the refractive index depends on the material refractive index, the wavelength of light, and carrier effective mass. The absorption also depends on the carrier mobility. Introducing germanium (Ge) lowers the carrier effective mass, leading to enhanced FCPD effect. A higher Ge concentration will lead to a higher phase shift, which in turn decreases the phase shifter length required for π phase shift. This enhances the modulation bandwidth.

The efficiency of using Ge to enhance the FCPD effect depends on multiple factors. The maximum Ge mole fraction (x) that can be used depends on the wavelength of operation. For 1550 nm operation, the maximum mole fraction should be less than 0.33 to avoid material absorption. For $\mathrm{Si}_{1-x}\mathrm{Ge}_x/\mathrm{Si}$, the critical layer thickness decreases with increasing x, where the critical layer thickness is defined as the thickness beyond which strain relaxes by forming defects, leading to losses [155]. The layer is said to be pseudomorphic below the critical layer thickness. A defect-free thicker strained layer of larger mole fraction can be ensured by using multiple layers with a small step-index between successive layers. The mode maxima should coincide with the maximum Ge mole fraction layer.

The change in refractive index and absorption coefficient at 1550 nm for silicon is given in (2.4) which has been modified for the proposed structure by using the obtained strained layer parameters as given below:

$$\Delta n = -\left[8.8\times10^{-22}\Delta N_e\left(\frac{m_{ce}^{*si}}{m_{ce}^{*layer}}\right)+8.5\times10^{-18}(\Delta N_h)^{0.8}\left(\frac{m_{ch}^{*si}}{m_{ch}^{*layer}}\right)\right]\left(\frac{n^{si}}{n^{layer}}\right) \tag{6.1a}$$

$$\Delta\alpha = \left[8.5\times10^{-18}\Delta N_e\left(\frac{m_{ce}^{*si}}{m_{ce}^{*layer}}\right)^2\left(\frac{\mu_e^{si}}{\mu_e^{layer}}\right)+6.0\times10^{-18}\Delta N_h\left(\frac{m_{ch}^{*si}}{m_{ch}^{*layer}}\right)^2\left(\frac{\mu_h^{si}}{\mu_h^{layer}}\right)\right]\left(\frac{n^{si}}{n^{layer}}\right) \tag{6.1b}$$

Fig. 6.1: Graded rib structure. The grading is along the x-axis with each layer doped P and N to form the PN phase shifter shown in Fig. 2.4. Layer 1 being relatively long and supported by the BOX and silicon substrate is unstrained while layers 2, 3, and 4 experiences biaxial compressive strain and layers 5, 6, and 7 biaxial tensile strain.

6.2 Multi-layer SiGe phase shifter

6.2.1 Graded-index rib structure

The PN phase shifter structure is similar to Fig. 2.4, with W_{rib} = 500 nm, H_{rib} = 250 nm, and H_{slab} = 50 nm. The strained $Si_{1-x}Ge_x$ layers are grown along the (001) direction ($\hat{x}$-axis) one over the other with different mole fractions to form the graded-index structure. Fig. 6.1 shows the graded rib structure along with the mole fraction and thickness of each layer. Germanium mole fraction of 0.1, 0.2, and 0.3 have been used for the graded layers to avoid material absorption at 1550 nm, with the thickness of each layer kept below the critical layer thickness.

The cross-sectional mode profile and the refractive index along the $\hat{x}$-axis at 1550 nm are shown in Fig. 6.2(a) and (b) respectively. The waveguide supports a single E^y mode propagation with 2D mode confinement of 74.38%. The E^x mode is cut-off with a 2D mode confinement of 31.93%.

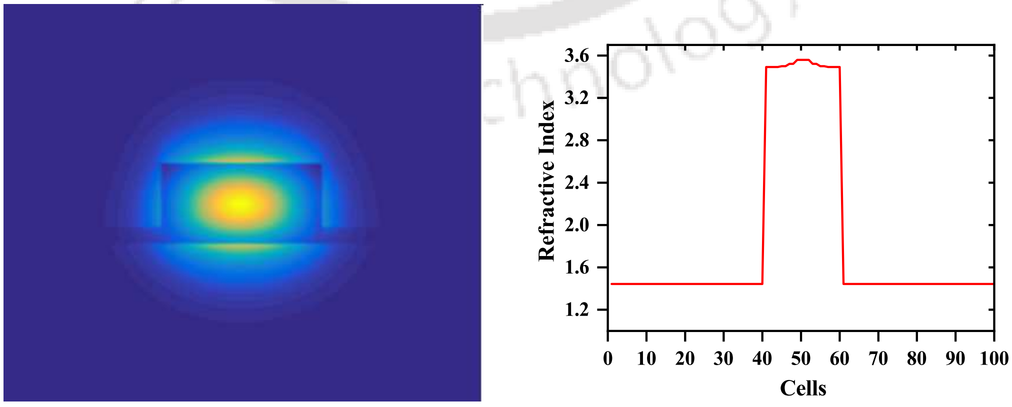

(a) (b)

Fig. 6.2: (a) Cross-sectional mode profile and (b) refractive index along waveguide height.

6.2.2 Band diagram

The band diagram, along with the hole and electron densities in the P and N rib regions across the waveguide height, is shown in Fig. 6.3(a)-(c) respectively. The valence band minimum and conduction band maximum lie in layer 4, which have the highest germanium mole fraction. Each layer is doped with boron and phosphorus to form the P and N regions with an equal doping concentration of 5×10^{17} cm^{-3}. However, due to the different energy levels of each layer, the localized carrier density across the device differs with higher electron (hole) concentration at layer with lower electron (hole) energy. The conduction and valence band discontinuities of different layers can be calculated using [156]. The boron and phosphorus-doped layers behave as a P-P and N-N heterojunction due to different layer properties. The heterojunctions are formed by accumulation and depletion of carriers on either side of each interface

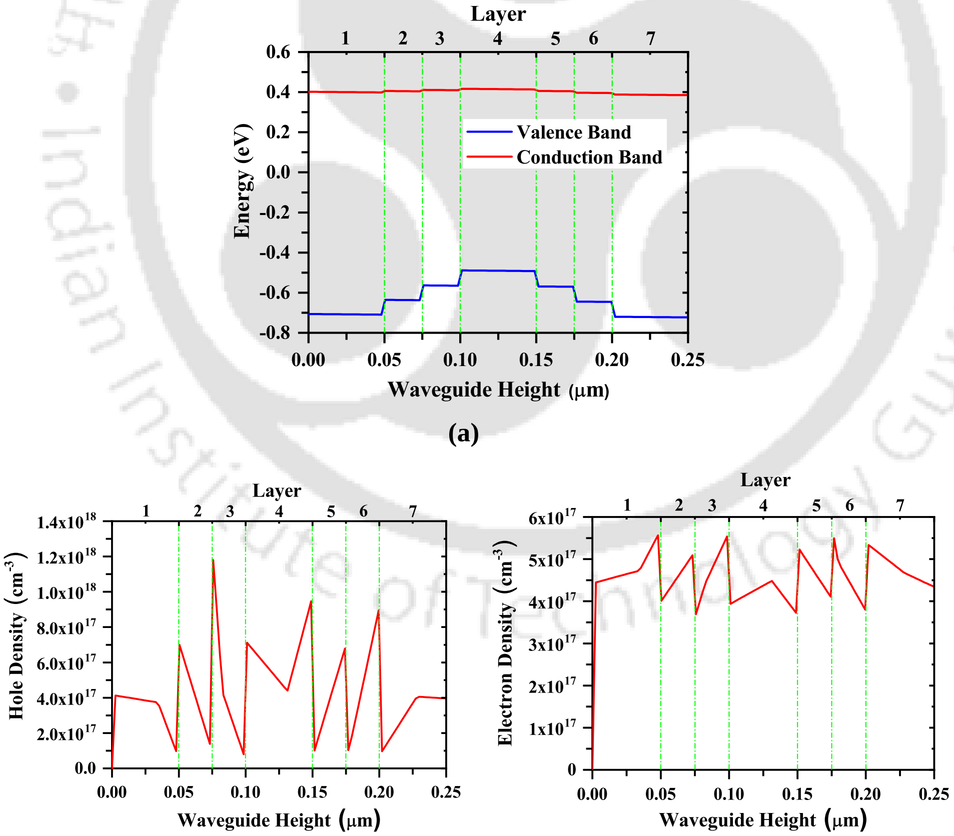

(a)

(b) (c)

Fig. 6.3: (a) Intrinsic band diagram showing valence and conduction band across multiple layers along waveguide height, (b) Hole equilibrium density in P-rib along waveguide height, and (c) Electron equilibrium density in N-rib along waveguide height. The dashed green lines in each figure demarcate the different layer interfaces. The layers are shown in the upper x-axis.

as seen from Fig. 6.3(b) and (c). For both P and N doped rib, a localized electric field exist from layer 4 to 1 and from layer 4 to 7, which can be interpreted from the carrier type and accumulation/depletion of carriers across each interface.

6.2.3 Material parameters

The material parameters of each graded layer have been extracted from the band structure calculated using the non-local empirical pseudopotential method (NL-EPM) and are shown in Fig. 6.4. Other methods that can be used to calculate the material parameters could be found in [157–160]. For the proposed device structure, strained layers are grown over strained layers

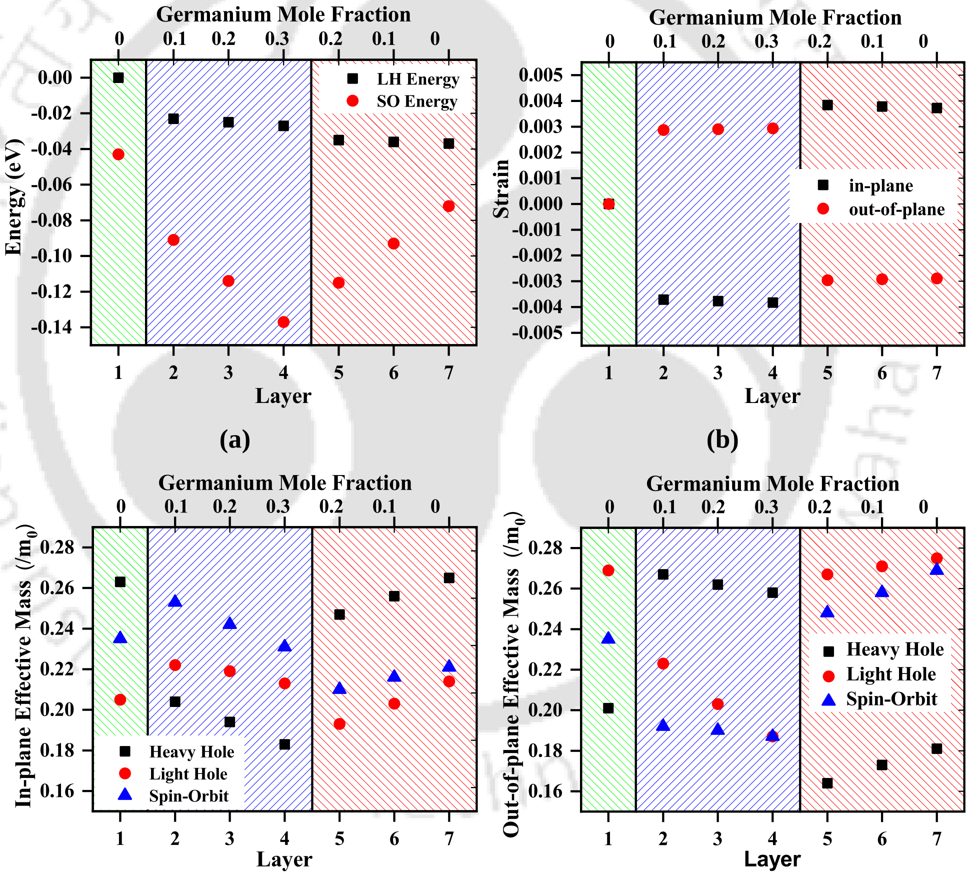

(a) (b) (c) (d)

Fig. 6.4: (a) Valence band energy at Γ (negative energy implies hole energy which increases downward), (b) Strain components, (c) In-plane hole effective mass, and (d) Out-of-plane hole effective mass. The plots are divided into three windows with green window representing unstrained material (Layer 1), blue window representing biaxial compressive strained material (Layer 2, Layer 3, Layer 4), and red window representing biaxial tensile strained material (Layer 5, Layer 6, Layer 7). The mole fraction for compressive strain (blue window) increases from left to right, whereas that for tensile strain (red window) increases from right to left as shown in the upper x-axis.

having different germanium mole fractions with half the layers experiencing tensile strain and the other half compressive strain. The pseudopotential form factors of silicon and germanium were taken from [161]. The strain causes the 6-fold degeneracy of the conduction band minima to separate into 2-fold and 4-fold degenerate bands. The effect of strain on the valence band is to break the HH and LH degeneracy at Γ point and cause a shift in the SO splitting energy. The shift in the energy of the LH and SO band along with the in-plane and out-of-plane strain and valence band effective masses of different layers are shown in Figs. 6.4(a)-(d). The change in material parameters for each strain type has been observed to be linear with mole fraction.

Fig 6.4(a) shows the valence band energies of the graded layers. The LH energy increases for compressive strain and decreases for the tensile strain with increasing mole fraction. The SO energy increases with increasing mole fraction irrespective of the type of strain. For strained $Si_{1-x}Ge_x$/strained $Si_{1-y}Ge_y$, strain is biaxial compressive for $x > y$ and biaxial tensile for $x < y$ which is evident from Fig. 6.4(b). The in-plane strain is negative, and the out-of-plane strain is positive for the compressive strain. The reverse is true for tensile strain. The effect of strain on the in-plane and out-of-plane effective mass of the HH, LH, and SO band is shown in Fig. 6.4(c) and (d) respectively. The in-plane and out-of-plane effective mass of all three valence bands decrease with increasing mole fraction for both strain type. A decrease and increase in the in-plane HH mass from unstrained to compressive strain and from compressive to tensile strain respectively, can be observed from Fig. 6.4(c). The opposite can be observed for the in-plane LH mass. The scenario for the HH and LH out-of-plane effective mass is opposite to the in-plane case, as shown in Fig. 6.4(d). The behavior of both in-plane and out-of-plane SO effective mass is similar to the LH mass.

6.2.4 Electrical equivalent circuit

The 3 dB modulation bandwidth can be determined from the phase shifter resistance and capacitance. The depletion width at the top and bottom oxide/semiconductor interface is widened, leading to a fringing electric field, which can be modeled as a capacitance in parallel to the junction capacitance. Apart from the PN junction depletion capacitance, the carrier accumulation/depletion across each layer interface can be modeled as a capacitance in parallel with

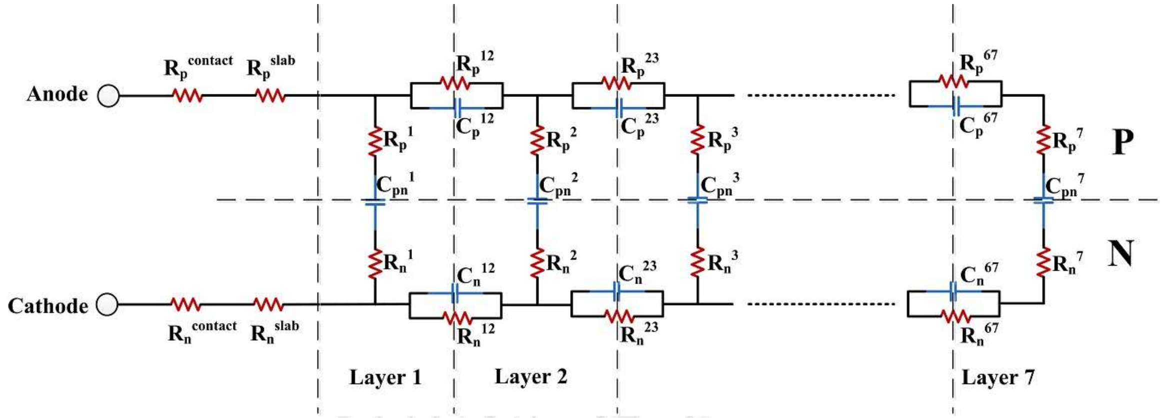

Fig. 6.5: Equivalent circuit model of the proposed phase shifter. The vertical dashed lines denotes each layer starting from layer 1 on the left and the horizontal dashed line separates the P and N doped regions. The P(N) region resistance and capacitances are denoted by subscript '*p(n)*'. The PN junction depletion capacitance of each layer is denoted by the subscript '*pn*'. The contact and slab resistance is denoted by the superscripts '*contact*' and '*slab*' respectively. Superscripts '*i*' and '*ij*' represents the layer and layer interfaces respectively.

resistance as carriers have to cross multiple layers to get collected by the end electrodes when a reverse bias is applied. The equivalent circuit of the multi-layer graded-SiGe phase shifter is shown in Fig. 6.5.

The contact resistance ($R^{contact}$) and slab resistance (R^{slab}) of the proposed structure can be calculated analytically using the approach given in [143] as

$$R^{contact} = R_p^{contact} + R_n^{contact} = \frac{1}{qH_{slab}L}\left[\frac{W_{P++}}{N_a^{contact}\mu_h^{contact}} + \frac{W_{N++}}{N_d^{contact}\mu_e^{contact}}\right] \tag{6.2a}$$

$$R^{slab} = R_p^{slab} + R_n^{slab} = \frac{1}{qH_{slab}L}\left[\frac{W_{Pslab}}{N_a^{slab}\mu_h^{slab}} + \frac{W_{Nslab}}{N_d^{slab}\mu_e^{slab}}\right] \tag{6.2b}$$

The layer and interface resistances can be similarly calculated as

$$R_p^i = \frac{W_{rib}^{p^i} - W_D^{p^i}}{qN_a^i\mu_h^i h_i L} \tag{6.3a}$$

$$R_n^i = \frac{W_{rib}^{n^i} - W_D^{n^i}}{qN_d^i\mu_e^i h_i L} \tag{6.3b}$$

$$R_p^{ij} = \frac{h_{ij}}{qN_a^{ij}\mu_h^{ij}L(W_{rib}^{p} - W_D^{p^{ij}})} \tag{6.3c}$$

$$R_n^{ij} = \frac{h_{ij}}{qN_d^{ij}\mu_e^{ij}L(W_{rib}^n - W_D^{n^{ij}})} \tag{6.3d}$$

The total phase shifter resistance is

$$R = R^{contact} + R^{slab} + R_p^{rib} + R_n^{rib} \tag{6.4}$$

The calculation of the heterojunction interface capacitance is not straightforward. From Fig. 6.3(b) and (c), it can be observed that the carriers in each layer do not reach their equilibrium values as the layer thickness is smaller than the space charge width in either side. The capacitance can be calculated as $|dQ/dV|$, where Q is the charge accumulated/depleted determined from the carrier slope in Fig. 6.3(b)-(c) and V is the voltage. For a small amount of charge accumulated/depleted, the interface capacitance can be ignored without any appreciable error.

The depletion capacitance can be calculated as [143]

$$C_d = C_{\|} + C_f + C_{CPS}^t + C_{CPS}^b \tag{6.5}$$

where, $C_{\|}$ is the parallel plate diode depletion capacitance, and, C_f and C_{CPS}^t (C_{CPS}^b) are the fringe capacitances due to charges in the center of the diode and due to widened depletion width at the top (bottom) oxide/semiconductor interface respectively. Since the depletion width of the different layers are different for a given voltage due to different material properties, $C_{\|}$ is calculated for each layer and added due to their parallel configuration which can be written as

$$C_{\|} = \epsilon_0 \sum_{1}^{layer} \frac{\epsilon_{layer} h_{layer}}{W_D^{layer}} \tag{6.6}$$

The calculation of C_f, C_{CPS}^t, and C_{CPS}^b is given in [143]. For the proposed structure, the average depletion width is given by

$$W_{D,av} = \epsilon_0 \epsilon_{av} \frac{H_{rib}}{C_{\|}} \tag{6.7}$$

where

$$\epsilon_{av} = \frac{\sum_{1}^{layer} h_{layer}\epsilon_{layer}}{\sum_{1}^{layer} h_{layer}} \tag{6.8}$$

Since carriers travel in different layers with different effective mass and energy, the bandwidth of the proposed phase shifter can be limited by the time taken by the carriers to arrive from the top layer to the bottom layer under an applied reverse bias. The carrier transit time from layer 7 to layer 1 can be calculated as [162]

$$\tau_e = \sum_{i=7}^{i=2}\left[\sqrt{\frac{2\pi m_{ce}^{*i} h_i^2}{kT}} \exp\left(\frac{\Delta E_{c_i} - q\vec{E}_i h_i}{kT}\right)\right] \tag{6.9a}$$

$$\tau_h = \sum_{i=7}^{i=2}\left[\sqrt{\frac{2\pi m_{ch}^{*i} h_i^2}{kT}} \exp\left(\frac{\Delta E_{v_i} - q\vec{E}_i h_i}{kT}\right)\right] \tag{6.9b}$$

$$\tau = \max(\tau_e, \tau_h) \tag{6.9c}$$

The band offset, and the electric field is positive if the band energy of the next layer is higher and the electric field aids in carrier transit, respectively. The 3 dB modulation bandwidth of the proposed phase shifter is calculated as [162]

$$f_{3dB} = \left(f_{\tau}^{-2} + f_{RC}^{-2}\right)^{-0.5} \tag{6.10}$$

where, f_{τ} and f_{RC} are the transit time limited and RC limited bandwidth given in [143, 162] as

$$f_{\tau} = \frac{0.55}{\tau} \tag{6.11a}$$

$$f_{RC} = \frac{1}{2\pi RC_d} \tag{6.11b}$$

6.2.5 Phase shifter metrics

The proposed PN optical phase shifter has been simulated in Sentaurus TCAD to obtain the 2D carrier concentration profiles at reverse bias voltages from 0 to 5 V with a P and N doping of 5×10^{17} cm^{-3} each. The 2D carrier profile across the rib area at -5 V is shown in Fig. 6.6(a). Boron and phosphorus have been used as the acceptor and donor, respectively. The P^{++} (N^{++}) contact regions have been doped with 1×10^{20} cm^{-3} Boron (Phosphorus). The junction is kept at the center of the rib waveguide, coinciding with the mode center. A total of 800 sample points across the rib area was selected for each reverse bias voltage to extract the electron and hole density profiles. Fig. 6.6(b)-(f) shows the performance metrics of the proposed optical phase shifter as a function of voltage along with a silicon and $Si_{0.7}Ge_{0.3}$ phase shifter of same doping and cross-section for comparison. It should, however, be noted that for the $Si_{0.7}Ge_{0.3}$ phase shifter, the thickness of the $Si_{0.7}Ge_{0.3}$ layer was kept 12.5 nm to keep the layer strained and prevent lattice defects [155].

The phase shift per unit length, $V_\pi L_\pi$, and $\alpha V_\pi L_\pi$ increase with reverse bias voltage, whereas the absorption loss per unit length and the insertion loss decreases. From Fig. 6.6, it can be ob-

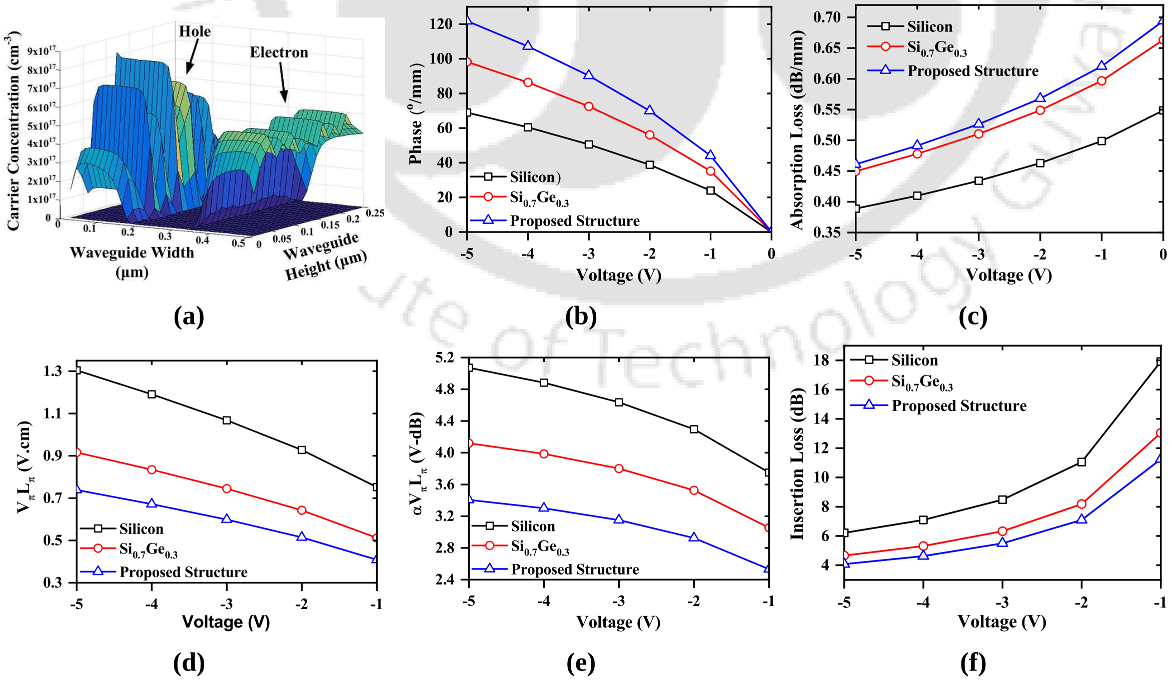

Fig. 6.6: (a) 2D carrier profile in the rib area at -5 V, (b) Phase shift per unit length, (c) Absorption loss per unit length, (d) $V_\pi L_\pi$ product, (e) $\alpha V_\pi L_\pi$ product, and (f) Insertion loss in dB.

served that the phase shift per unit length is higher, and the $V_\pi L_\pi$, $\alpha V_\pi L_\pi$, insertion loss is lower for the proposed structure compared to silicon and $\mathrm{Si_{0.7}Ge_{0.3}}$. The effective mass (mobility) of strained $\mathrm{Si_{1-x}Ge_x}$ layers decreases (increases) with mole fraction. However, the absorption loss has an inverse square dependency on effective mass and only inverse dependency on mobility, as seen from (6.1b) resulting in a higher absorption loss per unit length of the proposed structure compared to the silicon and $\mathrm{Si_{0.7}Ge_{0.3}}$ phase shifter. A more reasonable figure-of-merit is the $\alpha V_\pi L_\pi$, from which it can be seen that although the absorption per unit length is higher for the proposed phase shifter, the total absorption is lower due to lower L_π because of higher phase shift per unit length. A 1.77 (1.24) times higher phase shift, 0.57 (0.39) times lower $V_\pi L_\pi$, 0.67 (0.83) times lower $\alpha V_\pi L_\pi$, and 0.66 (0.87) times lower insertion loss have been obtained for the proposed optical phase shifter compared to the silicon ($\mathrm{Si_{0.7}Ge_{0.3}}$) phase shifter at -5 V.

The proposed phase shifter capacitance is shown in Fig. 6.7(a). The capacitance decreases with an increase in the reverse bias voltage as expected for a reverse-biased diode. The interface capacitance has been neglected as the error between the analytically calculated depletion capacitance and total device capacitance obtained from Sentaurus TCAD is less than 5%. The resistance at each reverse bias voltage has been calculated from (6.2) - (6.4) by using the extracted carrier concentration profiles. The 3 dB bandwidth of the phase shifter along with the RC and transit time-limited bandwidth is shown in Fig. 6.7(b). The RC limited bandwidth at -5 V is ~45 GHz. The hole (electron) transit time is 15.79 (4.05) ps. The $\hat{x}$-directed electric field obtained from TCAD is the same at all voltages as the applied bias essentially creates a $\hat{y}$-directed field. The transit time-limited bandwidth is thus constant at 34.83 GHz. The overall 3 dB bandwidth is ~27.5 GHz at -5 V. The bandwidth increases with reverse bias and can be further improved by higher doping so as to reduce the device resistance or by using smaller layer thickness to decrease the carrier transit time. The transit time of electrons is small mainly because of lower conduction band offset compared to the valence band due to the small difference in the electron affinity of silicon (4.05 eV) and germanium (4.00 eV). The hole transit from layer 7 to layer 1 is pictorially depicted in Fig. 6.7(c). The hole travel from layer 7 to 4 is from a higher energy level to lower one against the built-in junction electric field. The travel

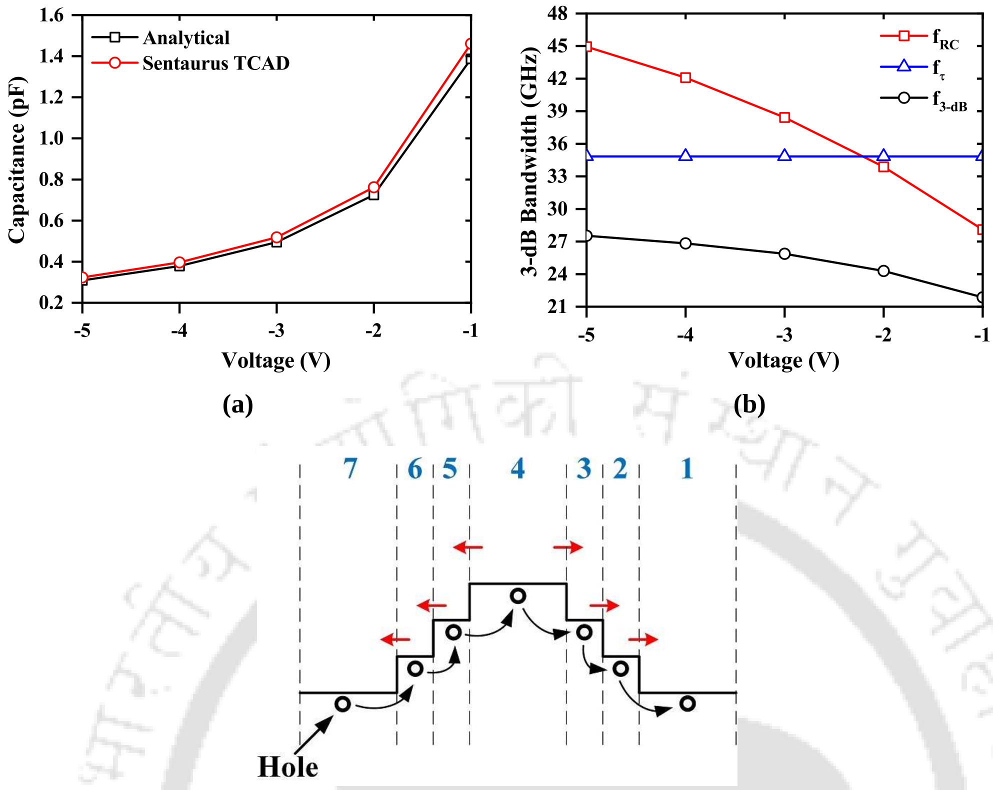

(a)

(b)

(c)

Fig. 6.7: (a) Total capacitance, (b) 3-dB modulation bandwidth, and (c) Transit of hole from layer 7 to layer 1; the layers are denoted at the top in blue and the red arrows represent the built-in electric field at the interfaces.

from layer 4 to 1 is aided by the built-in field, but the hole has to go from a lower energy level to a higher energy level. The transit of the electron is similar except the fact that in going from layer 7 to 1, the electron first has to travel to a higher energy level (layer 4) aided by the built-in junction electric field and then to a lower energy level (layer 1) against the field. Using a smaller value of mole fraction will decrease the total valence band offset but at the cost of lower phase shift and higher loss. Though the bandwidth is limited by the transit time, it is better compared to [91, 163–166].

Since the hole concentration difference causes a larger change in the refractive index compared to the corresponding electron concentration difference as evident from (6.1a), coinciding the mode center with the hole depletion region leads to a higher phase shift. The junction was shifted towards the N region, and the phase shifter performance at 5 V reverse bias was calculated and is shown in Fig. 6.8(a) and (b). The maximum phase shift occurs when the junction is shifted by 60 nm, where the maximum overlap of the P depletion region with the mode oc-

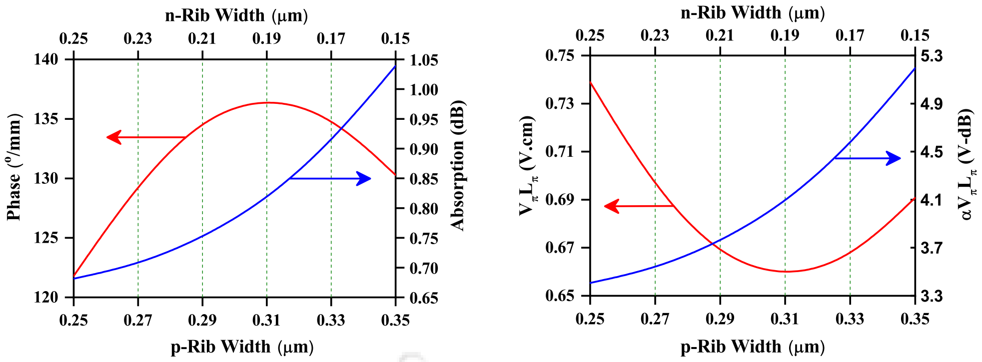

(a) **(b)**

Fig. 6.8: (a) Phase shift (left y-axis); Absorption loss (right y-axis) and (b) $V_\pi L_\pi$ (left y-axis); $\alpha V_\pi L_\pi$ (right y-axis). The lower and upper x-axis represents the P and N region rib width respectively.

curs. Higher phase shift leads to a lower L_π and thus lower $V_\pi L_\pi$. The phase shift increases to 137°/mm from 122°/mm, the $V_\pi L_\pi$ decreases to 0.66 V.cm from 0.74 V.cm. However, the absorption loss ($\alpha V_\pi L_\pi$) increases to 0.81 dB (4.07 V-dB) from 0.68 dB (3.41 V-dB). This is because the hole effective mass and mobility is lower than that of the electron. Since the junction shift towards N region results in a larger interaction of the mode with the P region, the absorption and thus $\alpha V_\pi L_\pi$ increases. Moving the junction towards the P region will result in lower absorption and $\alpha V_\pi L_\pi$ although at the expense of lower phase shift and higher $V_\pi L_\pi$.

6.3 Process simulation study

The fabrication of the proposed multi-layer SiGe phase shifter can be done using molecular beam epitaxy (MBE) [167] to grow thin layers of $Si_{1-x}Ge_x/Si_{1-y}Ge_y$ with varying germanium content followed by ion implantation to form the P and N regions. The complexity lies in the growth of the thin heterojunction layers. The effective control on concentration of dopant species, growth rate, and growth temperature can be the limiting factors that could result in variation of the phase shifter metrics. A more practical way to form the graded-index profile is to implant Ge on Si. This section focus on the process simulation study of a graded-index lateral and vertical PN phase shifter to emulate a fabricated device.

6.3.1 Ge implantation

The strained graded-SiGe phase shifter is created using Synopsys SPROCESS 2D [113]. An SOI wafer is used with 250 nm top Si <100> thickness. To form the graded-index structure, Ge

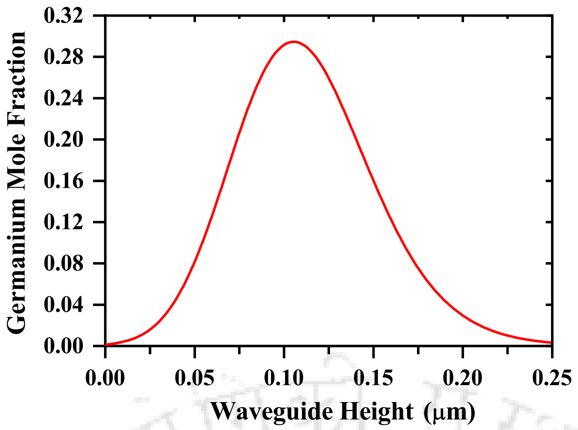

Fig. 6.9: Ge mole fraction.

with a dose of 1.35×10^{17} cm^{-2} is implanted at 165 keV energy. The resulting Ge mole fraction profile along the waveguide height is shown in Fig. 6.9.

6.3.2 Material parameters

Ge doping results in the formation of strain across the waveguide rib. The in-plane direction is denoted by $\|$, whereas the out-of-plane direction is denoted by $\perp$. The strain components can be calculated as [156]:

$$\epsilon_{\|}(x) = \frac{a_{\|}(x)}{a_0(x)} - 1 \tag{6.12a}$$

$$\epsilon_{\perp}(x) = \frac{a_{\perp}(x)}{a_0(x)} - 1 \tag{6.12b}$$

where $a_{\|} = a_0^{Si}$, and $a_{\perp}$ changes along the rib height. The material parameters of Si and Ge have been taken from [156, 168, 169] and are listed in Table 6.1. The lattice constant of relaxed $Si_{1-x}Ge_x$ is [161]

$$a_0^{SiGe}(x) = a_0^{Si} + 0.200326x(1-x) + (a_0^{Ge} - a_0^{Si})x^2 \tag{6.13}$$

The out-of-plane lattice constant as a function of the germanium mole fraction is given

Table 6.1: Material Parameters

Material	Lattice Constant	Elastic Constants			Spin-Orbit Splitting	Electron mass (/m$_0$)		Hole mass (/m$_0$)		
	a_0 (Å)	c_{11}	c_{12}	c_{44}	Δ_{so} (eV)	m_l^*	m_t^*	m_{hh}^*	m_{lh}^*	m_{so}^*
Si	5.43	1.675	0.650	0.801	0.044	0.92	0.197	0.48	0.16	0.24
Ge	5.65	1.315	0.494	0.684	0.29	1.64	0.082	0.28	0.044	0.08

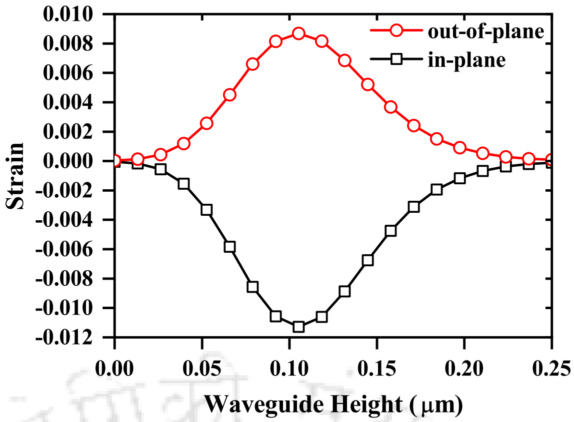

Fig. 6.10: In-plane and out-of-plane strain.

as [156]:

$$a_{\perp}(x) = a(x)\left[1 - 2\frac{c_{12}(x)}{c_{11}(x)}\epsilon_{\|}(x)\right] \tag{6.14}$$

In calculating $a_{\perp}$, linear interpolation of c_{11} and c_{12} given in Table 6.1 have been used. The in-plane and out-of-plane strain along the waveguide height is shown in Fig. 6.10 which shows that strain is in-plane biaxial compressive.

The biaxial compressive strain causes tetragonal lattice distortion, which causes the in-plane components (ϵ_{yy} and ϵ_{zz}) to be negative and the out-of-plane component (ϵ_{xx}) to be positive [168]. The off-diagonal components are zero. The tetragonal strain is given as

$$\epsilon_T = \epsilon_{\perp} - \epsilon_{\|} \tag{6.15}$$

The strain tensor is

$$\epsilon = \begin{bmatrix} \epsilon_{\|} & 0 & 0 \\ 0 & \epsilon_{\|} & 0 \\ 0 & 0 & \epsilon_{\perp} \end{bmatrix} \tag{6.16}$$

The conduction band of $Si_{1-x}Ge_x$ for 0 ≤ x ≤ 0.75 remains Si-like [168]. The shape of the constant energy surfaces does not change. However, the 6-fold degenerate band splits into a 4-fold (Δ_4) and a 2-fold (Δ_2) band. The Δ_4 band shift downwards in energy and the Δ_2 band shift upwards [170]. This results in a higher electron population in the Δ_4 band compared to the

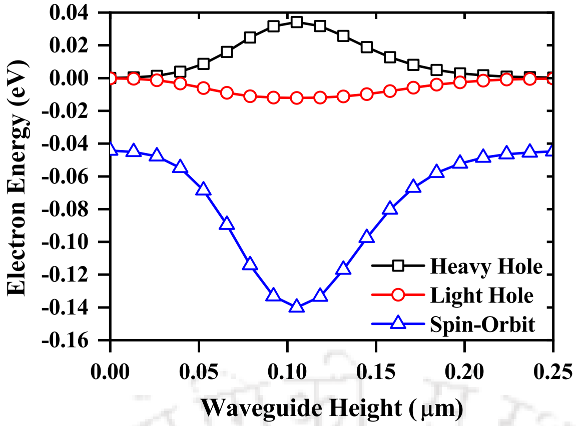

Fig. 6.11: Valence band energy.

Δ_2 band and causes the lobe size to increase. The lower electron-electron scattering between the Δ_2 band and the Δ_4 band results in a smaller effective electron mass.

The effect of the strain on the valence band is to break the heavy- light-hole degeneracy and cause shift in energy of the spin-orbit band [168]. The valence band energies along the waveguide height is shown in Fig. 6.11 from which it can be observed that strain causes the heavy-hole band to move down in energy while the light-hole and spin-orbit band move upwards. It should be kept in mind that the hole energy is the opposite of electron energy and increases downwards. The valence band energies are calculated using [168]:

$$E_{hh}(x) = \bar{\epsilon}(x) \tag{6.17a}$$

$$E_{lh}(x) = -\frac{1}{2}\left[\bar{\epsilon}(x) + \Delta_{so}(x)\right] + \frac{1}{2}\sqrt{9\bar{\epsilon}^2(x) + \Delta_{so}^2 - 2\bar{\epsilon}(x)\Delta_{so}} \tag{6.17b}$$

$$E_{so}(x) = -\frac{1}{2}\left[\bar{\epsilon}(x) + \Delta_{so}(x)\right] - \frac{1}{2}\sqrt{9\bar{\epsilon}^2(x) + \Delta_{so}^2 - 2\bar{\epsilon}(x)\Delta_{so}} \tag{6.17c}$$

where, $\Delta_{so}(x)$ is calculated by linearly interpolating the values for Si and Ge listed in Table 6.1 and $\bar{\epsilon}(x)$ is the strain energy given in [168].

The effective mass components of electrons and holes can be calculated as [171]:

$$\frac{1}{m_j^{*SiGe}} = \frac{1-x}{m_j^{*Si}} + \frac{x}{m_j^{*Ge}} \tag{6.18a}$$

where, j refers to longitudinal (l), transverse (t), heavy-hole (hh), light-hole (lh), and spin-orbit (so) components given in Table 6.1. The density-of-state (DOS) and conductivity effective

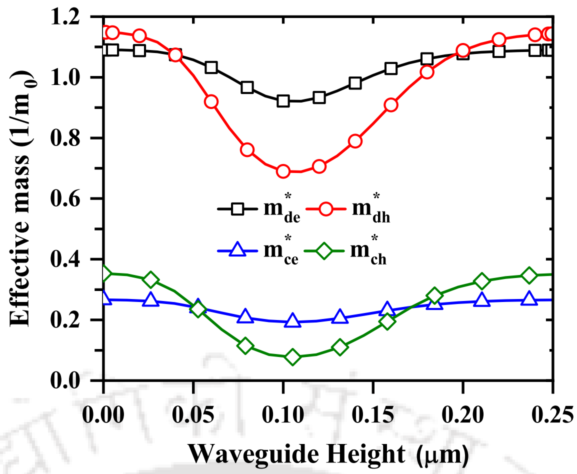

Fig. 6.12: DOS and conductivity effective mass of electrons and holes.

mass of electrons and holes are calculated as [169]

$$m^*_{de} = 6^{2/3}\left[m_t^{*^2} m_l^*\right]^{1/3} \tag{5a}$$

$$m^*_{ce} = 3\left(\frac{2}{m_t^*} + \frac{1}{m_l^*}\right)^{-1} \tag{5b}$$

$$m^*_{dh} = \left[\left(m^*_{hh} e^{\frac{-E_{hh}}{kT}}\right)^{3/2} + \left(m^*_{lh} e^{\frac{-E_{lh}}{kT}}\right)^{3/2} + \left(m^*_{so} e^{\frac{-E_{so}}{kT}}\right)^{3/2}\right]^{2/3} \tag{5c}$$

$$m^*_{ch} = \frac{(m^*_{hh} e^{\frac{-E_{hh}}{kT}})^{3/2} + (m^*_{lh} e^{\frac{-E_{lh}}{kT}})^{3/2} + (m^*_{so} e^{\frac{-E_{so}}{kT}})^{3/2}}{(m^*_{hh} e^{\frac{-E_{hh}}{kT}})^{1/2} + (m^*_{lh} e^{\frac{-E_{lh}}{kT}})^{1/2} + (m^*_{so} e^{\frac{-E_{so}}{kT}})^{1/2}} \tag{5d}$$

where subscripts *de*, *dh*, *ce*, and *ch* represent the effective masses of DOS electron, DOS hole, conductivity electron, and conductivity hole, respectively. The DOS and conductivity effective mass of electrons and holes along the waveguide height is shown in Fig. 6.12.

The electron and hole mobility is calculated from [170, 172, 173].

6.3.3 Lateral PN phase shifter

To form the PN junction, boron and phosphorus have been used for implantation. Since the implanted species have a Gaussian distribution, three-step implantation followed by rapid thermal annealing (RTA) at 1100°C for 5 seconds was done to ensure uniform concentration across the waveguide height. The species dose and implantation energy of each step for boron and phosphorus are shown in Table 6.2 and Table 6.3, respectively. The corresponding doping profile after each implantation step for boron and phosphorus can be seen in Fig. 6.13(a) and

Table 6.2: Dose and energy of boron implantation

Step	Dose (cm^{-2})	Energy (keV)
I	1×10^{13}	20
II	2×10^{12}	10
III	2×10^{12}	3

Table 6.3: Dose and energy of phosphorus implantation

Step	Dose (cm^{-2})	Energy (keV)
I	2×10^{13}	85
II	5×10^{12}	25
III	1×10^{12}	02

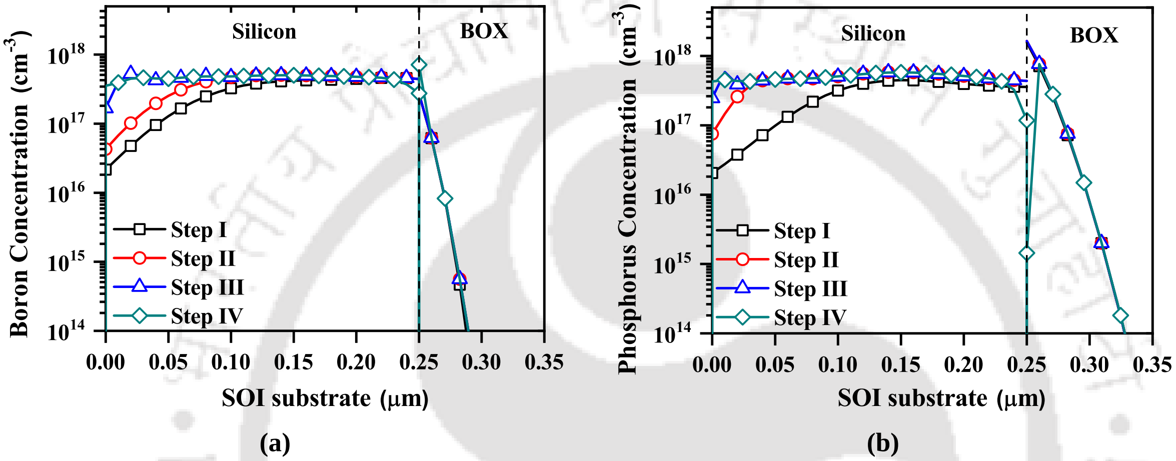

Fig. 6.13: Implanted distribution of (a) Boron and (b) Phosphorus.

(b), respectively, where RTA is depicted as step IV. To form a 500 nm × 250 nm rib waveguide with 50 nm slab thickness, a 200 nm anisotropic etch is done. The 50 nm thick P^{++} (N^{++}) end contacts are formed by implanting boron (phosphorus) with a dose of 1×10^{15} (1×10^{15}) cm^{-2} at an energy of 3 (20) keV. This is followed by 500 nm top oxide deposition and 500 nm anisotropic oxide etch over the P^{++} and N^{++} contacts for metal deposition.

6.3.3.1 Phase shifter metrics

The rib waveguide supports only fundamental quasi-TE mode with mode confinement of 73.8%. The quasi-TM mode has confinement of 31.2% and is cut-off. The scattering and FCA losses are calculated to be 2.15 dB/cm and 4.13 dB/cm, respectively. The performance metrics of the graded $Si_{1-x}Ge_x$ phase shifter as a function of the reverse bias voltage is shown in Fig. 6.14(a)-(c) along with a Si phase shifter for comparison, simulated using the same process flow without the Ge implantation. The phase shift per unit length, $V_\pi L_\pi$, and $\alpha V_\pi L_\pi$ increase with reverse voltage, whereas, the absorption loss per unit length and insertion loss decrease. The

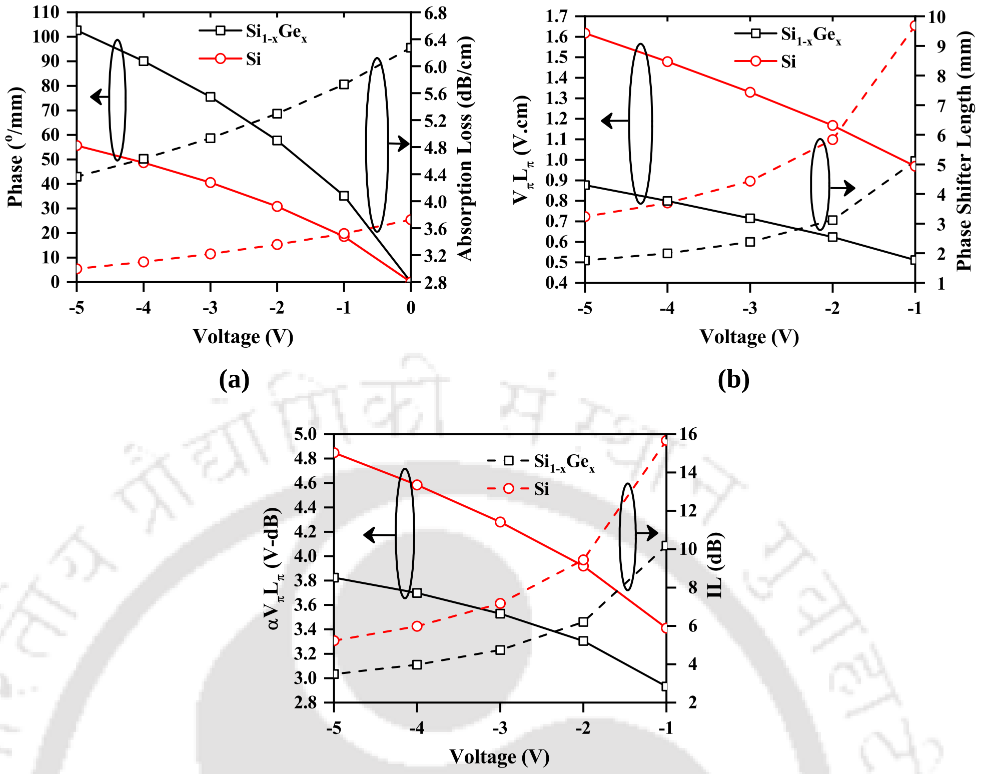

(a) (b)

(c)

Fig. 6.14: (a) Phase shift and absorption loss per unit length, (b) $V_\pi L_\pi$ product and phase shifter length, and (c) $\alpha V_\pi L_\pi$ product and insertion loss.

increase in phase shift with voltage is non-linear, and a larger phase shift corresponds to a smaller phase shifter length required for π phase shift. The absorption loss per unit length of $Si_{1-x}Ge_x$ phase shifter is higher compared to Si, as seen from Fig. 6.14(a). This is because of the inverse square dependency on the effective masses. Although the absorption loss per unit length is higher for the $Si_{1-x}Ge_x$ phase shifter, the total absorption loss at any voltage is lower than Si, as evident from Fig. 6.14(c) due to the lower phase shifter length required. The insertion loss of the $Si_{1-x}Ge_x$ phase shifter is also lower than its Si counterpart. Higher mole fraction can be obtained by increasing the Ge implantation dose, which will result in a larger phase shift and lower $V_\pi L_\pi$ although at the expense of higher absorption as the intrinsic material absorption will set in. Higher doping also leads to a larger phase shift and smaller $V_\pi L_\pi$ but at the cost of higher FCA. The junction of the designed phase shifter is kept in the center of the rib waveguide coinciding with the mode maxima. Shifting the junction to the right such that the mode maxima overlaps with the P-depletion region will lead to a higher phase shift as holes cause a larger change in the refractive index than electrons. The graded-layer formation leads to larger mode overlap with the strained $Si_{1-x}Ge_x$ region and ensures that the material remains strained. For a $Si_{1-x}Ge_x/Si$, the critical layer thickness decreases with increasing Ge mole fraction, where the critical layer thickness is defined as the thickness below which the material is strained and without any defects [155]. The graded layer results in a gradual increase of the mole fraction as opposed to a step increase, thereby keeping the layer strained.

6.3.4 Vertical junction phase shifter

The cross-section of the proposed vertical junction PN phase shifter is shown in Fig. 6.15. The graded-index formation is the same as described in section 6.3.2. The formation of the vertical junction structure requires multiple etching and deposition steps and is complex compared to a lateral junction structure. Boron (phosphorus) has been used to form the P (N) rib, P+ (N+) slab, and the P++ (N++) contact region. The implantation dosages and energies used to create the doping regions are given in Table 6.4. For defect annihilation, RTA was done at 1100°C for 5 seconds. Before contact formation, 500 nm oxide deposition was done, which will act as the top cladding. The doping concentration across the waveguide height is shown in Fig. 6.16. The mode profile of the designed phase shifter at 1550 nm is shown in Fig. 6.17. The quasi-TE mode (E^y) has mode confinement of 73.84%, and the quasi-TM mode (E^x) is cut-off with mode

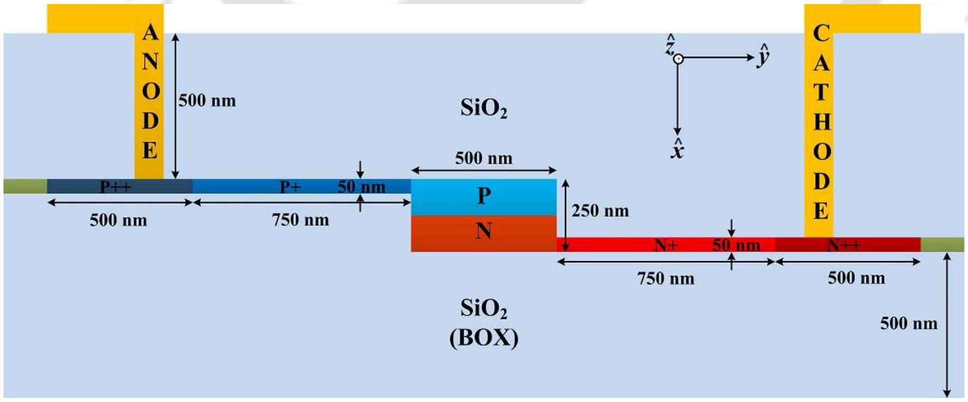

Fig. 6.15: Cross-section of the vertical junction phase shifter (the silicon substrate is not shown).

Table 6.4: Implantation dose and energy

Region	P	N	P+	N+	P++	N++
Dose (cm^{-2})	1×10^{13}	1×10^{13}	5×10^{13}	5×10^{13}	1×10^{15}	1×10^{15}
Energy (keV)	13	70	03	20	03	20

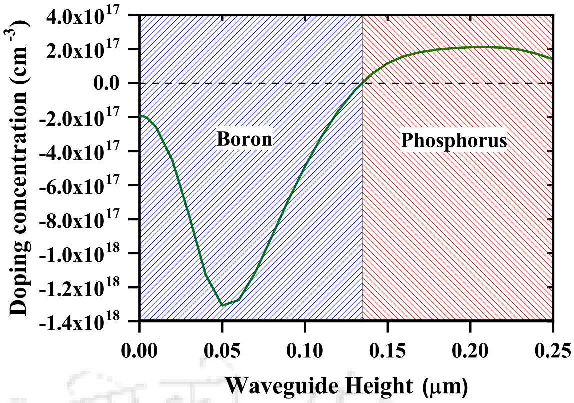

Fig. 6.16: PN doping profile.

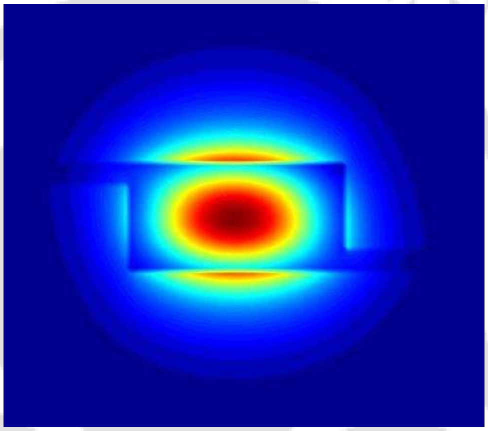

Fig. 6.17: Mode profile.

confinement of 31.19%.

The free carrier absorption loss of the designed phase shifter is calculated to be 7.33 dB/cm.

6.3.4.1 Phase shifter metrics

The phase shifter is simulated in Synopsys® SDEVICE, and the 2D carrier distribution across the waveguide rib for different reverse bias voltages have been extracted to calculate the phase shifter performance metrics. The phase shift and absorption loss per unit length are shown in Fig. 6.18(a) and (b) respectively. The phase shift and absorption loss curve are non-linear with voltage, which affects the modulator transfer function at higher drive voltages. For comparison, a silicon phase shifter has been simulated with the same waveguide structure, dimension, doping profile, and process flow, but without the germanium implantation. More than 3× increase in phase shift per mm at -5 V can be observed from Fig. 6.18(a) for germanium doped silicon phase shifter compared to silicon. The absorption loss per unit length, however, is

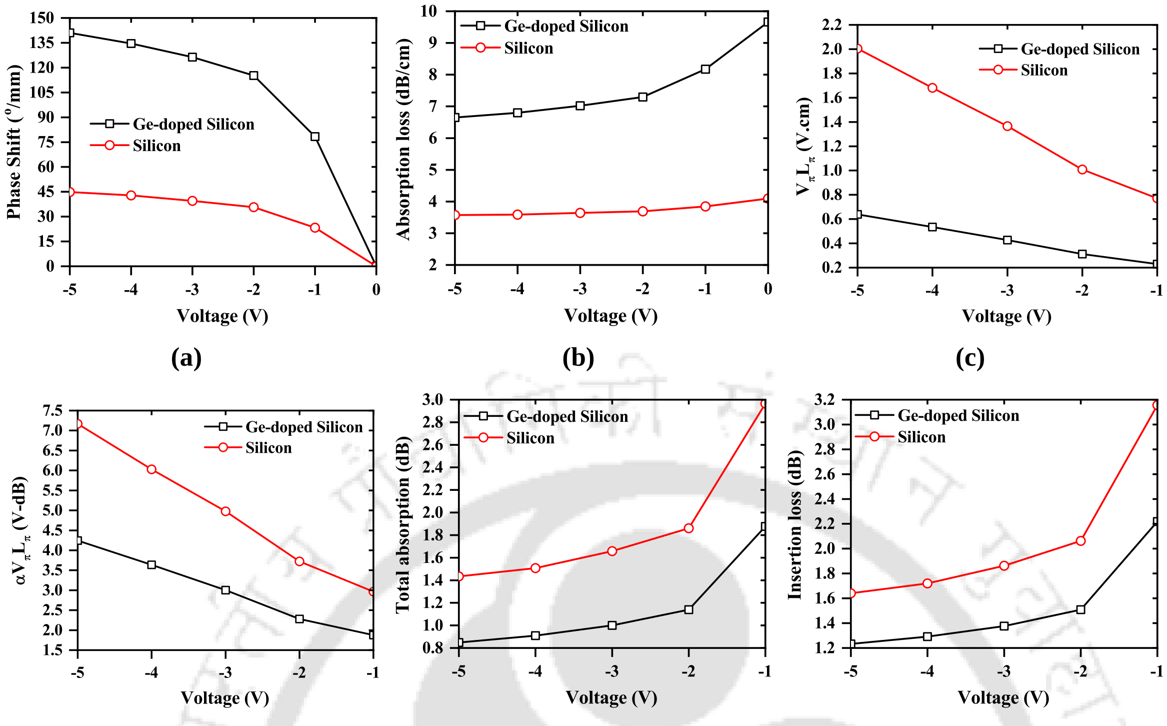

(a) **(b)** **(c)**

(d) **(e)** **(f)**

Fig. 6.18: (a) Phase shift per unit length, (b) Absorption loss per unit length, (c) $V_{\pi}L_{\pi}$, (d) $\alpha V_{\pi}L_{\pi}$, (e)Total absorption, and (f) Insertion loss.

much greater than silicon. A vertical junction results in carrier change with applied bias over a greater length (waveguide width) compared to a lateral junction, where carrier change is over the waveguide height. The E^y mode maxima and the germanium concentration maxima coincide with the P depletion region. Also, the P doping concentration is larger than the corresponding N concentration. This results in the larger phase shift of the proposed device since holes cause a better phase shift than electrons. Also, the hole conductivity mass is lower than the electron, which results in a larger absorption loss per unit length. The junction region can be modeled as a graded-junction, as evident from Fig. 6.16. This limits the FCA loss due to fewer carriers near the junction. Fig. 6.18(c) and (d) shows the $V_{\pi}L_{\pi}$ and $\alpha V_{\pi}L_{\pi}$ which increases with an increase in the reverse bias voltage. The total absorption and insertion loss are shown in Fig. 6.18(e) and (f) respectively. Though the absorption loss per unit length is greater for germanium doped phase shifter compared to silicon, the total absorption and the insertion loss are lower due to the higher phase shift of the former, which corresponds to a lesser required length to achieve π phase shift. Also, the absorption is mainly due to holes as the N rib is fully depleted at higher

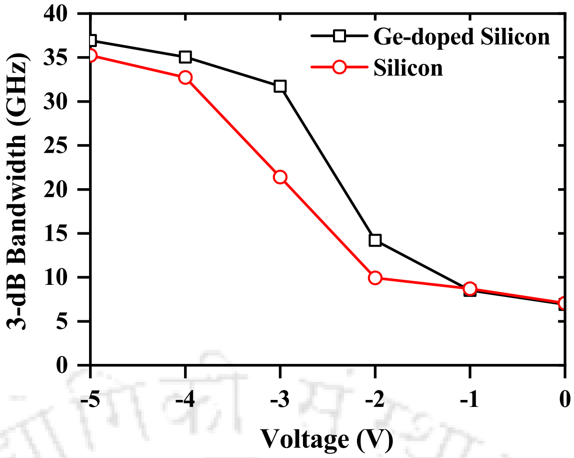

Fig. 6.19: 3 dB bandwidth.

reverse voltages.

The 3 dB bandwidth is shown in Fig. 6.19. The bandwidth of the germanium doped phase shifter is greater than silicon, although slightly. The largest bandwidth difference is 11 GHz at -3 V. The bandwidth has been calculated from the admittance matrix obtained from the small-signal analysis of the phase shifter using Synopsys® SDEVICE. The frequency normalized susceptance has been used to calculate the bandwidth [143]. The bandwidth of germanium doped phase shifter is larger because of lower resistance due to higher mobility of $Si_{1-x}Ge_x$ compared to silicon.

Multiple factors result in better performance of the germanium doped silicon phase shifter compared to silicon, though both have the same waveguide structure, dimension, and doping profile. These factors are directly related to material properties of $Si_{1-x}Ge_x$. The phase shift per unit length is directly proportional to the carrier concentration and inversely proportional to the refractive index and the carrier effective masses, as evident from (6.1). The phase shift also depends on the modal overlap with the depletion region, and thus the mode confinement plays an important role. The fundamental quasi-TE mode confinement of the germanium doped phase shifter is 73.84%, and that of silicon is 73.15%. The improvement in performance due to confinement is thus negligible. The main contribution comes due to the lower carrier effective masses of strained $Si_{1-x}Ge_x$. The effective masses decrease with an increase in the germanium concentration, as can be seen from Fig. 6.12. For a germanium mole fraction of 0.3, the electron effective mass decrease by a factor of 1.38 and hole by 4.55. The localized DOS changes across the rib height due to the introduction of germanium and results in carrier redistribution. The hole carrier density is more for larger germanium concentrations.

The performance of the proposed vertical junction germanium doped silicon phase shifter can be further improved by various parameter optimizations, including waveguide dimensions, dopant species concentration, doping profile shape, junction placement, etc. Larger waveguide dimensions will result in greater mode confinement and higher phase shift, although at the cost of higher absorption loss. Increasing the germanium implantation dose will result in a larger phase shift but at the cost of higher material absorption. Higher doping densities will result in larger phase shift but again at the cost of larger FCA loss. The bandwidth can be increased by using higher P and N doping, reducing the slab cross-sectional length, etc. Thus, multiple trade-offs are present and careful optimization, and design among all the parameters are required to enhance the device performance.

6.4 Comparison

The comparison of the multi-layer SiGe phase shifter, process simulated lateral SiGe phase shifter, and process simulated vertical SiGe phase shifter with recently reported PN optical phase shifters are given in Table 6.5.

Table 6.5: Comparison of different phase shifters

Ref	Material	Device	Junction	W_{rib} (nm)	H_{rib} (nm)	H_{slab} (nm)	L (mm)	$V_{\pi}L_{\pi}$ (V.cm)	*IL* (dB)	f_{3dB} (GHz)
[174]*	Silicon	PN	Lateral	500	220	90	0.5	0.72	4.7	13.3
[86]*	Silicon	PN	Lateral	400	220	100	1	1.9	4	-
[119]*	Silicon	PN	Lateral	400	300	50	1	1.15	3.6	18
[91]*	Silicon	PN	U-shaped	700	150	65	5.2	2.6	-	13.5
[175]*	Silicon	PIN	Lateral	480	220	90	0.95	0.19	2.25	20
[176]**	Silicon	MIS	Vertical	500	220	50	0.775	0.278	3.2	22.2
[177]*	$^{\#}$SISLG	Capacitor	-	480	220	60	0.3	0.28	7.08	5
[178]*	p-$Si_{0.6}Ge_{0.4}$/Si	PN	Lateral	400	220	-	0.5	0.81	2	12
Authors'**	$^{\#\#}Si_{1-x}Ge_{x}$	PN	Lateral	500	250	50	1.48	2.5	4	27.5
Authors'**	Ge doped Silicon	PN	Lateral	500	250	50	1.75	0.87	3.49	-
Authors'**	Ge doped Silicon	PN	Vertical	500	250	50	2.3	0.23	2.22	37

* Experimental result; ** Simulation result.

$^{\#}$ Silicon-insulator-SLG, SLG = Single Layer Graphene; $^{\#\#}$Multi-layer.

6.5 Summary

A strained SiGe PN optical phase shifter has been designed and analyzed with a graded-index structure having multiple strained layers of different mole fractions. The proposed structure has the advantage of having a thicker strained layer of higher mole fraction due to the graded structure, which results in greater overlap with the mode and thus greater change in refractive index. A phase shift of 122°/mm, $V_\pi L_\pi$ of 0.74 V.cm, $\alpha V_\pi L_\pi$ of 3.4 V-dB and insertion loss of 4 dB was obtained along with a 3-dB modulation bandwidth of 27.5 GHz at -5 V and a doping of 5×10^{17} cm^{-3}. A 15°/mm increase in phase shift and 0.08 V.cm decrease in $V_\pi L_\pi$ with only 0.13 dB increase in the total absorption loss was observed when the junction was moved by 60 nm towards the N region. A process simulation study has been done to form the graded-index profile by Ge implantation. Both lateral and vertical junction PN phase shifters have been process simulated. For the Ge-doped lateral PN phase shifter, 1.84× higher phase shift, 1.27× lower absorption loss, and 1.50× lower insertion loss have been observed compared to silicon. For the Ge-doped vertical PN phase shifter, phase shift of ~141°/mm, $V_\pi L_\pi$ of ~0.64 V.cm, insertion loss of ~1.23 dB, and 3-dB bandwidth of ~37 GHz has been obtained at -5 V.

7

Silicon Optical Modulator: SiGe MZM High-Speed Characteristics

Contents

7.1 Introduction

In the previous chapter, a multi-layer silicon-germanium (SiGe) phase shifter has been shown to exhibit enhanced free-carrier plasma dispersion (FCPD) effect compared to silicon (Si) phase shifter. The proposed graded-index SiGe phase shifter can also be created by implanting Ge in Si. This chapter presents the high-speed characteristics of the graded-SiGe Mach-Zehnder modulator (MZM) and is shown to have better performance compared to a Si MZM.

7.2 Phase shifter structure

The phase shifter cross-section is shown in Fig. 7.1. The PN phase shifter is process simulated using Silvaco® Athena. The waveguide parameters are given in Table 7.1. The graded-index profile is created using the same process steps, as described in section 6.3.2. However, the Ge dose and energy used are 1.7×10^{17} cm^{-2} and 220 keV, respectively. The Ge concentration along the waveguide height is shown in Fig. 7.2. The implantation energy has been so chosen to have maximum Ge concentration in the middle of the waveguide where the mode maxima occurs. The Ge implantation dose leads to a maximum mole fraction of 0.313 and is kept so as to avoid material absorption at C-band operation. The PN junction is formed by single implantation of each boron and phosphorus. Since an implantation profile is Gaussian-like, the implantation energy is chosen to ensure that the peak is in the middle of the waveguide. The

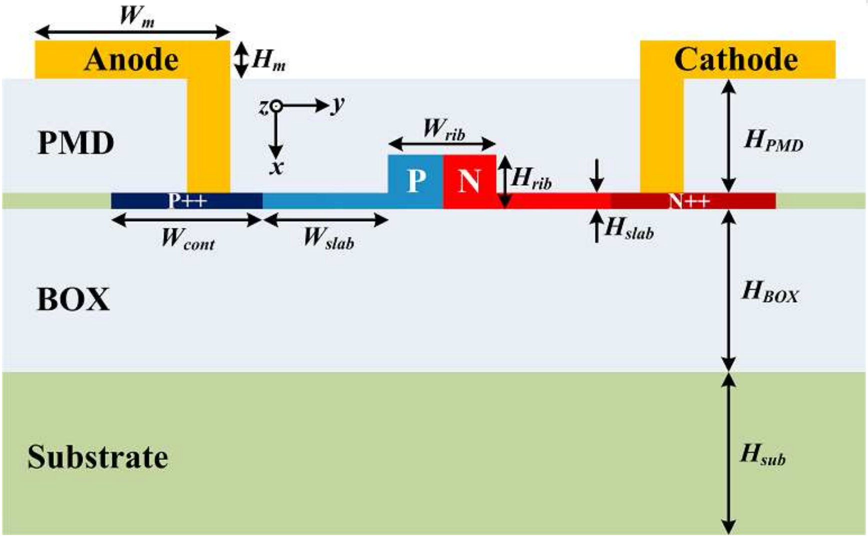

Fig. 7.1: Cross-section view of the PN phase shifter (the figure is not to scale).

Table 7.1: Waveguide parameters

Description	Symbol	Value
Metal contact width	W_m	3.2 μm
Metal layer thickness	H_m	0.8 μm
PMD layer thickness	H_{PMD}	0.6 μm
P++/N++ contact width	W_{cont}	0.5 μm
P/N slasec: 6.3.1b width	W_{slab}	0.5 μm
Rib width	W_{rib}	0.50 μm
Rib height	H_{rib}	0.25 μm
Slab height	H_{slab}	0.05 μm
BOX layer thickness	H_{BOX}	2 μm
Silicon substrate thickness	H_{sub}	500 μm

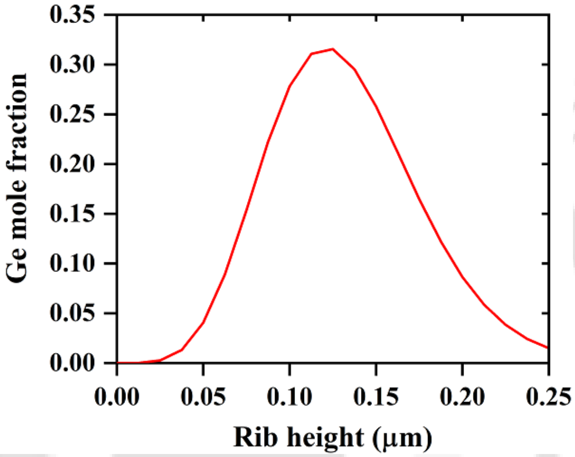

Fig. 7.2: Ge mole fraction across rib height.

boron (phosphorus) implantation dose and energy to form the P (N) region is 2.0 × 10^{13} (2.0 × 10^{13}) cm^{-2} and 25 (70) keV. The boron (phosphorus) implantation dose and energy to form the P++ (N++) region are 1.0 × 10^{15} (1.0 × 10^{15}) cm^{-2} and 3 (20) keV respectively. Each of the implantation steps is followed by a rapid thermal annealing (RTA) step at 1100°C for 5 seconds to recrystallize the structure and annihilate any defects. All other steps are similar to what is described in section 6.3.3. For comparison, a silicon PN phase shifter is also process simulated with the same steps described above, excluding the germanium implantation step. The stress-strain analysis and calculation of different material parameters can be found in section 6.3.2.

7.3 Phase shifter metrics

The process simulated PN phase shifter is analyzed using SILVACO® Atlas. The change in refractive index and absorption coefficient with the change in carrier concentration is deter-

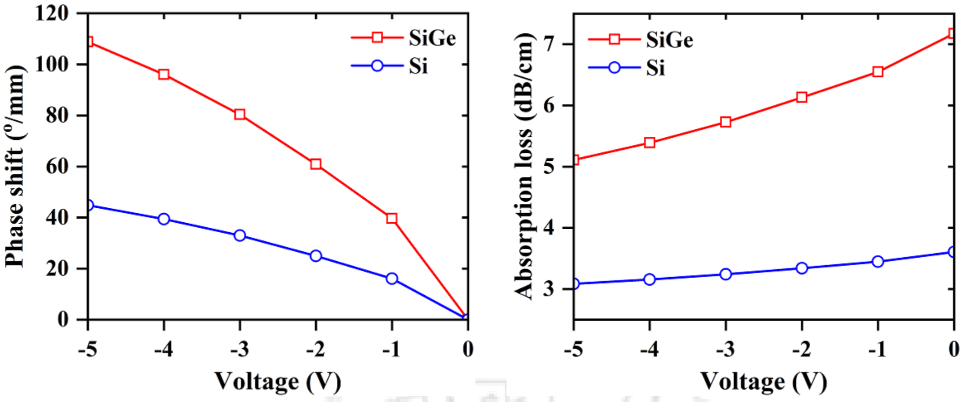

(a) (b)

Fig. 7.3: (a) Phase shift per unit length and (b) absorption loss per unit length.

mined from (6.1). The phase shift and absorption loss per unit length are shown in Fig. 7.3 for SiGe and Si phase shifter. The SiGe phase shifter has a larger phase shift per unit length compared to Si. This is due to the lower carrier effective mass of SiGe. The phase shift per unit length of SiGe (Si) is 108° (45°) at -5 V. The absorption loss consists of the free-carrier loss due to doping and the sidewall scattering loss. The scattering loss is calculated using the Payne-Lacey model and is 2.54 dB/cm (2.52 dB/cm) for SiGe (Si) phase shifter. There is a negligible difference in the scattering loss of the two phase shifters since the mode confinement of the two is comparable. The free-carrier loss at 0 V is 4.64 dB/cm (1.09 dB/cm) for SiGe (Si) phase shifter. The larger phase shift per unit length of the SiGe phase shifter results in better modulation efficiency ($V_\pi L_\pi$). The $V_\pi L_\pi$ of the SiGe (Si) phase shifter is 0.83 V.cm (2.01 V.cm) at -5 V. Although the absorption loss per unit length of the SiGe phase shifter is larger than the Si phase shifter, the total absorption is lower due to smaller L_π. The phase shifter is integrated into both arms of an MZM, and dual-arm drive is analyzed for both SiGe and Si phase shifters. V_π is chosen to be -5 V. The phase shifter length for SiGe and Si MZM is 0.8 mm and 2.0 mm, respectively. For dual arm drive, push-pull at quadrature operation is used, and thus the phase shifter length is kept half of that required for the single-arm drive. The small-signal analysis is done using TCAD, and the frequency normalized admittance matrix is extracted. The depletion capacitance of SiGe and Si phase shifter is shown in Fig. 7.4. The depletion capacitance per unit length of the SiGe phase shifter is found to be greater than the Si phase shifter. However, due to the lower L_π of SiGe phase shifter, the total capacitance of both phase shifters are similar.

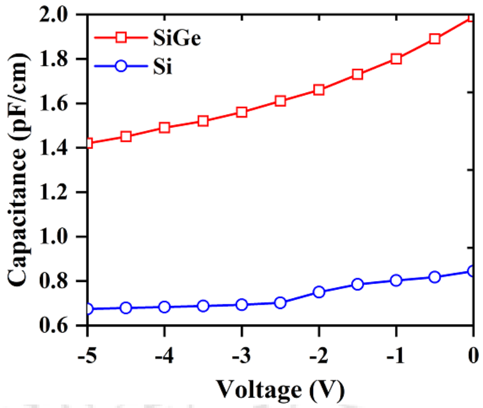

Fig. 7.4: Phase shifter capacitance as a function of applied voltage.

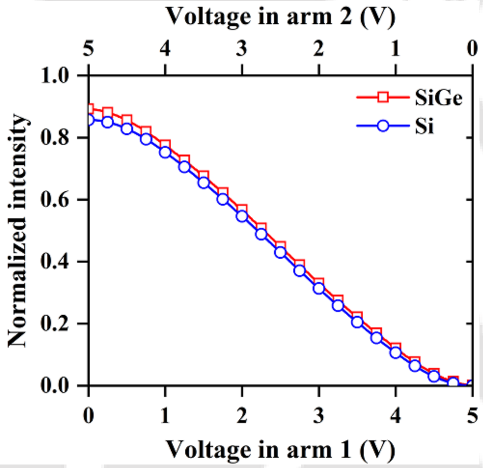

Fig. 7.5: Transfer characteristics of SiGe and Si MZM.

The capacitance at -5 V for the SiGe and Si phase shifter is 0.11 pF and 0.13 pF.

7.4 MZM transfer characteristics

The phase shifter bias point is chosen from the MZM transfer characteristics, which gives the ratio of output to input light intensity. The normalized output intensity is shown in Fig. 7.5 for the SiGe and Si MZM. The MZMs are driven in the linear region of the transfer characteristic plot, and the bias point is selected as 2 V. Both MZMs are driven by 2 V_{pp} drive voltage. In both MZMs, a TO phase shifter is kept in series with the EO PN phase shifter in one of the arms and tuned to quadrature operation. The DC extinction ratio of the SiGe (Si) MZM is 3.73 dB (3.81 dB). The insertion loss of SiGe (Si) MZM is 2.14 dB (2.44 dB), which includes 1 dB loss of the input 3-dB splitter and output combiner.

7.5 TWE analysis

The TWE characteristics of the SiGe and Si MZMs are shown in Fig. 7.6. The EO S_{21} curve is shown in Fig. 7.6(a). The 3 dB modulation bandwidth of SiGe (Si) MZM is 77.48 GHz (59.96 GHz). The higher modulation bandwidth of the SiGe MZM can be attributed to its lower length. The EE S-parameters are shown in Fig. 7.6(b). EE S_{11} represents the back reflection, and EE S_{21} gives an indication of the signal transmission loss [151]. The EE S_{11} is below -15 dB for the SiGe MZM over the whole simulated range. The EE S_{11} of the Si MZM is greater compared to the SiGe MZM till 16 GHz, indicating higher back reflection, after which it improves and falls below that of the SiGe EE S_{11}. The -6.4 dB EE S_{21} gives the 3 dB modulation bandwidth when there is no velocity mismatch [152]. The -6.4 dB EE bandwidth of the SiGe (Si) MZM is 58.16 GHz (85.99 GHz). The -6.4 dB EE bandwidth of the SiGe (Si) MZM is lower (higher) than the -3 dB EO bandwidth. The TWE attenuation per unit length (α_{TWE}) of both MZMs are shown in Fig. 7.6(c). The SiGe MZM has higher attenuation than the Si MZM. At the -3 dB

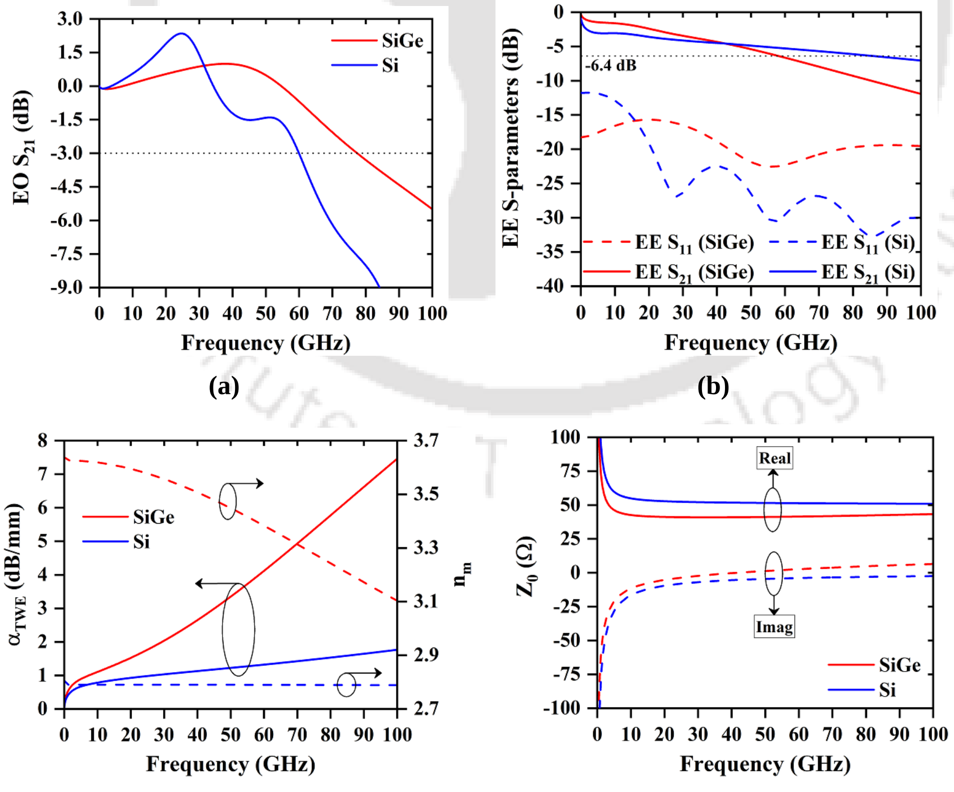

(a) (b)

(c) (d)

Fig. 7.6: (a) EO S_{21}, (b) EE S_{11} and EE S_{21}, (c) α_{TWE} and n_m, and (d) Z_0.

EO bandwidth, α_{TWE} is 4.45 dB (2.64 dB) for the SiGe (Si) MZM. The lower transmission loss of the Si MZM leads to the higher EE bandwidth compared to SiGe MZM. The optical group index of SiGe and Si MZM is 4.07 and 4.02, respectively. The microwave index (n_m) is shown in Fig. 7.6(c) from which it can be seen that the mismatch is more in the case of Si compared to SiGe. The characteristic impedance (Z_0) of both MZMs are shown in Fig. 7.6(d). At the -3 dB EO bandwidth, Z_0 of SiGe (Si) MZM is 42.18 + 4.52i (51.36 - 3.91i). The impedance matching is better in the case of Si MZM compared to SiGe MZM and results in lower back reflection, as seen from Fig. 7.6(b). Though the signal transmission loss is less and the impedance matching is better, the 3 dB modulation bandwidth of the Si MZM is lower than the SiGe MZM due to its longer length and higher velocity mismatch. At the -3 dB EO bandwidth, the characteristic impedance is inductive for the SiGe MZM and capacitive for the Si MZM.

7.6 High-speed characteristics

The high-speed characteristics are evaluated using OptiSystem® v.16.1.0. A 1550 nm laser of 10 dBm output power is used as the input to the MZM. The MZM is driven by a pseudo-random bit sequence (PRBS) of length 2^{15}-1 and a non-return-to-zero (NRZ) modulation scheme. The output of the MZM is connected to a single-mode fiber (SMF) with zero-dispersion at 1550 nm and 0.2 dB/km attenuation. The detector is a PIN diode with 1 A/W responsivity. The bit-error-rate (BER) is defined as the ratio of error bits to the total bits received. The BER as a function of SMF length for different modulation speeds is shown in Fig.

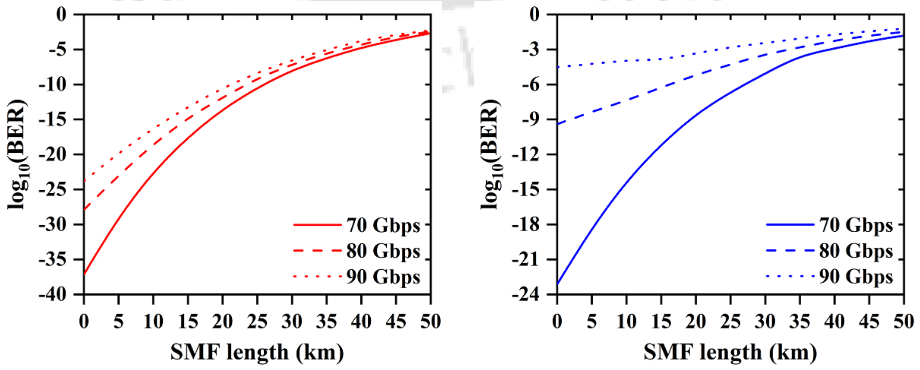

(a) (b)

Fig. 7.7: BER as a function of SMF length for (a) SiGe MZM and (b) Si MZM.

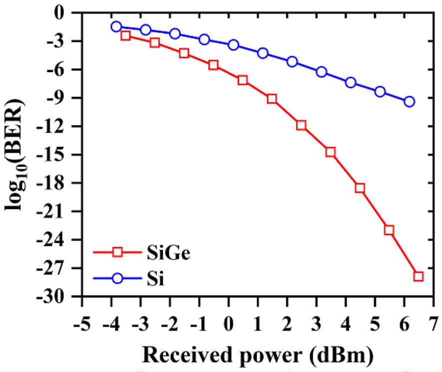

Fig. 7.8: BER as a function of the received power at 80 Gbps operation.

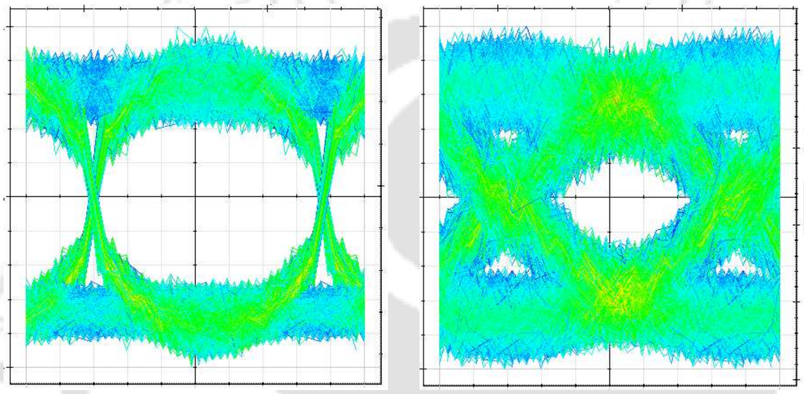

(a) *ER*: 2.97 dB, BER: ~ 10^{-30} **(b)** *ER*: 2.67 dB, BER: ~ 10^{-10}

Fig. 7.9: Eye diagram at 80 Gbps of (a) SiGe MZM and (b) Si MZM (the ER and BER of each MZM is given in the subcaptions).

7.7(a) and (b) for the SiGe and Si MZM, respectively. The data rates are taken to be 70 Gbps, 80 Gbps, and 90 Gbps. The SMF length is varied from 0 to 50 km. It can be seen that for any SMF length, the SiGe MZM shows better performance compared to the Si MZM. The BER increases with data rate and fiber length. Higher data rate transmission can be achieved with the same BER using SiGe MZM compared to the Si MZM. For error-free operation (BER = 10^{-12}), the SMF length at 70 Gbps is 22.5 km and 13.6 km for SiGe and Si MZM, respectively. The BER also varies with the received power. The change in BER with received power at 80 Gbps operation is shown in Fig. 7.8. It can be seen that the SiGe MZM has higher received power tolerance than the Si MZM to achieve the same BER performance. The eye diagram of both MZMs is shown in Fig. 7.9 from which it can be observed that SiGe MZM has a wider eye opening compared to Si MZM. Also, the asymmetricity of the eye can be observed. This is due to the non-linear phase-voltage relation of FCPD based Si modulators [179].

Table 7.2: Performance metrics of the MZMs over 50 km fiber transmission with BER below HD-FEC threshold.

MZM	P_t (mW)	*Bit Rate* (Gbps)	E_b (pJ/bit)
SiGe	47.4	80	0.59
Si	38.9	53	0.73

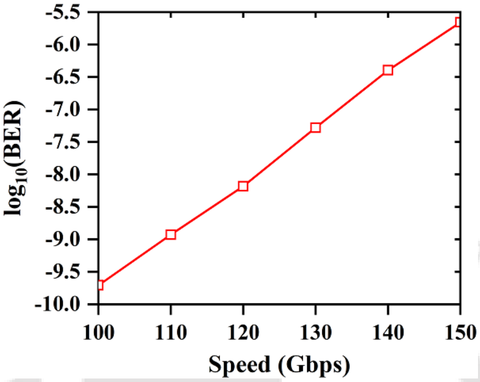

Fig. 7.10: BER as a function of modulation speed for the dual-arm driven SiGe MZM.

Energy per bit (E_b) of both MZMs are determined for 50 km SMF transmission at the hard-decision forward-error-correction (HD-FEC) threshold (BER = 3.8×10^{-3}). The speed, power, and energy per bit of SiGe and Si MZM are shown in Table 7.2. The power consumption of the SiGe MZM is more compared to the Si MZM due to the lower characteristic impedance of the SiGe TWE arm. However, the higher speed of the SiGe MZM results in lower E_b compared to the Si MZM.

In Fig. 7.7, the data rate is limited to 90 Gbps due to the high BER of the Si MZM. However, beyond 100G transmission over a single channel is possible using the SiGe MZM. The BER as a function of the modulation speed is shown in Fig. 7.10. The BER increases from 1.96×10^{-10} at 100 Gbps to 2.20×10^{-06} at 150 Gbps. The E_b at 150 Gbps is 0.32 pJ/bit. Beyond 100G NRZ-OOK modulation over a single channel can be achieved using dual-arm driven SiGe MZM, and is suitable for 400G applications without the requirement of higher-order modulation formats.

7.7 Performance comparison

The SiGe MZM is compared with recent literature and is given in Table 7.3 from which it can be observed that the proposed SiGe MZM achieves better overall performance with OOK drive compared to the state-of-the-art silicon modulators.

Table 7.3: Comparison of MZM performance metrics

Ref.	$V_\pi L_\pi$ (V.cm)	IL (dB)	f_{3dB} (GHz)	Modulation	Speed (Gbps)	BER	ER (dB)	E_b (pJ/bit)
[180]*	1.4	8	28 (EE 6dB)	QPSK	64	2.1×10^{-05}	–	7.1
[181]*	–	5 (on-chip)	38	PAM-8	114	< HD-FEC	–	7.7
[154]*	1.4	4.4	58	OOK	90	–	3.3	–
				PAM-4	112	–	2.7	–
[182]*	2.2	2.5	70	OOK	100	–	5.0	
This work**	0.83	2.14	77.48	OOK	150	2.2×10^{-06}	2.6	0.32

* Experimental result; ** Simulation result.

Table 7.4: Comparison of the designed MZM with other material platforms.

Ref.	Material	Structure	$V_\pi L_\pi$ (V.cm)	IL (dB)	f_{3dB} (GHz)	Speed (Gbps)	ER (dB)	E_b (pJ/bit)
[183]*	Graphene	MOS	25 V, 30 μm	0.9	35 (25 V)	–	–	1.4
[184]*	InGaAsP	MOS	0.09 (250 μm)	1.0	2.6 (dep.)	32	3.1	–
[185]*	InGaAsP	PN	0.4	4.5	–	40 (error-free)	–	–
[186]*	InP	n-i-p-n	2 V, 3 mm	2	67	100	>10	–
This work**	Ge-doped Si	PN	0.83	2.14	77.48	150	2.6	0.32

* Experimental result; ** Simulation result.

To show the effectiveness of silicon photonic modulators, Table 7.4 gives the comparison of the designed modulator with modulators realized in other material platforms.

7.8 Summary

The performance of a Si traveling-wave MZM is enhanced by implanting Ge to form a graded SiGe profile. The SiGe PN phase shifter is process simulated and compared with a Si PN phase shifter created using the same process flow. The SiGe phase shifter has 2.4× higher phase shift and better modulation efficiency at -5 V. The lesser length of the SiGe phase shifters results in 1.29× higher 3 dB modulation bandwidth compared to Si. The BER performance is evaluated for varying SMF lengths and received power levels. For the same fiber transmission length and bit rate, lower BER is achieved for SiGe MZM compared to Si MZM. Also, SiGe MZM has more received power tolerance compared to Si MZM for the same BER level. For 50 km transmission below the HD-FEC threshold, the SiGe MZM has 1.24× lower energy per bit (E_b) at 1.51× higher speed compared to Si MZM. The SiGe MZM can achieve beyond 100G operation over a single channel with a BER of 2.2×10^{-06} and E_b of 0.32 pJ/bit at 150 Gbps data rate. The graded SiGe traveling-wave MZM is suitable for 400G applications without the requirement of higher modulation formats.

8

Summary and Future Work

Contents

8.1 Summary of contributions

In this section, a summary and list of the findings during this thesis work are presented. This thesis presents

(i) **Mode, dispersion, and loss characteristics of a graded-index SiGe strip waveguide**

In this study, the mode, loss, and dispersion characteristics of a buried strip waveguide have been calculated for CWDM wavelengths. Process simulation has been used to form the graded-index core by Ge implantation in Si. QV-FDM has been used to calculate the number of propagating modes, effective indices, material absorption, mode confinement, and dispersion parameters. The scattering loss has been determined from the P-L model. The zero dispersion for higher-order modes occurs in the O-band, which is suitable for short-reach multimodal applications. The usable waveguide length and the number of modes have been characterized and are limited by the mode with the highest propagation loss/dispersion and lowest mode confinement, respectively.

(ii) **A 2D model of Si PN phase shifter**

A 2D model of a silicon lateral PN optical phase shifter is presented, which can be used for multiple parameter study and optimization of the device performance without the need of any commercial numerical tools. The model shows good agreement with TCAD simulation and can be used to calculate the phase shift, absorption loss, modulation efficiency, and insertion loss of the phase shifter. Multiple parameter study includes the waveguide dimensions, operating wavelength, cladding material, doping concentrations, junction offset, and applied voltage. The model employs the effective index method to determine the mode properties and construct the 2D mode field. The PN diode is modeled by taking into account the fringing electric field at the core-cladding interface, which results in a wider depletion region near the interface. Multiple loss components are discussed, and the scattering loss and free-carrier absorption are modeled using P-L and Soref model, respectively. The model uses the 2D modal overlap with the 2D carrier distribution across the waveguide to calculate the phase shifter performance metrics. The algorithm used to model the 2D nature of the PN diode depletion region is presented in detail and uses mathematical and analytical formulas instead of numerical methods, making the model faster and easy to implement, with accuracy in par with commercial tools.

(iii) **Performance analysis of a quasi-TM mode Si optical MZM**

A Si MZM with quasi-TM mode propagation is investigated for NRZ-OOK modulation. The quasi-TM PN phase shifter phase-loss characteristics have been determined and shown to exhibit better performance compared to quasi-TE phase shifter with the same waveguide cross-sectional area and device parameters. The phase shifter modulation efficiency is 1.02 V.cm with RC limited bandwidth of 46 GHz at 5 V reverse bias. The MZM transfer characteristics are determined for the dual-arm push-pull driving scheme, and a TWE structure is employed to enhance the device bandwidth. A 3 dB bandwidth of 74 GHz is obtained at 2.5 V reverse bias. The high-speed modulator characteristics are studied for different data rates over SMF transmission. A 30 km fiber transmission with an open eye at 160 Gbps with 2 V_{pp} drive is obtained with an extinction ratio of 2.3 dB, BER of $\sim 2.77 \times 10^{-06}$, and energy per bit of 0.45 pJ/bit. The effect of fiber dispersion on the BER shows dispersion tolerance from 0 $ps.nm^{-1}.km^{-1}$ to -1.73 $ps.nm^{-1}.km^{-1}$ for 30 km fiber transmission below the HD-FEC threshold at 100 Gbps operation.

(iv) **Designing a multi-layer SiGe PN phase shifter**

A graded-index strained $Si_{1-x}Ge_x$ optical PN phase shifter with multiple strained layers has been proposed for high-speed data modulation at 1550 nm with low device footprint. The QV-FDM, NL-EPM, and the P-L model have been used to analyze the proposed device. A phase shift of 122°/mm, $V_\pi L_\pi$ of 0.74 V.cm, and insertion loss of 4 dB at 5 V reverse bias with a 3-dB modulation bandwidth of 27.5 GHz has been obtained for a 500 nm × 250 nm cross-section rib waveguide with 50 nm slab. A 15°/mm increase in phase shift and 0.08 V.cm decrease in $V_\pi L_\pi$ has been observed when the junction is shifted by 60 nm towards the N side.

(v) **Process simulation study of a lateral junction Ge-doped Si PN phase shifter**

This study analyzes the effect of Ge doping on the performance of an optical PN phase shifter in silicon photonics platform. The fabrication process flow is defined using a 2D process simulation tool to create the phase shifter structure. The mode, material, and loss parameters of the designed phase shifter are calculated, and the performance is compared with a Si phase shifter. A 1.84× higher phase shift, 1.27× lower absorption, and 1.50× lower insertion loss is obtained for the SiGe phase shifter compared to Si.

(vi) **Process simulation study of a vertical junction Ge-doped Si PN phase shifter**

The performance of a Ge-doped Si optical phase shifter with vertical PN junction has been investigated. The proposed phase shifter is simulated using a process simulation tool, and the 2D carrier distribution has been used to calculate the phase shifter performance metrics. The proposed phase shifter has a phase shift of ~141°/mm, $V_\pi L_\pi$ of ~0.64 V.cm, insertion loss of ~1.23 dB and 3-dB bandwidth of ~37 GHz at 5 V reverse bias.

(vii) **Performance analysis of a Ge-doped Si optical MZM**

The performance of a Si MZM is enhanced by using device-level engineering techniques that involve material engineering and junction optimizations. The FCPD effect, which is used for modulation in Si, is enhanced by implanting Ge in Si, forming a graded SiGe core. Comparison of the process simulated SiGe phase shifter with a Si phase shifter shows 2.4× higher phase shift at -5 V for 1550 nm wavelength operation. Both single-arm and dual-arm drive are investigated for both SiGe and Si MZMs. A TWE is used to enhance the modulation bandwidth. Both single-arm and dual-arm driven SiGe MZM achieves better performance in terms of modulation bandwidth, modulation speed, fiber transmission length, and energy per bit, compared to the corresponding Si MZM. The BER performance over SMF transmission and received power levels are simulated. The dual-arm driven SiGe MZM can achieve 150 Gbps transmission at BER of 2.2×10^{-06} and energy per bit of 0.32 pJ/bit with a 3 dB bandwidth of 77.48 GHz at -2 V and 2 V_{pp} drive voltage using NRZ-OOK modulation.

8.2 Future work

This thesis focusses on the performance enhancement of silicon optical modulators using device-level engineering technique, specifically using Ge to enhance the modulation efficiency. The thesis also includes the study of a Ge-doped Si strip waveguide for multimodal applications in the CWDM band and the modeling of a silicon PN optical phase shifter. Since the study is simulation-based, there are many inherent assumptions, and further study is necessary. Some possible directions in which the present work can be extended are

(i) Inclusion of semiconductor physics model to improve the accuracy of the silicon PN phase shifter model at higher doping concentrations.

(ii) The silicon PN phase shifter model can be extended to determine the performance of a silicon-germanium PN phase shifter.

(iii) Further improvement in performance can be made by process simulation optimization. The effect of different ion implantation conditions and the number of steps for each ion species need to be analyzed.

(iv) The fabrication and characterization of the proposed graded-SiGe MZM may be followed and validated with the simulation work presented in this thesis.

A

Appendix: Waveguide Losses

The mode suffers loss while propagating through the waveguide. The main contributions to the propagation loss comes from the intrinsic material absorption, free carrier absorption (FCA), substrate leakage loss, polarization dependent loss (PDL), and sidewall scattering loss. The intrinsic material absorption loss can be calculated from (3.3). The FCA is due to dopant ions and can be calculated as [187]:

$$\alpha_{FCA} = \int_{\hat{x}} \int_{\hat{y}} \frac{q^3 \lambda^2}{4\pi^2 c^3 \epsilon_0 n} \left(\frac{N_e(\hat{x},\hat{y})}{\left[m^*_{ce}(\hat{x},\hat{y})\right]^2 \mu_e(\hat{x},\hat{y})} + \frac{N_h(\hat{x},\hat{y})}{\left[m^*_{ch}(\hat{x},\hat{y})\right]^2 \mu_h(\hat{x},\hat{y})} \right) d\hat{x}\, d\hat{y} \tag{A.1}$$

The electron and hole mobility as a function of doping can be determined from [172, 188].

FCA is absent if the waveguide is intrinsic, and no carrier dopants are introduced. The substrate leakage loss occurs when the BOX (lower cladding) is sufficiently thin such that mode leaks to the underneath silicon substrate. This loss can be substantial since higher-order modes are poorly confined and leak to a much greater depth in the cladding. Proper design should ensure sufficient cladding layer thickness such that the evanescent field decays within the cladding. The substrate leakage can be determined either analytically and/or numerically if required [189]. For small waveguide length, the mode polarization does not change, and thus

PDL can be neglected without any appreciable error. The sidewall scattering loss occurs due to sidewall roughness as a result of etching and is proportional to the mode intensity at the sidewalls. The scattering loss of each supported mode at different wavelengths can be determined from the P-L model [102], which decomposes the 2D cross-section waveguide into 1D slab waveguides. The scattering loss is characterized by standard deviation (σ) and correlation length (L_c) and is shown below for the E^y mode [145].

$$\alpha_{scat} = \frac{f.g.\gamma.S_w.\sigma^2}{\sqrt{2}k_0 n_{core}} \tag{A.2}$$

where

$$k_0 = \frac{2\pi}{\lambda} \tag{A.3}$$

S_w, g, f, and γ are calculated as

$$S_w = \frac{\frac{\delta n^r_{eff}}{\delta w}}{\frac{\delta n^s_{eff}}{\delta w}} \tag{A.4}$$

where superscripts 'r' and 's' denotes rib and strip waveguide of the same cross-section, and w represents the waveguide width.

$$g = \frac{k_0^4 (n_{core}^2 - n_{eff}^2)(n_{core}^2 - n_{clad}^2)}{1 + \frac{w.k_0 \sqrt{n_{eff}^2 - n_{clad}^2}}{2}} \tag{A.5}$$

$$f = \frac{a\sqrt{1 - a^2 + \sqrt{(1 + a^2)^2 + 2a^2b^2}}}{\sqrt{(1 + a^2)^2 + 2a^2b^2}} \tag{A.6}$$

where,

$$a = k_0.L_c \sqrt{n_{eff}^2 - n_{clad}^2}\,, \; b = \frac{n_{clad}}{n_{core}} \sqrt{\frac{n_{core}^2 - n_{clad}^2}{\Delta(n_{eff}^2 - n_{clad}^2)}}\,, \; \Delta = \frac{n_{core}^2 - n_{clad}^2}{2n_{core}^2} \tag{A.7}$$

$$\gamma = \frac{n^{\parallel}_{eff}}{n^{\perp}_{eff}} \frac{\cos\left(\frac{k_0.w}{2}\sqrt{n_{core}^2 - n^{\perp}_{eff}}\right)}{\cos\left(\frac{k_0.w}{2}\sqrt{n_{core}^2 - n^{\parallel}_{eff}}\right)} \sqrt{\frac{n_{core}^2 - n^{\perp}_{eff}}{n_{core}^2 - n^{\parallel}_{eff}}} \tag{A.8}$$

where the superscripts '∥' and '⊥' refers to the parallel and perpendicular interaction of the mode electric field with the sidewalls corresponding to the E^x and E^y mode of the planar waveguide respectively. Since the scattering loss is directly proportional to the mode intensity at the sidewalls, S_w given by (A.4) is a scaling ratio needed because of the reduction in the sidewall height due to the slab layer. The perpendicular interaction of the E_y mode with the sidewalls is taken into account by γ. The value of σ and L_c are taken to be 2 nm and 50 nm, respectively, which is valid for a waveguide with a small cross-section [121]. The sidewall scattering loss of E^x mode can be similarly determined and does not depend on γ since the E^x mode direction is parallel to the waveguide sidewall.

Bibliography

[1] B. Jalali and S. Fathpour, “Silicon photonics,” *Journal of Lightwave Technology*, vol. 24, no. 12, pp. 4600–4615, 2006.

[2] K. Narayanan and S. F. Preble, “Optical nonlinearities in hydrogenated-amorphous silicon waveguides,” *Optics Express*, vol. 18, no. 9, pp. 8998–9005, 2010.

[3] A. M. Agarwal, L. Liao, J. S. Foresi, M. R. Black, X. Duan, and L. Kimerling, “Low-loss polycrystalline silicon waveguides for silicon photonics,” *Journal of Applied Physics*, vol. 80, no. 11, pp. 6120–6123, 1996.

[4] F. Cunin, T. A. Schmedake, J. R. Link, Y. Y. Li, J. Koh, S. N. Bhatia, and M. J. Sailor, “Biomolecular screening with encoded porous-silicon photonic crystals,” *Nature Materials*, vol. 1, no. 1, pp. 39–41, 2002.

[5] L. L. Y. Voon and G. Guzmán-Verri, “Is silicene the next graphene?” *MRS Bulletin*, vol. 39, no. 4, pp. 366–373, 2014.

[6] M. Salib, L. Liao, R. Jones, M. Morse, A. Liu, D. Samara-Rubio, D. Alduino, and M. Paniccia, “Silicon photonics,” *Intel Technology Journal*, vol. 8, no. 2, 2004.

[7] B.-S. Song, S. Yamada, T. Asano, and S. Noda, “Demonstration of two-dimensional photonic crystals based on silicon carbide,” *Optics Express*, vol. 19, no. 12, pp. 11 084–11 089, 2011.

[8] K. Ikeda, R. E. Saperstein, N. Alic, and Y. Fainman, “Thermal and kerr nonlinear properties of plasma-deposited silicon nitride/silicon dioxide waveguides,” *Optics Express*, vol. 16, no. 17, pp. 12 987–12 994, 2008.

[9] K. Lee, Y.-K. Fang, W. J. Lee, J.-J. Ho, K. Chen, and K. Liao, “Novel electrochromic devices (ECD) of tungsten oxide (WO_3) thin film integrated with amorphous silicon germanium photodetector for hydrogen sensor,” *Sensors and Actuators B: Chemical*, vol. 69, no. 1-2, pp. 96–99, 2000.

[10] R. Soref, “Silicon-based silicon–germanium–tin heterostructure photonics,” *Philosophical Transactions of the Royal Society A: Mathematical, Physical and Engineering Sciences*, vol. 372, no. 2012, p. 20130113, 2014.

[11] S. Yan, X. Zhu, L. H. Frandsen, S. Xiao, N. A. Mortensen, J. Dong, and Y. Ding, “Slow-light-enhanced energy efficiency for graphene microheaters on silicon photonic crystal waveguides,” *Nature Communications*, vol. 8, no. 1, pp. 1–8, 2017.

[12] P. O. Weigel, M. Savanier, C. T. DeRose, A. T. Pomerene, A. L. Starbuck, A. L. Lentine, V. Stenger, and S. Mookherjea, “Lightwave circuits in lithium niobate through hybrid waveguides with silicon photonics,” *Scientific Reports*, vol. 6, p. 22301, 2016.

[13] S. Lourdudoss, “Heteroepitaxy and selective area heteroepitaxy for silicon photonics,” *Current Opinion in Solid State and Materials Science*, vol. 16, no. 2, pp. 91–99, 2012.

[14] S. Abel, T. Stöferle, C. Marchiori, D. Caimi, L. Czornomaz, M. Stuckelberger, M. Sousa, B. J. Offrein, and J. Fompeyrine, “A hybrid barium titanate–silicon photonics platform for ultraefficient electro-optic tuning,” *Journal of Lightwave Technology*, vol. 34, no. 8, pp. 1688–1693, 2016.

[15] J. Bland-Hawthorn, J. Lawrence, G. Robertson, S. Campbell, B. Pope, C. Betters, S. Leon-Saval, T. Birks, R. Haynes, N. Cvetojevic *et al.*, “PIMMS: photonic integrated multimode microspectrograph,” in *Ground-based and Airborne Instrumentation for Astronomy III*, vol. 7735. International Society for Optics and Photonics, 2010, p. 77350N.

[16] R. C. Bailey, A. L. Washburn, A. J. Qavi, M. Iqbal, M. Gleeson, F. Tybor, and L. C. Gunn, “A robust silicon photonic platform for multiparameter biological analysis,” in *Silicon Photonics IV*, vol. 7220. International Society for Optics and Photonics, 2009, p. 72200N.

[17] R. Dersch, M. Steinhart, U. Boudriot, A. Greiner, and J. Wendorff, “Nanoprocessing of polymers: applications in medicine, sensors, catalysis, photonics,” *Polymers for Advanced Technologies*, vol. 16, no. 2-3, pp. 276–282, 2005.

[18] Y. A. Vlasov, “Silicon CMOS-integrated nano-photonics for computer and data communications beyond 100G,” *IEEE Communications Magazine*, vol. 50, no. 2, pp. s67–s72, 2012.

[19] S. S. El Nasr-Storey, F. Boeuf, C. Baudot, S. Detraz, J. M. Fedeli, D. Marris-Morini, L. Olantera, G. Pezzullo, C. Sigaud, C. Soos *et al.*, “Effect of radiation on a mach–zehnder interferometer silicon modulator for HL–LHC data transmission applications,” *IEEE Transactions on Nuclear Science*, vol. 62, no. 1, pp. 329–335, 2015.

[20] S. S. El Nasr-Storey, F. Boeuf, C. Baudot, S. Detraz, J.-M. Fedeli, D. Marris-Morini, L. Olantera, G. Pezzullo, C. Sigaud, C. Soos *et al.*, “Silicon photonics for high energy physics data transmission applications,” in *11th International Conference on Group IV Photonics (GFP)*. IEEE, 2014, pp. 1–2.

[21] S. Chen, W. Li, J. Wu, Q. Jiang, M. Tang, S. Shutts, S. N. Elliott, A. Sobiesierski, A. J. Seeds, I. Ross *et al.*, “Electrically pumped continuous-wave III–V quantum dot lasers on silicon,” *Nature Photonics*, vol. 10, no. 5, p. 307, 2016.

[22] S. S. Iyer and Y.-H. Xie, “Light emission from silicon,” *Science*, vol. 260, no. 5104, pp. 40–46, 1993.

[23] M. Fujita, Y. Tanaka, and S. Noda, “Light emission from silicon in photonic crystal nanocavity,” *IEEE Journal of Selected Topics in Quantum Electronics*, vol. 14, no. 4, pp. 1090–1097, 2008.

[24] Y. Kanemitsu, “Light emission from porous silicon and related materials,” *Physics Reports*, vol. 263, no. 1, pp. 1–91, 1995.

[25] M. E. Castagna, S. Coffa, M. Monaco, L. Caristia, A. Messina, R. Mangano, and C. Bongiorno, “Si-based materials and devices for light emission in silicon,” *Physica E: Low-dimensional Systems and Nanostructures*, vol. 16, no. 3-4, pp. 547–553, 2003.

[26] J. R. Jain, A. Hryciw, T. M. Baer, D. A. Miller, M. L. Brongersma, and R. T. Howe, “A micromachining-based technology for enhancing germanium light emission via tensile strain,” *Nature Photonics*, vol. 6, no. 6, p. 398, 2012.

[27] Q. Zhang, Y. Liu, G. Han, Y. Shao, X. Gao, C. Zhang, J. Zhang, and Y. Hao, "Theoretical analysis of performance enhancement in GeSn/SiGeSn light-emitting diode enabled by Si_3N_4 liner stressor technique," *Applied Optics*, vol. 55, no. 34, pp. 9668–9674, 2016.

[28] G. Sun, R. Soref, and H. Cheng, "Design of an electrically pumped SiGeSn/GeSn/SiGeSn double-heterostructure midinfrared laser," *Journal of Applied Physics*, vol. 108, no. 3, p. 033107, 2010.

[29] H. Rong, A. Liu, R. Jones, O. Cohen, D. Hak, R. Nicolaescu, A. Fang, and M. Paniccia, "An all-silicon Raman laser," *Nature*, vol. 433, no. 7023, pp. 292–294, 2005.

[30] S. S. Azadeh, F. Merget, M. Nezhad, and J. Witzens, "On the measurement of the Pockels effect in strained silicon," *Optics Letters*, vol. 40, no. 8, pp. 1877–1880, 2015.

[31] C. L. Manganelli, P. Pintus, and C. Bonati, "Modeling of strain-induced Pockels effect in silicon," *Optics Express*, vol. 23, no. 22, pp. 28 649–28 666, 2015.

[32] G. T. Reed, G. Mashanovich, F. Y. Gardes, and D. Thomson, "Silicon optical modulators," *Nature Photonics*, vol. 4, no. 8, p. 518, 2010.

[33] "Silicon photonics market research report – global forecast till 2024," https://www.marketresearchfuture.com/reports/silicon-photonics-market-2809.

[34] B. Dhoedt, R. Baets, P. Van Daele, P. Heremans, J. Van Campenhout, J. Hall, R. Michalzik, A. Schmid, H. Thienpont, R. Vounckx *et al.*, "Optically interconnected integrated circuits to solve the CMOS interconnect bottleneck," in *1998 Proceedings. 48th Electronic Components and Technology Conference (Cat. No. 98CH36206)*. IEEE, 1998, pp. 992–998.

[35] A. C. Cangellaris, "The interconnect bottleneck in multi-GHz processors; new opportunities for hybrid electrical/optical solutions," in *Proceedings. Fifth International Conference on Massively Parallel Processing (Cat. No. 98EX182)*. IEEE, 1998, pp. 96–103.

[36] A. Ghiasi, "Large data centers interconnect bottlenecks," *Optics Express*, vol. 23, no. 3, pp. 2085–2090, 2015.

[37] T. L. Paoli and J. E. Ripper, "Direct modulation of semiconductor lasers," *Proceedings of the IEEE*, vol. 58, no. 10, pp. 1457–1465, 1970.

[38] Y. Fu, X. Hu, C. Lu, S. Yue, H. Yang, and Q. Gong, "All-optical logic gates based on nanoscale plasmonic slot waveguides," *Nano Letters*, vol. 12, no. 11, pp. 5784–5790, 2012.

[39] N. Zhao, X. Li, G. Li, and J. M. Kahn, "Capacity limits of spatially multiplexed free-space communication," *Nature Photonics*, vol. 9, no. 12, p. 822, 2015.

[40] G. Milione, M. P. Lavery, H. Huang, Y. Ren, G. Xie, T. A. Nguyen, E. Karimi, L. Marrucci, D. A. Nolan, R. R. Alfano *et al.*, "4× 20 Gbit/s mode division multiplexing over free space using vector modes and a q-plate mode (de) multiplexer," *Optics Letters*, vol. 40, no. 9, pp. 1980–1983, 2015.

[41] G. Jain, P. M. Anandarajah, R. McKenna, D. Gutierrez-Pascual, F. Smyth, J. Braddell, and J. F. Donegan, "Athermal chirp-compensated directly modulated PIC for uncooled DWDM," in *Integrated Optics: Devices, Materials, and Technologies XXIV*, vol. 11283. International Society for Optics and Photonics, 2020, p. 112831X.

[42] C. Adams, "A mechanical shutter for light using piezoelectric actuators," *Review of Scientific Instruments*, vol. 71, no. 1, pp. 59–60, 2000.

[43] M. Okazaki and T. Suhara, “High-performance 1024-pixel EO spatial light modulator using cascaded periodically-poled Raman-Nath gratings,” *Journal of Lightwave Technology*, vol. 33, no. 24, pp. 5195–5200, 2015.

[44] I. Mhaouech, V. Coda, G. Montemezzani, M. Chauvet, and L. Guilbert, “Integrated low drive voltage electro-optic Bragg modulator using a periodically poled lithium niobate,” in *2017 Conference on Lasers and Electro-Optics Europe & European Quantum Electronics Conference (CLEO/Europe-EQEC)*. IEEE, 2017, pp. 1–1.

[45] M. Nedeljkovic, S. Stanković, C. J. Mitchell, A. Z. Khokhar, S. A. Reynolds, D. J. Thomson, F. Y. Gardes, C. G. Littlejohns, G. T. Reed, and G. Z. Mashanovich, “Mid-infrared thermo-optic modulators in SoI,” *IEEE Photonics Technology Letters*, vol. 26, no. 13, pp. 1352–1355, 2014.

[46] T. Nakamura, S. Tani, I. Ito, and Y. Kobayashi, “Magneto-optic modulator for high bandwidth cavity length stabilization,” *Optics Express*, vol. 25, no. 5, pp. 4994–5000, 2017.

[47] V. R. Almeida, C. A. Barrios, R. R. Panepucci, and M. Lipson, “All-optical control of light on a silicon chip,” *Nature*, vol. 431, no. 7012, pp. 1081–1084, 2004.

[48] C. Wang, M. Zhang, B. Stern, M. Lipson, and M. Lončar, “Nanophotonic lithium niobate electro-optic modulators,” *Optics Express*, vol. 26, no. 2, pp. 1547–1555, 2018.

[49] D. V. Simili, M. Cada, and J. Pistora, “Silicon slot waveguide electro-optic Kerr effect modulator,” *IEEE Photonics Technology Letters*, vol. 30, no. 9, pp. 873–876, 2018.

[50] N. Abadia, T. Bernadin, P. Chaisakul, S. Olivier, D. Marris-Morini, R. E. de Lamaëstre, J. Weeber, and L. Vivien, “Low-power consumption Franz-Keldysh effect plasmonic modulator,” *Optics Express*, vol. 22, no. 9, pp. 11 236–11 243, 2014.

[51] Y.-H. Kuo, Y. K. Lee, Y. Ge, S. Ren, J. E. Roth, T. I. Kamins, D. A. Miller, and J. S. Harris, “Strong quantum-confined Stark effect in germanium quantum-well structures on silicon,” *Nature*, vol. 437, no. 7063, pp. 1334–1336, 2005.

[52] R. Soref and B. Bennett, “Electrooptical effects in silicon,” *IEEE Journal of Quantum Electronics*, vol. 23, no. 1, pp. 123–129, 1987.

[53] R. A. Soref and B. R. Bennett, “Kramers-Kronig analysis of electro-optical switching in silicon,” in *Integrated Optical Circuit Engineering IV*, vol. 704. International Society for Optics and Photonics, 1987, pp. 32–37.

[54] P. Dong, L. Chen, and Y.-k. Chen, “High-speed low-voltage single-drive push-pull silicon Mach-Zehnder modulators,” *Optics express*, vol. 20, no. 6, pp. 6163–6169, 2012.

[55] H. Xu, X. Li, X. Xiao, P. Zhou, Z. Li, J. Yu, and Y. Yu, “High-speed silicon modulator with band equalization,” *Optics letters*, vol. 39, no. 16, pp. 4839–4842, 2014.

[56] R. Dubé-Demers, S. LaRochelle, and W. Shi, “Ultrafast pulse-amplitude modulation with a femtojoule silicon photonic modulator,” *Optica*, vol. 3, no. 6, pp. 622–627, 2016.

[57] M. Shin, Y. Ban, B.-M. Yu, M.-H. Kim, J. Rhim, L. Zimmermann, and W.-Y. Choi, “A linear equivalent circuit model for depletion-type silicon microring modulators,” *IEEE Transactions on Electron Devices*, vol. 64, no. 3, pp. 1140–1145, 2017.

[58] J. Sun, R. Kumar, M. Sakib, J. B. Driscoll, H. Jayatilleka, and H. Rong, “A 128 Gb/s PAM4 silicon microring modulator with integrated thermo-optic resonance tuning,” *Journal of Lightwave Technology*, vol. 37, no. 1, pp. 110–115, 2019.

[59] X. Ruan, L. Zhang, F. Yang, Y. Zhu, Y. Li, and F. Zhang, “Beyond 100G single sideband PAM-4 transmission with silicon dual-drive MZM,” *IEEE Photonics Technology Letters*, vol. 31, no. 7, pp. 509–512, 2019.

[60] A. Giuglea, G. Belfiore, M. Khafaji, R. Henker, D. Petousi, G. Winzer, L. Zimmermann, and F. Ellinger, “Comparison of segmented and traveling-wave electro-optical transmitters based on silicon photonics Mach-Zehnder modulators,” in *2018 Photonics in Switching and Computing (PSC)*. IEEE, 2018, pp. 1–3.

[61] H. Yu and W. Bogaerts, “An equivalent circuit model of the traveling wave electrode for carrier-depletion-based silicon optical modulators,” *Journal of Lightwave Technology*, vol. 30, no. 11, pp. 1602–1609, 2012.

[62] E. Chen and S. Y. Chou, “Characteristics of coplanar transmission lines on multilayer substrates: Modeling and experiments,” *IEEE Transactions on Microwave Theory and Techniques*, vol. 45, no. 6, pp. 939–945, 1997.

[63] E. Carlsson and S. Gevorgian, “Conformal mapping of the field and charge distributions in multilayered substrate cpws,” *IEEE Transactions on Microwave Theory and Techniques*, vol. 47, no. 8, pp. 1544–1552, 1999.

[64] K. Ogawa, H. Ishihara, K. Goi, Y. Mashiko, S. T. Lim, M. J. Sun, S. Seah, C. E. Png, T.-Y. Liow, X. Tu *et al.*, “Fundamental characteristics and high-speed applications of carrier-depletion silicon Mach-Zehnder modulators,” *IEICE Electronics Express*, vol. 11, no. 24, pp. 1–15, 2014.

[65] B. Mardiana, S. Shaari, P. S. Menon, H. Hazura, A. Hanim, N. Arsad, and H. Abdullah, “Analyses for various doping structures of SOI-based optical phase modulator using free carrier dispersion effect,” *Optik-International Journal for Light and Electron Optics*, vol. 125, no. 6, pp. 1800–1803, 2014.

[66] Y. Taguchi, S. Takagi, and M. Takenaka, “Numerical analysis of Ge/Si hybrid MOS optical modulator operating at mid-infrared wavelength,” *Japanese Journal of Applied Physics*, vol. 58, no. SB, p. SBBE03, 2019.

[67] G. Rasigade, D. Marris-Morini, M. Ziebell, E. Cassan, and L. Vivien, “Analytical model for depletion-based silicon modulator simulation,” *Optics Express*, vol. 19, no. 5, pp. 3919–3924, 2011.

[68] E. Temporiti, A. Ghilioni, G. Minoia, P. Orlandi, M. Repossi, D. Baldi, and F. Svelto, “Insights into silicon photonics Mach–Zehnder-based optical transmitter architectures,” *IEEE Journal of Solid-State Circuits*, vol. 51, no. 12, pp. 3178–3191, 2016.

[69] A. Samani, E. El-Fiky, M. Osman, D. Patel, R. Li, M. Jacques, and D. Plant, “180 Gb/s single carrier single polarization 16-Qam transmission using an O-band silicon photonic IQM,” *Optics Express*, vol. 27, no. 10, pp. 14 447–14 456, 2019.

[70] E. El-Fiky, A. Samani, D. Patel, M. Jacques, M. Sowailem, and D. V. Plant, “400 Gb/s O-band silicon photonic transmitter for intra-datacenter optical interconnects,” *Optics Express*, vol. 27, no. 7, pp. 10 258–10 268, 2019.

[71] H. Sepehrian, J. Lin, L. A. Rusch, and W. Shi, “Silicon photonic IQ modulators for 400 Gb/s and beyond,” *Journal of Lightwave Technology*, vol. 37, no. 13, pp. 3078–3086, 2019.

[72] N. Eiselt, J. Wei, H. Griesser, A. Dochhan, M. Eiselt, J.-P. Elbers, J. J. V. Olmos, and I. T. Monroy, “First real-time 400G PAM-4 demonstration for inter-data center transmission over 100 km of SSMF at 1550 nm,” in *2016 Optical Fiber Communications Conference and Exhibition (OFC)*. IEEE, 2016, pp. 1–3.

[73] L. Deniel, M. Gay, D. P. Galacho, C. Baudot, L. Bramerie, O. Ozolins, F. Boeuf, L. Vivien, C. Peucheret, and D. Marris-Morini, “DAC-less PAM-4 generation in the O-band using a silicon Mach-Zehnder modulator,” *Optics Express*, vol. 27, no. 7, pp. 9740–9748, 2019.

[74] O. Dubray, A. Abraham, K. Hassan, S. Olivier, D. Marris-Morini, L. Vivien, I. O’Connor, and S. Menezo, “Electro-optical ring modulator: An ultracompact model for the comparison and optimization of pn, pin, and capacitive junction,” *IEEE Journal of Selected Topics in Quantum Electronics*, vol. 22, no. 6, pp. 89–98, 2016.

[75] C. E. Png, M. J. Sun, S. T. Lim, T. Y. Ang, and K. Ogawa, “Numerical modeling and analysis for high-efficiency carrier-depletion silicon rib-waveguide phase shifters,” *IEEE Journal of Selected Topics in Quantum Electronics*, vol. 22, no. 6, pp. 99–106, 2016.

[76] D. Pérez-Galacho, D. Marris-Morini, R. Stoffer, E. Cassan, C. Baudot, T. Korthorst, F. Boeuf, and L. Vivien, “Simplified modeling and optimization of silicon modulators based on free-carrier plasma dispersion effect,” *Optics Express*, vol. 24, no. 23, pp. 26 332–26 337, 2016.

[77] H. Yu, M. Pantouvaki, J. Van Campenhout, D. Korn, K. Komorowska, P. Dumon, Y. Li, P. Verheyen, P. Absil, L. Alloatti *et al.*, “Performance tradeoff between lateral and interdigitated doping patterns for high speed carrier-depletion based silicon modulators,” *Optics Express*, vol. 20, no. 12, pp. 12 926–12 938, 2012.

[78] J. Wang, C. Qiu, H. Li, W. Ling, L. Li, A. Pang, Z. Sheng, A. Wu, X. Wang, S. Zou *et al.*, “Optimization and demonstration of a large-bandwidth carrier-depletion silicon optical modulator,” *Journal of Lightwave Technology*, vol. 31, no. 24, pp. 4119–4125, 2013.

[79] G. Rasigade, D. Marris-Morini, L. Vivien, and E. Cassan, “An optimization method for depletion-based silicon optical modulators,” in *Silicon Photonics and Photonic Integrated Circuits II*, vol. 7719. International Society for Optics and Photonics, 2010, p. 771912.

[80] I. Goykhman, B. Desiatov, S. Ben-Ezra, J. Shappir, and U. Levy, “Optimization of efficiency-loss figure of merit in carrier-depletion silicon Mach-Zehnder optical modulator,” *Optics Express*, vol. 21, no. 17, pp. 19 518–19 529, 2013.

[81] M. Takenaka and S. Takagi, “Strain engineering of plasma dispersion effect for SiGe optical modulators,” *IEEE Journal of Quantum Electronics*, vol. 48, no. 1, pp. 8–16, 2012.

[82] Y. Kim, M. Takenaka, T. Osada, M. Hata, and S. Takagi, “Strain-induced enhancement of plasma dispersion effect and free-carrier absorption in SiGe optical modulators,” *Scientific Reports*, vol. 4, p. 4683, 2014.

[83] S. Rao, G. Coppola, C. Summonte, and F. Della Corte, “Progress towards a high-performing a-Si:H-based electro-optic modulator,” *Journal of Optics*, vol. 16, no. 5, p. 055501, 2014.

[84] S. Rao and F. Della Corte, "Numerical analysis of electro-optical modulators based on the amorphous silicon technology," *Journal of Lightwave Technology*, vol. 32, no. 13, pp. 2399–2407, 2014.

[85] J. Baek, J.-B. You, and K. Yu, "Free-carrier electro-refraction modulation based on a silicon slot waveguide with ITO," *Optics Express*, vol. 23, no. 12, pp. 15 863–15 876, 2015.

[86] G. T. Reed, D. J. Thomson, F. Y. Gardes, Y. Hu, J.-M. Fedeli, and G. Z. Mashanovich, "High-speed carrier-depletion silicon Mach-Zehnder optical modulators with lateral PN junctions," *Frontiers in Physics*, vol. 2, p. 77, 2014.

[87] S. T. Lim, M. J. Sun, and C. E. Png, "Silicon optical modulator simulation," *Frontiers in Physics*, vol. 3, p. 27, 2015.

[88] M. Ziebell, D. Marris-Morini, G. Rasigade, J.-M. Fédéli, P. Crozat, E. Cassan, D. Bouville, and L. Vivien, "40 Gbit/s low-loss silicon optical modulator based on a pipin diode," *Optics Express*, vol. 20, no. 10, pp. 10 591–10 596, 2012.

[89] H. Xu, X. Xiao, X. Li, Y. Hu, Z. Li, T. Chu, Y. Yu, and J. Yu, "High speed silicon Mach-Zehnder modulator based on interleaved PN junctions," *Optics Express*, vol. 20, no. 14, pp. 15 093–15 099, 2012.

[90] K. Goi, K. Ogawa, Y. T. Tan, V. Dixit, S. T. Lim, C. E. Png, T.-Y. Liow, X. Tu, G.-Q. Lo, and D.-L. Kwong, "Silicon Mach-Zehnder modulator using low-loss phase shifter with bottom PN junction formed by restricted-depth doping," *IEICE Electronics Express*, vol. 10, no. 17, pp. 20 130 552–20 130 552, 2013.

[91] Z. Yong, W. D. Sacher, Y. Huang, J. C. Mikkelsen, Y. Yang, X. Luo, P. Dumais, D. Goodwill, H. Bahrami, P. G.-Q. Lo *et al.*, "U-shaped PN junctions for efficient silicon Mach-Zehnder and microring modulators in the O-band," *Optics Express*, vol. 25, no. 7, pp. 8425–8439, 2017.

[92] Y. Liu, S. Dunham, T. Baehr-Jones, A. E.-J. Lim, G.-Q. Lo, and M. Hochberg, "Ultra-responsive phase shifters for depletion mode silicon modulators," *Journal of Lightwave Technology*, vol. 31, no. 23, pp. 3787–3793, 2013.

[93] T. Y. Ang, C. E. Png, S. T. Lim, and J. R. Ong, "Silicon modulators with optimized vertical pn junctions for high-modulation-efficiency in the O-band," in *Silicon Photonics XIII*, vol. 10537. International Society for Optics and Photonics, 2018, p. 105370H.

[94] H. Yu, W. Bogaerts, and A. De Keersgieter, "Optimization of ion implantation condition for depletion-type silicon optical modulators," *IEEE Journal of Quantum Electronics*, vol. 46, no. 12, pp. 1763–1768, 2010.

[95] R. A. Soref, J. Schmidtchen, and K. Petermann, "Large single-mode rib waveguides in GeSi-Si and Si-on-SiO$_2$," *IEEE Journal of Quantum Electronics*, vol. 27, no. 8, pp. 1971–1974, 1991.

[96] S. P. Pogossian, L. Vescan, and A. Vonsovici, "The single-mode condition for semiconductor rib waveguides with large cross section," *Journal of Lightwave Technology*, vol. 16, no. 10, pp. 1851–1853, 1998.

[97] H. Huang, K. Liu, B. Qi, and V. J. Sorger, "Re-analysis of single-mode conditions for silicon rib waveguides at 1550 nm wavelength," *Journal of Lightwave Technology*, vol. 34, no. 16, pp. 3811–3817, 2016.

[98] G. Hocker and W. K. Burns, “Mode dispersion in diffused channel waveguides by the effective index method,” *Applied Optics*, vol. 16, no. 1, pp. 113–118, 1977.

[99] E. Dulkeith, F. Xia, L. Schares, W. M. Green, and Y. A. Vlasov, “Group index and group velocity dispersion in silicon-on-insulator photonic wires,” *Optics Express*, vol. 14, no. 9, pp. 3853–3863, 2006.

[100] D. Tan, K. Ikeda, P. Sun, and Y. Fainman, “Group velocity dispersion and self phase modulation in silicon nitride waveguides,” *Applied Physics Letters*, vol. 96, no. 6, p. 061101, 2010.

[101] K. K. Lee, D. R. Lim, H.-C. Luan, A. Agarwal, J. Foresi, and L. C. Kimerling, “Effect of size and roughness on light transmission in a Si/SiO$_2$ waveguide: Experiments and model,” *Applied Physics Letters*, vol. 77, no. 11, pp. 1617–1619, 2000.

[102] F. Payne and J. Lacey, “A theoretical analysis of scattering loss from planar optical waveguides,” *Optical and Quantum Electronics*, vol. 26, no. 10, pp. 977–986, 1994.

[103] Y. A. Vlasov and S. J. McNab, “Losses in single-mode silicon-on-insulator strip waveguides and bends,” *Optics Express*, vol. 12, no. 8, pp. 1622–1631, 2004.

[104] B. A. Daniel and G. P. Agrawal, “Dependence of dispersive and birefringence properties of silicon nanowires on waveguide dimensions,” *Optics Letters*, vol. 35, no. 2, pp. 190–192, 2010.

[105] S. Mas, J. Caraquitena, J. V. Galán, P. Sanchis, and J. Martí, “Tailoring the dispersion behavior of silicon nanophotonic slot waveguides,” *Optics Express*, vol. 18, no. 20, pp. 20 839–20 844, 2010.

[106] K. Hammani, M. A. Ettabib, A. Bogris, A. Kapsalis, D. Syvridis, M. Brun, P. Labeye, S. Nicoletti, D. J. Richardson, and P. Petropoulos, “Optical properties of silicon germanium waveguides at telecommunication wavelengths,” *Optics Express*, vol. 21, no. 14, pp. 16 690–16 701, 2013.

[107] X. Chen, N. C. Panoiu, I. Hsieh, J. I. Dadap, and R. M. Osgood, “Third-order dispersion and ultrafast-pulse propagation in silicon wire waveguides,” *IEEE Photonics Technology Letters*, vol. 18, no. 24, pp. 2617–2619, 2006.

[108] X. Liu, W. M. Green, I.-W. Hsieh, J. I. Dadap, Y. A. Vlasov, and R. M. Osgood, “Dispersion engineering in silicon photonic wires using thin Si$_3$N$_4$ conformal dielectric coating,” in *Integrated Photonics and Nanophotonics Research and Applications*. Optical Society of America, 2008, p. IMC7.

[109] J. Dadap, N. Panoiu, X. Chen, I.-W. Hsieh, X. Liu, C.-Y. Chou, E. Dulkeith, S. McNab, F. Xia, W. Green *et al.*, “Nonlinear-optical phase modification in dispersion-engineered Si photonic wires,” *Optics Express*, vol. 16, no. 2, pp. 1280–1299, 2008.

[110] L. Jia, M. Geng, L. Zhang, L. Yang, P. Chen, and Y. Liu, “Dispersion characteristics of nanometer-scaled silicon rib waveguides,” *Chinese Optics Letters*, vol. 8, no. 5, pp. 485–489, 2010.

[111] Z. Huang, S. Yuan, Y. Wang, Q. Huang, and J. Xia, “Tailoring the structure of multilayered hybrid silicon vertical waveguide to achieve anomalous dispersion,” *IEEE Photonics Journal*, vol. 9, no. 3, pp. 1–8, 2017.

[112] R. Marchetti, V. Vitali, C. Lacava, I. Cristiani, B. Charbonnier, V. Muffato, M. Fournier, and P. Minzioni, “Group-velocity dispersion in SOI-based channel waveguides with reduced-height,” *Optics Express*, vol. 25, no. 9, pp. 9761–9767, 2017.

[113] Synopsys®, "version L-2016.03," *SPROCESS*.

[114] K. Kawano and T. Kitoh, *Introduction to Optical Waveguide Analysis: Solving Maxwell's Equation and the Schrödinger Equation*. John Wiley & Sons, 2004.

[115] L. Chrostowski and M. Hochberg, *Silicon photonics design: from devices to systems*. Cambridge University Press, 2015.

[116] I. Malitson, "Interspecimen comparison of the refractive index of fused silica," *Journal of the Optical Society of America*, vol. 55, no. 10, pp. 1205–1209, 1965.

[117] D. Marris, A. Cordat, D. Pascal, A. Koster, E. Cassan, L. Vivien, and S. Laval, "Design of a SiGe-Si quantum-well optical modulator," *IEEE Journal of Selected Topics in Quantum Electronics*, vol. 9, no. 3, pp. 747–754, 2003.

[118] L. Naval, B. Jalali, L. Gomelsky, and J. Liu, "Optimization of $Si_{1-x}Ge_x/Si$ waveguide photodetectors operating at $\lambda = 1.3\ \mu$m," *Journal of Lightwave Technology*, vol. 14, no. 5, pp. 787–797, 1996.

[119] D. Perez-Galacho, C. Baudot, T. Hirtzlin, S. Messaoudène, N. Vulliet, P. Crozat, F. Boeuf, L. Vivien, and D. Marris-Morini, "Low voltage 25 Gbps silicon Mach-Zehnder modulator in the O-band," *Optics Express*, vol. 25, no. 10, pp. 11 217–11 222, 2017.

[120] M. Born and E. Wolf, *Principles of optics: electromagnetic theory of propagation, interference and diffraction of light*. Elsevier, 2013.

[121] F. Grillot, L. Vivien, S. Laval, D. Pascal, and E. Cassan, "Size influence on the propagation loss induced by sidewall roughness in ultrasmall SOI waveguides," *IEEE Photonics Technology Letters*, vol. 16, no. 7, pp. 1661–1663, 2004.

[122] H. K. Tsang, C. Wong, T. Liang, I. Day, S. Roberts, A. Harpin, J. Drake, and M. Asghari, "Optical dispersion, two-photon absorption and self-phase modulation in silicon waveguides at 1.5 μm wavelength," *Applied Physics Letters*, vol. 80, no. 3, pp. 416–418, 2002.

[123] H. Liang, Y. He, R. Luo, and Q. Lin, "Ultra-broadband dispersion engineering of nanophotonic waveguides," *Optics Express*, vol. 24, no. 26, pp. 29 444–29 451, 2016.

[124] COMSOL Multiphysics, *https://www.comsol.co.in/*.

[125] Synopsys TCAD, *https://www.synopsys.com/silicon/tcad.html*.

[126] Optiwave, *https://optiwave.com/*.

[127] Lumerical Inc, *https://www.lumerical.com/*.

[128] D. H. Choi and W. J. Hoefer, "The finite-difference-time-domain method and its application to eigenvalue problems," *IEEE Transactions on Microwave Theory and Techniques*, vol. 34, no. 12, pp. 1464–1470, 1986.

[129] T. Namiki, "A new FDTD algorithm based on alternating-direction implicit method," *IEEE Transactions on Microwave Theory and Techniques*, vol. 47, no. 10, pp. 2003–2007, 1999.

[130] ——, "3-D ADI-FDTD method-unconditionally stable time-domain algorithm for solving full vector maxwell's equations," *IEEE Transactions on Microwave Theory and Techniques*, vol. 48, no. 10, pp. 1743–1748, 2000.

[131] A. Splett, M. Majd, and K. Petermann, “A novel beam propagation method for large refractive index steps and large propagation distance,” *IEEE Photonics Technology Letters*, vol. 3, no. 5, pp. 466–468, 1991.

[132] C. Xu, W. Huang, J. Chrostowski, and S. Chaudhuri, “A full-vectorial beam propagation method for anisotropic waveguides,” *Journal of Lightwave Technology*, vol. 12, no. 11, pp. 1926–1931, 1994.

[133] F. Castaldo, G. Abbate, and E. Santamato, “Theory for a new full-vectorial beam-propagation method in anisotropic structures,” *Applied Optics*, vol. 38, no. 18, pp. 3904–3910, 1999.

[134] T. Angkaew, M. Matsuhara, and N. Kumagai, “Finite-element analysis of waveguide modes: A novel approach that eliminates spurious modes,” *IEEE Transactions on Microwave Theory and Techniques*, vol. 35, no. 2, pp. 117–123, 1987.

[135] J. J. Barnes and R. J. Lomax, “Finite-element methods in semiconductor device simulation,” *IEEE Transactions on Electron Devices*, vol. 24, no. 8, pp. 1082–1089, 1977.

[136] D. Hadji, Y. Marechal, and J. Zimmermann, “Three-dimensional semiconductor device simulation by finite element method coupled to monte carlo method,” *IEEE Transactions on Magnetics*, vol. 34, no. 5, pp. 2525–2528, 1998.

[137] G. Brown and B. Lindsay, “The numerical solution of Poisson’s equation for two-dimensional semiconductor devices,” *Solid-State Electronics*, vol. 19, no. 12, pp. 991–992, 1976.

[138] A. Pacelli, “Self-consistent solution of the Schrodinger equation in semiconductor devices by implicit iteration,” *IEEE Transactions on Electron Devices*, vol. 44, no. 7, pp. 1169–1171, 1997.

[139] C. S. Rafferty, M. R. Pinto, and R. W. Dutton, “Iterative methods in semiconductor device simulation,” *IEEE Transactions on Electron Devices*, vol. 32, no. 10, pp. 2018–2027, 1985.

[140] A. Yoshii, H. Kitazawa, M. Tomizawa, S. Horiguchi, and T. Sudo, “A three-dimensional analysis of semiconductor devices,” *IEEE Transactions on Electron Devices*, vol. 29, no. 2, pp. 184–189, 1982.

[141] C. Ringhofer and C. Schmeiser, “A modified Gummel method for the basic semiconductor device equations,” *IEEE Transactions on Computer-Aided Design of Integrated Circuits and Systems*, vol. 7, no. 2, pp. 251–253, 1988.

[142] M. Kemp, C. Tannous, and M. Meunier, “Amorphous silicon device simulation by an adapted Gummel method,” *IEEE Transactions on Electron Devices*, vol. 35, no. 9, pp. 1510–1513, 1988.

[143] H. Jayatilleka, W. D. Sacher, and J. K. Poon, “Analytical model and fringing-field parasitics of carrier-depletion silicon-on-insulator optical modulation diodes,” *IEEE Photonics Journal*, vol. 5, no. 1, pp. 2 200 211–2 200 211, 2013.

[144] C. R. Pollock and M. Lipson, *Integrated photonics*. Chapter 3, 5, Springer, 2003.

[145] L. J. McKnight, M. D. Dawson, and S. Calvez, “Diamond Raman waveguide lasers: completely analytical design optimization incorporating scattering losses,” *IEEE Journal of Quantum Electronics*, vol. 47, no. 8, pp. 1069–1077, 2011.

[146] B. Younis, A. Heikal, M. Hussein, S. Obayya, and M. F. O. Hameed, “Hybrid Si-VO_2 modulator with ultra-high extinction ratio based on slot TM mode,” *Optics Express*, vol. 27, no. 26, pp. 37 454–37 468, 2019.

[147] F. Gardes, G. Reed, N. Emerson, and C. Png, “A sub-micron depletion-type photonic modulator in silicon on insulator,” *Optics Express*, vol. 13, no. 22, pp. 8845–8854, 2005.

[148] F. Gardes, D. Thomson, N. Emerson, and G. Reed, “40 Gb/s silicon photonics modulator for TE and TM polarisations,” *Optics Express*, vol. 19, no. 12, pp. 11 804–11 814, 2011.

[149] Y. Kim, M. Takenaka, and S. Takagi, “Numerical analysis of carrier-depletion strained SiGe optical modulators with vertical pn junction,” *IEEE Journal of Quantum Electronics*, vol. 51, no. 4, pp. 1–7, 2015.

[150] J. Gao and H. Wu, “Multi-function Mach-Zehnder modulator for pulse shaping and generation,” *Optics Express*, vol. 24, no. 19, pp. 22 239–22 249, 2016.

[151] H. Zhu, L. Zhou, L. Liu, T. Wang, Y. Zhou, J. Wang, Q. Wu, A. Xie, R. Yang, Z. Li *et al.*, “Single-drive push-pull silicon Mach-Zehnder modulator for OOK and BPSK modulation,” in *2014 OptoElectronics and Communication Conference and Australian Conference on Optical Fibre Technology*. IEEE, 2014, pp. 174–175.

[152] Y. Zhou, L. Zhou, H. Zhu, C. Wong, Y. Wen, L. Liu, X. Li, and J. Chen, “Modeling and optimization of a single-drive push–pull silicon Mach–Zehnder modulator,” *Photonics Research*, vol. 4, no. 4, pp. 153–161, 2016.

[153] R. Ding, Y. Liu, Q. Li, Y. Yang, Y. Ma, K. Padmaraju, A. E.-J. Lim, G.-Q. Lo, K. Bergman, T. Baehr-Jones *et al.*, “Design and characterization of a 30-GHz bandwidth low-power silicon traveling-wave modulator,” *Optics Communications*, vol. 321, pp. 124–133, 2014.

[154] M. Li, L. Wang, X. Li, X. Xiao, and S. Yu, “Silicon intensity Mach–Zehnder modulator for single lane 100 Gb/s applications,” *Photonics Research*, vol. 6, no. 2, pp. 109–116, 2018.

[155] S. Jain, *Silicon-Germanium Strained Layers and Heterostructures: Semi-conductor and semimetals series*. Elsevier, 2003.

[156] C. G. Van de Walle, “Band lineups and deformation potentials in the model-solid theory,” *Physical Review B*, vol. 39, no. 3, p. 1871, 1989.

[157] S. Krishnamurthy, A. Sher, and A.-B. Chen, “Band structures of $\mathrm{Si}_x\mathrm{Ge}_{1-x}$ alloys,” *Physical Review B*, vol. 33, no. 2, p. 1026, 1986.

[158] J. Hinckley and J. Singh, “Hole transport theory in pseudomorphic $\mathrm{Si}_{1-x}\mathrm{Ge}_x$ alloys grown on Si (001) substrates,” *Physical Review B*, vol. 41, no. 5, p. 2912, 1990.

[159] T. Manku and A. Nathan, “Carrier transport parameters for devices based on $\mathrm{Si}_{1-x}\mathrm{Ge}_x$ strained layers,” *Microelectronics Journal*, vol. 23, no. 6, pp. 463–469, 1992.

[160] S. K. Chun and K. L. Wang, “Effective mass and mobility of holes in strained $\mathrm{Si}_{1-x}\mathrm{Ge}_x$ layers on,” *IEEE Transactions on Electron Devices*, vol. 39, no. 9, pp. 2153–2164, 1992.

[161] M. M. Rieger and P. Vogl, “Electronic-band parameters in strained $\mathrm{Si}_{1-x}\mathrm{Ge}_x$ alloys on $\mathrm{Si}_{1-y}\mathrm{Ge}_y$ substrates,” *Physical Review B*, vol. 48, no. 19, p. 14276, 1993.

[162] G. Zhou and P. Runge, “Modeling of multiple-quantum-well pin photodiodes,” *IEEE Journal of Quantum Electronics*, vol. 50, no. 4, pp. 220–227, 2014.

[163] M. Chagnon, M. Morsy-Osman, M. Poulin, C. Paquet, S. Lessard, and D. V. Plant, “Experimental parametric study of a silicon photonic modulator enabled 112-Gb/s PAM transmission system with a DAC and ADC,” *Journal of Lightwave Technology*, vol. 33, no. 7, pp. 1380–1387, 2015.

[164] C. Xiong, D. M. Gill, J. E. Proesel, J. S. Orcutt, W. Haensch, and W. M. Green, “Monolithic 56 Gb/s silicon photonic pulse-amplitude modulation transmitter,” *Optica*, vol. 3, no. 10, pp. 1060–1065, 2016.

[165] Z. Yong, S. Shopov, J. C. Mikkelsen, R. Mallard, J. C. Mak, S. P. Voinigescu, and J. K. Poon, “Flip-chip integrated silicon Mach-Zehnder modulator with a 28 nm fully depleted silicon-on-insulator CMOS driver,” *Optics Express*, vol. 25, no. 6, pp. 6112–6121, 2017.

[166] S. Shao, J. Ding, L. Zhang, X. Fu, and L. Yang, “Low-voltage linear silicon optical modulator with a single-drive parallel-push–pull scheme,” *Optics Communications*, vol. 407, pp. 271–274, 2018.

[167] R. Willardson, E. R. Weber, J. C. Bean, and R. Hull, *Germanium Silicon: Physics and Materials*. Academic Press, 1998, vol. 56.

[168] R. People, “Indirect band gap of coherently strained $\mathrm{Ge}_x\mathrm{Si}_{1-x}$ bulk alloys on <001> silicon substrates,” *Physical Review B*, vol. 32, no. 2, p. 1405, 1985.

[169] B. Anderson and R. Anderson, *Fundamentals of Semiconductor Devices*. McGraw-Hill, Inc., 2004.

[170] T. Manku and A. Nathan, “Electron drift mobility model for devices based on unstrained and coherently strained $\mathrm{Si}_{1-x}\mathrm{Ge}_x$ grown on <001> silicon substrate,” *IEEE Transactions on Electron Devices*, vol. 39, no. 9, pp. 2082–2089, 1992.

[171] J. E. Sutherland and J. R. Hauser, “A computer analysis of heterojunction and graded composition solar cells,” *IEEE Transactions on Electron Devices*, vol. 24, no. 4, pp. 363–372, 1977.

[172] G. Masetti, M. Severi, and S. Solmi, “Modeling of carrier mobility against carrier concentration in arsenic-, phosphorus-, and boron-doped silicon,” *IEEE Transactions on Electron Devices*, vol. 30, no. 7, pp. 764–769, 1983.

[173] T. Manku, J. M. McGregor, A. Nathan, D. J. Roulston, J.-P. Noel, and D. Houghton, “Drift hole mobility in strained and unstrained doped $\mathrm{Si}_{1-x}\mathrm{Ge}_x$ alloys,” *IEEE Transactions on Electron Devices*, vol. 40, no. 11, pp. 1990–1996, 1993.

[174] D. Patel, V. Veerasubramanian, S. Ghosh, A. Samani, Q. Zhong, and D. V. Plant, “High-speed compact silicon photonic Michelson interferometric modulator,” *Optics Express*, vol. 22, no. 22, pp. 26 788–26 802, 2014.

[175] S. Tanaka, T. Simoyama, T. Aoki, T. Mori, S. Sekiguchi, S.-H. Jeong, T. Usuki, Y. Tanaka, and K. Morito, “Ultralow-power (1.59 mW/Gbps), 56-Gbps PAM4 operation of Si photonic transmitter integrating segmented PIN Mach–Zehnder modulator and 28-nm CMOS driver,” *Journal of Lightwave Technology*, vol. 36, no. 5, pp. 1275–1280, 2018.

[176] S. Pal and S. Gupta, “Junction-less optical phase shifter loaded silicon Mach–Zehnder modulator,” *Optics Communications*, vol. 437, pp. 110–120, 2019.

[177] V. Sorianello, M. Midrio, G. Contestabile, I. Asselberghs, J. Van Campenhout, C. Huyghebaert, I. Goykhman, A. Ott, A. Ferrari, and M. Romagnoli, “Graphene–silicon phase modulators with gigahertz bandwidth,” *Nature Photonics*, vol. 12, no. 1, p. 40, 2018.

[178] J. Fujikata, M. Noguchi, Y. Kim, J. Han, S. Takahashi, T. Nakamura, and M. Takenaka, "High-speed and highly efficient Si optical modulator with strained SiGe layer," *Applied Physics Express*, vol. 11, no. 3, p. 032201, 2018.

[179] S. Yu, Y. Liu, and T. Chu, "Highly linear silicon Mach-Zehnder modulators with optimized phase-shifter," in *2017 International Topical Meeting on Microwave Photonics (MWP)*. IEEE, 2017, pp. 1–3.

[180] H. Zhu, L. Zhou, T. Wang, L. Liu, C. Wong, Y. Zhou, R. Yang, X. Li, and J. Chen, "Optimized silicon QPSK modulator with 64-Gb/s modulation speed," *IEEE Photonics Journal*, vol. 7, no. 3, pp. 1–6, 2015.

[181] A. Simard, B. Filion, D. Patel, D. Plant, and S. LaRochelle, "Segmented silicon MZM for PAM-8 transmissions at 114 Gb/s with binary signaling," *Optics Express*, vol. 24, no. 17, pp. 19 467–19 472, 2016.

[182] M. He, M. Xu, Y. Ren, J. Jian, Z. Ruan, Y. Xu, S. Gao, S. Sun, X. Wen, L. Zhou *et al.*, "High-performance hybrid silicon and lithium niobate Mach–Zehnder modulators for 100 Gbit.s^{-1} and beyond," *Nature Photonics*, vol. 13, no. 5, pp. 359–364, 2019.

[183] H. Dalir, Y. Xia, Y. Wang, and X. Zhang, "Athermal broadband graphene optical modulator with 35 GHz speed," *ACS photonics*, vol. 3, no. 9, pp. 1564–1568, 2016.

[184] T. Hiraki, T. Aihara, K. Hasebe, K. Takeda, T. Fujii, T. Kakitsuka, T. Tsuchizawa, H. Fukuda, and S. Matsuo, "Heterogeneously integrated III–V/Si MOS capacitor Mach–Zehnder modulator," *Nature Photonics*, vol. 11, no. 8, pp. 482–485, 2017.

[185] T. Hiraki, T. Aihara, K. Takeda, T. Fujii, T. Kakitsuka, T. Tsuchizawa, H. Fukuda, and S. Matsuo, "Membrane InGaAsP Mach-Zehnder modulator with SiN:D waveguides on Si platform," *Optics Express*, vol. 27, no. 13, pp. 18 612–18 619, 2019.

[186] Y. Ogiso, J. Ozaki, N. Kashio, N. Kikuchi, H. Tanobe, Y. Ohiso, and M. Kohtoku, "100 Gb/s and 2 V V_π InP Mach-Zehnder modulator with an nipn heterostructure," *Electronics Letters*, vol. 52, no. 22, pp. 1866–1867, 2016.

[187] D. K. Schroder, R. N. Thomas, and J. C. Swartz, "Free carrier absorption in silicon," *IEEE Journal of Solid-State Circuits*, vol. 13, no. 1, pp. 180–187, 1978.

[188] B. Senapati, "Modelling of strained silicon-germanium material parameters for device simulation," *IETE Journal of Research*, vol. 53, no. 3, pp. 215–236, 2007.

[189] S. He, J. Xu, and V. G. Romanov, "A simple analytical method for calculating the leakage loss of a buried rectangular waveguide," *Journal of Optics A: Pure and Applied Optics*, vol. 6, no. 1, p. 57, 2003.